FEDERAL UNIVERSITY OF MINAS GERAIS
Engineering School
Structural Engineering Post Graduate Program

Thiago Henrique Lara Pinto

NUMERICAL MODELLING STRATEGIES FOR COMPRESSION AFTER IMPACT ANALYSES OF COMPOSITE LAMINATES

Belo Horizonte
2023

Thiago Henrique Lara Pinto

NUMERICAL MODELLING STRATEGIES FOR COMPRESSION AFTER IMPACT ANALYSES OF COMPOSITE LAMINATES

Thesis submitted to the Structural Engineering Post Graduate Program of the Engineering School from Federal University of Minas Gerais, in partial fulfillment of the requirements for the degree of "Doctor in Structural Engineering".

Advisor: Prof. Dr. Carlos Alberto Cimini Jr.

Belo Horizonte
2023

Pinto, Thiago Henrique Lara.
P659n Numerical modelling strategies for compression after impact analyses of composite laminates [recurso eletrônico] / Thiago Henrique Lara Pinto. - 2023.
1 recurso online (154 f. : il., color.) : pdf.

Orientador: Carlos Alberto Cimini Jr.

Tese (doutorado) - Universidade Federal de Minas Gerais, Escola de Engenharia.

Bibliografia: f. 136-154.
Exigências do sistema: Adobe Acrobat Reader.

1. Engenharia de estruturas - Teses. 2. Materiais compostos - Teses. 3. Materiais laminados - Teses. 4. Modelagem - Teses. I. Cimini Júnior, Carlos Alberto. II. Universidade Federal de Minas Gerais. Escola de Engenharia. III. Título.

CDU: 624(043)

Ficha catalográfica elaborada pela Bibliotecária Roseli Alves de Oliveira CRB/6 2121
Biblioteca Prof. Mário Werneck, Escola de Engenharia da UFMG

UNIVERSIDADE FEDERAL DE MINAS GERAIS

PROGRAMA DE PÓS-GRADUAÇÃO EM ENGENHARIA DE ESTRUTURAS

PROPEEs UFMG

ATA DA DEFESA DE TESE DE DOUTORADO EM ENGENHARIA DE ESTRUTURAS Nº: 90 DO ALUNO THIAGO HENRIQUE LARA PINTO

Às **08:00** horas do dia **02** do mês de **fevereiro** de **2023**, reuniu-se em ambiente virtual, na Escola de Engenharia da Universidade Federal de Minas Gerais - UFMG, a Comissão Examinadora indicada pelo Colegiado do Programa em **11 de novembro de 2022**, para julgar a defesa da Tese de Doutorado intitulada **"Numerical Modelling Strategies for Compression After Impact Analyses of Composite Laminates"**, cuja aprovação é um dos requisitos para a obtenção do Grau de DOUTOR EM ENGENHARIA DE ESTRUTURAS na área de ESTRUTURAS.

Abrindo a sessão, o Presidente da Comissão, **Prof. Dr. Carlos Alberto Cimini Júnior**, após dar a conhecer aos presentes o teor das Normas Regulamentares passou a palavra ao candidato para apresentação de seu trabalho. Seguiu-se a arguição pelos examinadores, com a respectiva defesa do candidato. Logo após, a Comissão se reuniu, sem a presença do candidato e do público, para julgamento e expedição do resultado final.

Prof. Dr. Carlos Alberto Cimini Jr. - DEES - UFMG (Orientador)
Prof. Dr. Estevam Barbosa de Las Casas - DEES - UFMG
Prof. Dr. Túlio Hallal Panzera - UFSJ
Prof. Dr. Maurício Vicente Donadon - ITA
Prof. Dr. José Daniel Diniz Melo - UFRN

Após reunião, a Comissão considerou o candidato APROVADO, conforme pareceres em anexo.

O resultado final foi comunicado publicamente ao candidato pelo Presidente da Comissão. Nada mais havendo a tratar, o Presidente encerrou a reunião e lavrou a presente ATA, que será assinada por todos os membros participantes da Comissão Examinadora.

Belo Horizonte, 02 de fevereiro de 2023.

Observações:

1. A aprovação do candidato na defesa da Tese de Doutorado não significa que o mesmo tenha cumprido todos os requisitos necessários para obtenção do Grau de Doutor em Engenharia de Estruturas;
2. Este documento não terá validade sem a assinatura do Coordenador do Programa de Pós-Graduação.

Documento assinado eletronicamente por **Mauricio Vicente Donadon**, **Usuário Externo**, em 02/02/2023, às 12:52, conforme horário oficial de Brasília, com fundamento no art. 5º do Decreto nº 10.543, de 13 de novembro de 2020.

Documento assinado eletronicamente por **Estevam Barbosa de Las Casas**, **Diretor(a)**, em 02/02/2023, às 12:53, conforme horário oficial de Brasília, com fundamento no art. 5º do Decreto nº 10.543, de 13 de novembro de 2020.

Documento assinado eletronicamente por **Tulio Hallak Panzera**, **Usuário Externo**, em 02/02/2023, às 12:54, conforme horário oficial de Brasília, com fundamento no art. 5º do Decreto nº 10.543, de 13 de novembro de 2020.

Documento assinado eletronicamente por **José Daniel Diniz Melo**, **Usuário Externo**, em 02/02/2023, às 12:54, conforme horário oficial de Brasília, com fundamento no art. 5º do Decreto nº 10.543, de 13 de novembro de 2020.

Documento assinado eletronicamente por **Carlos Alberto Cimini Junior**, **Professor do Magistério Superior**, em 02/02/2023, às 13:00, conforme horário oficial de Brasília, com fundamento no art. 5º do Decreto nº 10.543, de 13 de novembro de 2020.

Documento assinado eletronicamente por **Felicio Bruzzi Barros**, **Coordenador(a) de curso de pós-graduação**, em 01/03/2023, às 18:10, conforme horário oficial de Brasília, com fundamento no art. 5º do Decreto nº 10.543, de 13 de novembro de 2020.

A autenticidade deste documento pode ser conferida no site https://sei.ufmg.br/sei/controlador_externo.php?acao=documento_conferir&id_orgao_acesso_externo=0, informando o código verificador **2042677** e o código CRC **8B586AC3**.

Referência: Processo nº 23072.204193/2023-22 SEI nº 2042677

A Matemática, senhora, que ensina o homem a ser simples e modesto, é a base de todas as ciências e de todas as artes.

(in free translation:
Mathematics, madam, which teaches man to be simple and humble, is the basis of all the sciences and all the arts.)

Malba Tahan, *aka* Júlio César de Mello e Souza,
O homem que calculava
(in free translation: The man who counted)

Dedicated to the departed owners of my Ford Rural, my beloved father and grandfather, and to my dear daughter, who was born with the mission of inheriting a beautiful vintage car.

Acknowledgements

First of all, I would like to express my gratitude to my family, especially to my parents, Raimundo (in memorian) and Regina, my brother, Fernando, my wife, Liliane, my daughter, Beatriz, and my mother in law, Graça, for having always supported me.

I would like to express my sincere gratitude to Professors Cimini and Sung Ha, for the generosity and all the support and guidance to the accomplishment of this work.

To the professors of the Department of Structural Engineering of UFMG, for the contribution to my formation and in the development of this work.

To the professors of the Institute of Science and Technology of UFVJM, for all the support and friendship, and for UFVJM institution itself for the all support through actions such as Planquali and qualification leaves.

To all the teachers I've had since my childhood, especially Átylla Gontijo, my first physics teacher, a guy who tries his best to make his students enjoy exact sciences.

To the friends of UFMG, Hanyang and UFVJM for their comments and contributions, without which this route would have been immeasurably more arduous.

To CAPES for the financial support through the Doctoral Sandwich Abroad Program (in portuguese: Programa de Doutorado Sanduíche no Exterior-PDSE), edital no. 47/2017, process number 88881.187859/2018-01.

Abstract

This work proposes a cost-effective virtual testing methodology, comparing both traditional and multiscale approaches, focusing on Compression After Impact loading in composite material. First, a parametric modeling tool was coded, allowing a user-friendly and flexible virtual testing model development, being capable of automatic process different layups, materials and criteria. The second part, an user subroutine which contains the core of the proposed model when working with multiscale analysis, was developed based on the Octogonal Fiber Model (OFM), micro-mechanical failure criteria, and a damage homogenization metric especially proposed, tested and implement for OFM. Finally, a semi-automatic damage metric was conceived to reduce human induced variables during impact damaged area measurements and, optionally, non-negligible cracks measurements, during the numerical and experimental damage images post-processing. The proposed multi-scale model, applied together with user-friendly pre and post-processing subroutines, presented good results for predictions of Post Impact Compression (CAI) virtual tests, proving to be promising for future developments.

Keywords: Composite Materials, Multiscale Analysis, Compression After Impact (CAI), Global/Local Analysis, Octagonal Fiber Model (OFM)

Resumo

Este trabalho propõe uma metodologia de teste virtual de baixo custo computacional, comparando-se abordagens tradicionais e multiescala, tendo como foco o carregamento de Compressão Pós Impacto em materiais compósitos. Primeiramente, foi implementada uma ferramenta de modelagem paramétrica que permite o desenvolvimento de um modelo de ensaio virtual de forma amigável e flexível, sendo capaz de processar automaticamente diferentes laminados, materiais e critérios. A segunda parte, uma sub-rotina que contém o núcleo do modelo proposto quando baseado em análise multiescala, foi desenvolvida com base no Modelo de Fibra Octogonal (OFM), critérios de falha micromecânica e uma métrica de homogeneização de danos especialmente proposta, testada e implementada para o OFM. Por fim, uma métrica de dano semi-automática foi concebida para reduzir as variáveis induzidas pelo usuário durante as medições da área de dano por impacto e, opcionalmente, medições de trincas não desprezíveis, durante o pós-processamento das imagens de danos numéricos e experimentais. O modelo multi-escala proposto, juntamente com rotinas de pré e pós-processamento amigáveis ao usuário, apresentaram bons resultados para previsões de testes virtuais de Compressão Pós Impacto (CAI), demonstrando-se promissores para desenvolvimentos futuros.

Palavras-Chave: Materiais Compósitos, Análise Multiescala, Compressão Pós Impacto, Análise Global/Local, Modelo de Fibra Octogonal (OFM)

List of Figures

List of Tables

List of Abbreviations and Acronyms

CAI Compression After Impact

DOF Degree Of Freedom

FEM Finite Element Method

GUI Graphical User Interface

HSCL Hanyang Structures and Composites Laboratory

LDM, LGM, SDM DDM and WDM CAI failure descriptions: L stands for lateral failure; G for gauge/away from damage failure area; M is the middle location; D for at/through damage failure area; and W for transversal failure

MEF *Método de Elementos Finitos* (in Portuguese)

MMF Micro-Mechanics of Failure

OHT Open Hole Traction

OHC Open Hole Compression

OFM Octagonal Fiber Model

RVE Representative Volume Element

SAF Stress Amplification Factor

ShAI Shear After Impact

SLJ Single Lap Joint

SP Series-Parallel Approach

TAI Tension After Impact

UMAT Abaqus®/Standard user-defined Material

VUMAT Abaqus®/Explicit user-defined Material

WWFE-II Second World-Wide Failure Exercise

List of Symbols

chapter 3

subsection 3.1.1

X_T Longitudinal tensile strength

X_C Longitudinal compressive strength

Y_T Transverse tensile strength

Y_C Transverse compressive strength

S_L Longitudinal shear strength

S_T Transverse shear strength

α Coefficient that determines shear stress contribution to the fiber initiation criterion

σ Effective stress

subsection 3.1.2

X_T Longitudinal tensile strength

X_C Longitudinal compressive strength

Y_T Transverse tensile strength

Y_C Transverse compressive strength

S_{12}, S_{13} and S_{23} Shear strengths in the respective principal material directions

σ Effective stress

section 3.2

$\mathbf{t}$ Nominal traction stress vector

δ Separation vector

G Work done by the traction and their conjugate relative displacements

η Material parameter-based exponent

n Normal direction

s 1st shear direction

t 2nd shear direction

section 3.3

A Stress amplification factor - thermal portion

D Damage variable

E Elastic degradation

E_o Elastic undamaged response

M Stress amplification factor

ΔT temperature variation

σ Effective micro-stresses

$\bar{\sigma}$ Macro-stresses

$\tilde{\sigma}$ Micro-stress

subsection 3.3.1

M_{ij} Stress Amplification Factors (SAF)

σ Ply stresses

$\bar{\sigma}$ Microstresses

c Constituent

f Fiber

m Matrix

i Interface

ij Sub-regions identification index in OFM

a, b *and* c Dimensions in OFM sub-regions

$\bar{E}$ Effective ply Elastic Modulus

$\bar{v}$ Effective ply Poisson

$\bar{G}$ Effective ply transverse shear modulus

subsection 3.3.2

X_f Longitudinal fiber tensile strength

X'_f Longitudinal fiber compressive strength

Y_f Transverse fiber tensile strength

Y'_f Transverse fiber compressive strength

S_{f4} Transverse fiber shear strength

S_{f6} Longitudinal fiber shear strength

σ_x Effective fiber longitudinal stress

subsection 3.3.3

I_1, I_2 *and* I_3 Invariants

X_f Longitudinal fiber tensile strength

X'_f Longitudinal fiber compressive strength

Y_f Transverse fiber tensile strength

Y'_f Transverse fiber compressive strength

S_{f4} Transverse fiber shear strength

S_{f6} Longitudinal fiber shear strength

σ_x *or* σ_{11} Matrix longitudinal stress

σ_y *or* σ_{22} Matrix transversal stress

σ_z *or* σ_{33} Matrix out-of-plane stress

τ_{xy} *or* τ_{12}, τ_{yz} *or* τ_{23} *and* τ_{zx} *or* τ_{32} Shear stresses in matrix

σ_{VM} von Mises state of stresses

cr Critical value

C_m Matrix compressive strength

T_m Matrix tensile strength

subsection 3.3.4

$\mathbf{t}$ Nominal traction stress vector

n Normal direction

s Shear direction

t tangential direction

x longitudinal direction

Y Interface maximum allowable value

chapter 5

section 5.2

C Stiffness matrix terms

t step time

M_{ij} Stress Amplification Factors (SAF)

$\bar{\sigma}$ Ply stresses

σ *and* τ Microstresses

t_i Interface microstresses

ε Ply strains

V_f Volume fraction

c Constituent

f Fiber

m Matrix

i Interface

ij Sub-regions identification index in OFM

a, b *and* c Dimensions in OFM sub-regions

$\bar{E}$ Effective ply Elastic Modulus

$\bar{v}$ Effective ply Poisson

$\bar{G}$ Effective ply transverse shear modulus

C_m Matrix compressive strength

T_m Matrix tensile strength

X_f Longitudinal fiber tensile strength

X'_f Longitudinal fiber compressive strength

$\mathrm{s_{mtc}}$ Shear module factors to control loss of shear stiffness caused by matrix tensile and compressive failure.

A Section area

L Section length

dam Damaged value

d Damage index

$homog$ Mean homogenized value obtained by proposed procedure

$C_{Bauwens}$ Bauwens criteria failure index

$C_{Interface}$ Interface criteria failure index

Index

Chapter 1

Introduction

As stated by Santos et al. (2022), composite materials are composed by multiple phases with distinct functionalities, and by well-defined and non-miscible interfaces, with possible surface chemical reactions. Each of these phases may be defined as a conventional monolithic material, as metals, ceramics or polymers, combined to achieve a certain performance, superior to the individual phases incorporated in nano, micro, and/or macro scales (Daniel and Ishai, 2005; Santos et al., 2022).

Composite materials are ideal for structural applications where high strength-to-weight and stiffness-to-weight ratios are required. Since the antiquity, the humanity uses different materials combinations in order to improove products quality. From the early days, it's observed the use of wood, a natural composite material considering the fact that its properties vary significantly with and against the fiber directions. Over time, materials have been specialy developed in order to build goods: from houses and facilities built from primitive mud bricks reinforced with straw, later replaced by steel bars reinforced concrete, to the modern airframe structures built from fiber reinforced composites (Niu, 2010). Advanced composite material systems has experienced a significant boom in the past years, with applications in the manufacture of a variety of products, ranging from aircrafts, spacecrafts, missiles and rockets, to sport goods, marine and automobile components, civil engineering, and biomedical applications (Daniel and Ishai, 2005; Srinivasan, 2009; Alves and Cimini Jr, 2022).

As described later in this text, a composite material may be analyzed from a scale based on its fiber's dimensions, to the scale of the analyzed component itself. Each of these scales having its inherent advantages and disadvantages. The work presented herein proposes to develop a compression after impact (CAI) virtual testing for composite materials methodology, including a low computational cost multiscale-based model, and to compare its capabilities and demands with models and criteria conventionally used in industry.

During this work, computational tools were developed for pre-processing, processing and post-processing of results. Figure 1.1 presents the proposed modeling and analysis flowchart.First, an automatic modeling interface was developed, being able to generate impact and post-impact compression models from input parameters such as the description of laminates, materials and main dimensions. The tool was developed based on the ASTM standards for Impact (ASTM, 2014) and CAI (ASTM, 2012), but can easily adapt to other standards. The CAI Virtual Testing Parametric Modeling (pre-processor tool) creates the Impact and Compression After Impact (CAI) models, using a Graphic User Interface (GUI) to insert input data and select control options. The created models for Impact case may be processed with both conventional failure criteria or considering an user subroutine (VUMAT) defined criteria.The created model for CAI case is then processed, considering impact results as the initial condition for the laminate model, again being possible to apply different failure criteria options. In this work, a micro-mechanical subroutine based on the Octagonal Fiber Model (OFM) (Huang et al., 2020) model was proposed and developed. To this end, a damage homogenization methodology was proposed to enable the feedback of the macroscale model based on the damage calculated in the OFM. This code calculates stresses in a micro-mechanical unit cell, based on the macro-mechanical model and Octagonal Fiber Model (OFM) theory, evaluates failure, applies the proposed section-based homogenization method to calculate material progressive damage, and then updates the macro-mechanical

properties. Finally, based on an open source image processing package named Scikit-Image (Walt et al., 2014), an automatic damage measurement subroutine was developed.Also considering the laminate model impact results, the Damage Measurement Tool (post-processor tool) is applied to perform impact damage area measurement with minimal human influence.

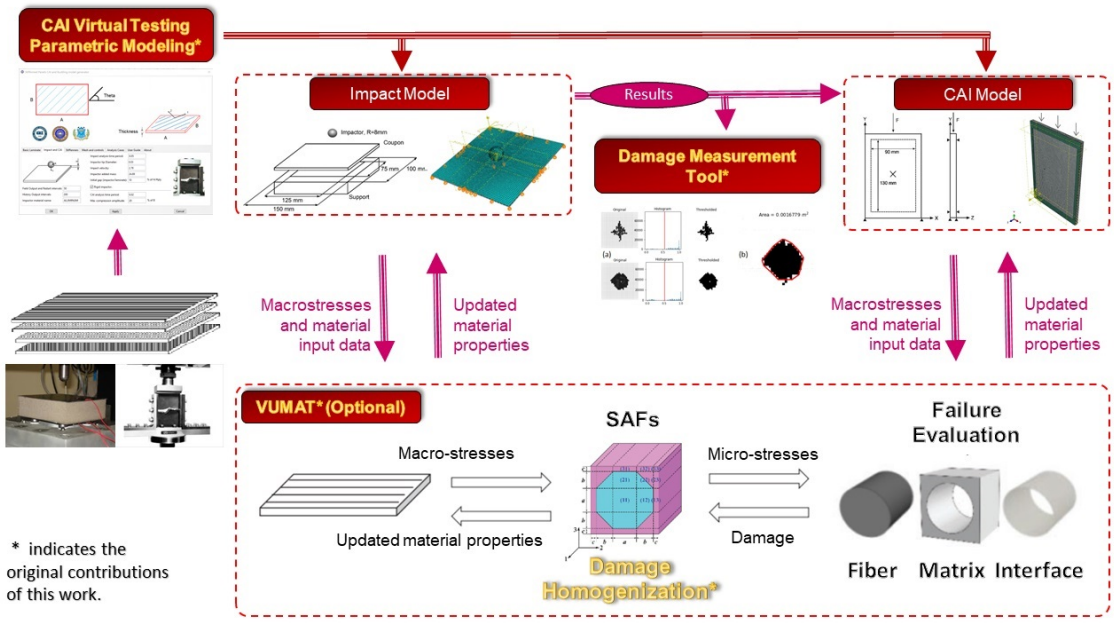

Figure 1.1: Multi-scale analysis flowchart considering the proposed tools.

1.1 Motivation

Compression After Impact is a key topic in the characterization of composite materials for aircraft structural applications (Zou et al., 2021; Fatima et al., 2021; Seamone et al., 2022; Knopp et al., 2022; Yin and Iannucci, 2022; Linke, 2022). Due to the lack of reliable and efficient computational CAI methodologies, the topic is usually verified in a very experimental demanding way in the aeronautical companies. This thesis aims to develop a virtual testing methodology to study the effect of impact and Compression After Impact (CAI), developing tools capable to reduce

time and costs during the aircraft design, providing a robust methodology for CAI analysis for engineers in charge of designing composites aircraft components. A cost effective multi-scale approach is advantageous for the proposed subject since the conventional macroscale FEM analyses do not capture the local effects, and a full microscale FEM is not feasible, for most conventional aircraft structures, due to extremely high computational costs. Considering that, Octagonal Fiber Model (Huang et al., 2020) micromechanics analysis-based model was selected since it is simple enough to be implemented in a Fortran user subroutine, despite being capable of generating information and verifications at the constituent scale. .The analysis is proposed to be developed in both micro and macro scales, studying carbon/epoxy fiber reinforced composites. The multi-scale criteria results are compared with different conventional failure criteria foccusing on understanding the advantages and disadvantages of the different modeling possibilities.

1.2 Problem Statement

The main objective of this work is to develop a multi-scale virtual testing methodology for Compression After Impact (CAI) loading in composite materials, with the aim of reducing the experimental impact and CAI test campaign, and providing a reliable and efficient way to study the damage tolerance and residual compression strength after impact in composite aeronautical components.

As secondary objectives of the research, it is proposed to develop and verify a multi-scale approach based on the Octagonal Fiber Model (OFM) (Huang et al., 2020) and micro-mechanical failure criteria for fiber, matrix and interface, and to compare it with the conventional macro-scale criteria based on the two-dimensional Hashin failure criterion; to develop an user-friendly and flexible Compression After Impact (CAI) Virtual Test Parametric Modeling Tool to automate the processing of different layups, materials and failure criteria; and to develop an automatic damage

area measurement post-processor tool focusing in minimize human interference in impact damage measurement metrics.

The proposed methodology and tools will provide a valuable contribution to the composite materials studies in aeronautical sector, providing new tools for virtual testing and CAI residual strength prediction. The following specific tasks can be enumerated:

- to develop of a user-friendly semiautomatic modeling preprocessing tool;
- to extend Hashin failure criterion for 3D models;
- given the literature microscale Octagonal Fiber Model (OFM) for the multi-scale analysis:
  - to propose a damage homogenization method for the OFM unit cell;
  - to propose a subroutine for the micromechanical failure model;
  - to verify the model accuracy for strength prediction;
- to develop an automatic damage area measurement procedure to reduce human influence;
- to compare CAI analysis results considering different strategies for 5 models:
  - **Case 1.** 2D model without cohesive surfaces using conventional Hashin failure criterion;
  - **Case 2.** 2D model including cohesive surfaces using conventional Hashin failure criterion;
  - **Case 3.** 3D model including cohesive surfaces using Hashin/Puck-based Nie (2014) failure criterion;
  - **Case 4.** 3D model including cohesive surfaces using Hashin extended failure criterion for three-dimensional elements;

- **Case 5.** 3D model including cohesive surfaces using mulitiscale approach with micromechanics OFM-based failure criterion.

1.3 Thesis Outline

This work was divided into eight chapters. Chapter 1 presents the work motivation, the problem description and this chapter outline. Following, chapter 2 presents a literature review, used as a contextualization for these studies.

Chapter 3 provides the theoretical foundation necessary for the development of this work. It starts with the Classical Lamina Level Theory Failure Criteria, commonly applied to macro-scale composite models. Next, a brief description of the adopted Interply Cohesive Failure Criteria is presented. Finally, this chapter presents a study on the basis of the proposed micro-stresses approximation and to the failure criteria adopted in the presented multi-scale analysis.

Chapter 4 describes the adopted methodology for developing and verifying the proposed Compression After Impact (CAI) virtual testing procedure.

Chapter 5 describes the main computational tools proposed and developed during this work focusing in performing Compression After Impact (CAI) predictions for composite materials. First, a semiautomatic user-friendly Graphic User Interface (GUI) is presented in section 5.1. The developed tool is capable of automatically building Impact and CAI models and to be used with different user developed subroutines (VUMAT). The second part (section 5.2) presents a cost-effective model based on Octogonal Fiber Model (Huang et al., 2020) and micromechanics analysis-based criteria, developed focusing on CAI problem. Finally, section 5.3 presents the developed damage area measurement procedure for impact test results, which creates an standard criteria for various tested specimens, focusing on human factor reduction in impact damage measurements.

Chapter 6 presents the obtained results during the developed multi-scale user

subroutine (VUMAT) validation considering simple load cases. Then in chapter 7 the obtained CAI results when applying the proposed multi-scale model aer compared with traditional failure criteria and experimental results obtained in the literature (Tan et al., 2015*a*).

Discussion and conclusions about the studies and developments are presented in chapter 8, which also contains some suggestions for future work.

Chapter 2

Literature Review

A structural composite material is a system composed by two or more phases which, on microscale, can be analyzed separately or, if observed on a macroscopic scale, form a new material whose mechanical properties can be designed to be superior to those of its constituents acting separately. One of these phases is usually more rigid and resistant, which is called the reinforcement, and the other, weaker and less rigid, is called matrix. The properties of a composite material are dependent on the properties of its constituents, their geometry and the distribution of the different materials employed in their phases. A third distinct phase, called interfase (Figure 2.1), can be generated by chemical reactions in the interface between the matrix and the reinforcement (Daniel and Ishai, 2005). An interface is typically modeled in zero dimensional terms and may be described as the boundary between two layers of different microstructure. Such boundaries usually are formed by chemical interaction, being the volume of material affected at the constituents' interface. The term interphase, a three-dimensional zone Sharpe (1972), indicates the presence of a chemically or mechanically altered zone between adjacent phases (Jesson and Watts, 2012). This region governs the transfer of forces between the matrix and the reinforcing fibers. An effective interphase can ensure that the mechanical properties of the composite reflect the high strength and modulus of the fibers (Piggott, 1987). The incorporation of an interphasial region into micromechanical analyses of composite stiffness and strength requires a reevaluation of the problem, and the level

of complexity modeled is limited by our ability to measure interphasial and initial condition properties (Swain et al., 1990; Ha et al., 2008; Huang, Jin and Ha, 2012; Linke, 2022).

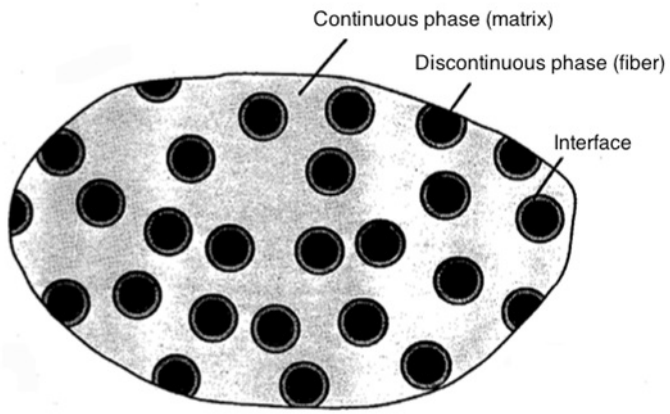

Figure 2.1: Schematic cross-section of composite material (Daniel and Ishai, 2005).

A wide variety of matrices may be applied to various particulate or fibrous reinforcing elements. It is also possible, for example, to associate fiber reinforcements to metals in order to achieve a balance between the advantages of fibers and metallic materials (Marinucci, 2011). The adhesive nature at the matrix-reinforcement interface is dependent on factors such as the presence of functional groups in the fiber, produced by some type of superficial treatment; orientation, atomic arrangement, crystallinity and chemical properties of the reinforcement; molecular conformation and chemical constitution of the matrix; resin surface tension (viscosity) and fiber roughness; diffusivity of the elements of each constituent; and fibers geometric arrangement (LevyNeto and Pardini, 2006; Huang et al., 2008; Zhang et al., 2022). Due to its anisotropic nature, different tests and specimens standards are necessary for the properties evaluation of a composite material (Srinivasan, 2009). Advanced composite materials are widely used in the aerospace industry due to their high rigidity, strength-to-weight ratio and anisotropy, which provides elastic and mass

project possibilities during the design of structural components. However, complex and expensive test programs are needed to fully characterize the material and its failure modes. In recent years, significant efforts have been made to develop precise numerical methods, in order to reduce this cost. Efforts have been made to obtain structural composites components correlating material properties, structural performance, use of different manufacturing processes and cost reduction (Rezende et al., 2011). The widespread use of composite material structures often requires the association of different composite and metallic components (Moura et al. (2009); Tang et al. (2015)).

2.1 Modeling Techniques

Numerical methods are used during the analysis and design of complex structures, applying mathematically simulated processes to represent a real-world phenomena (Hamming, 1987). One of the most widely used numerical methods in engineering, the finite element method, was originally developed for the study of complex aeronautical structures, being later applied to different areas (Huebner, 1975). Heterogeneous materials, such as composite materials, demand a large number of parameters in order to enable the material description, which leads to a expensive experimental process. Considering that properties vary as a function of the partial fractions of matrix and reinforcement, homogenization techniques are used in order to predict the composite material properties as a function of the properties of its constituents (Barbero, 2007; Chechkin et al., 2007; Caminero et al., 2018; Vignoli et al., 2022). Aiming to represent the behavior of composite materials, approximations are commonly developed, such as the representation of a honeycomb structure by a mesh of nonlinear springs Aminanda et al. (2009). Simplified approaches requires calibrations using specific test results (Rahmé et al., 2012). A consistent work to develop failure criteria due to impact is currently been developed by Professor Ha and

his group at the Hanyang Structures and Composites Laboratory (HSCL), studying topics such as failure and progressive damage (Ha et al., 2010; Zhao et al., 2017), impact damage resistance (Park et al., 2008) and induced delamination detection (Hayat and Ha, 2014; Koynagi et al., 2009), to develop precise and computationally efficient techniques that take into account the most important scales involved in the simulation of composite material structures, allowing the analyst to choose the desired precision and detail level.

Several theories can be used in modeling the nonlinear mechanical behavior of composite materials, such as the series-parallel approach, developed for long fibers, where the laminae material is described by an approach of elements in parallel in the main direction of their fibers, and in series in the orthogonal direction. Based on classical laminate theory, this this theory can be extended to multidirectional laminates (Rastellini et al., 2008). A simplified form of this mixture theory formulation can be applied in order to optimize the computational performance of an explicit finite element model of large scale composite structures. In Martinez et al. (2011) work, an isotropic damage law modification is proposed, capable of taking into account the residual friction force in fracture modes, where it is possible to predict mechanical performance and delamination of composite materials.Otero et al. (2012) proposed to apply constitutive models to predict the mechanical performance of nano carbon tubes composites, considered as ideal reinforcements for high performance composites due to their matrix-reinforcement interface connection. The formulation was developed based on the mixing theory, dividing the composite between matrix and a new material, relative to the carbon nanotubes and the coupling interface, taking into account the non-linear effects generated in these bodies. The same group later performed a comparison of micro-structural approaches, mixing theory and homogenization, applied to linear models of composite materials structures (Otero et al., 2015). Finite element models intended to capture micromechanical effects (fiber,

matrix and interface scale) should generally employ meshes with elements size similar to the microstructure, resulting in an extremely high computational cost. On the other hand, homogenization techniques for heterogeneous materials analysis, although leading to manageable problem sizes, are deficient when microscopic fields information is required. Multiscale damage models, as well as classic failure criteria, are representative when compared to experimental data (Ivančević and Smojver, 2016; Wang et al., 2021; Kok et al., 2022). The multiscale modeling strategy is then an attempt to achieve precision in the macroscale damage evolution, analysing both micro and macro scales with a rationalized computational cost, besides the intrinsic precision gain of the model (Kwon et al., 2007; Xu et al., 2014; Ma et al., 2021; Hou et al., 2022).

2.2 Impact Induced Damage and Compression After Impact Effects

Composite components are commonly exposed to impacts during operation (Keegan et al., 2013; Verma et al., 2017; Verma, Jiang, Vedvik, Gao and Ren, 2019; Verma, Vedvik and Gao, 2019; Verma, Vedvik, Haselbach, Gao and Jiang, 2019; Shah, Megat-Yusoff, Karuppanan, Choudhry and Sajid, 2021), leading to the deterioration of structural integrity and load-bearing ability. Impact induced damage (Figure 2.2) in the form of matrix cracking, delamination, and fiber fracture may threaten the fatigue life of the component (Niu, 2010; Ullah and Silberschmidt, 2015).

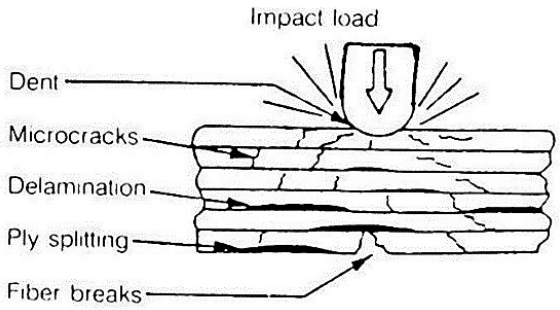

Figure 2.2: Typical failure modes for impact (Niu, 2010).

The structural stiffness degradation should be investigated for several types of impact loading (Figure 2.3), ranging from low velocity impact, which leads to barely visible impact damage with significant effects on compressive strength, to ballistic high-velocity impact, focusing on the residual velocity of the projectile and target energy absorption related to the impact velocity and angle. Thus, the study of impact and post-impact compression becomes very important, mainly for the identification of damage effects resulting from low energy impacts and, therefore, damages that are difficult to detect.

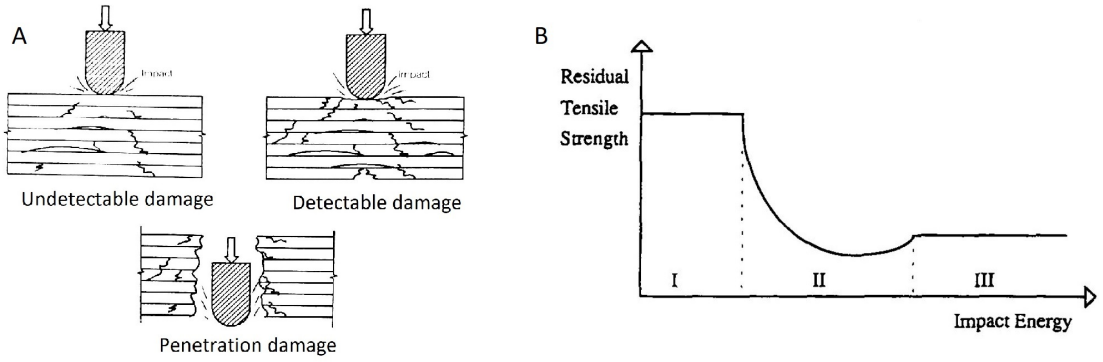

Figure 2.3: Impact energy effects: (A) Detectability (Niu, 2010) and (B) Characteristic residual strength versus impact energy (Richardson and Wisheart, 1996).

The impact damage generated in composite laminates has been a recurring theme of interest to researchers since it leads to Compression After impact (CAI) phenomena, one of the most critical design tolerance cases in aerospace structures , and has to be analyzed using expensive and time-consuming experiments (Tuo et al., 2019; Yang et al., 2021; Jayaram et al., 2021; WANG and NAGASHIMA, 2022; Knopp et al., 2022; Gemi et al., 2022). Usually, computer model simulations of these problems should be performed together with experimental test programs to corroborate the predictions and build confidence. Experimental and simulation results have been widely analyzed and published, including review articles on the current state of the art, studying issues such as new analytical methods to represent test results (Suemasu, 2016; Caprio et al., 2016; Yin and Iannucci, 2022), the variation of constitutive properties in impact resistance in continuous fibers reinforced composite materials to improve impact properties (Cantwell and Morton, 1991; Justo et al., 2015; Han et al., 2016; Liv et al., 2017; Perillo et al., 2017; Liu et al., 2018; Gopinath and Batra, 2020; Shah, Megat-Yusoff, Karuppanan, Choudhry, Din, Othman, Sharp and Gerard, 2021), determination of the strain fields and failure mechanisms during the failure of the impacted composite laminates when subjected to compression (Kadlec and Kafka, 2015; Liu et al., 2016; Sun and Hallett, 2018; Esaki, 2017; Zhang, 2019; Zou et al., 2021; Zhou et al., 2021), the impact induced crack propagation (Rivallant et al., 2014), and the analysis of these effects in delamination prediction methods (Elder et al., 2004; González et al., 2012), as the contact radius increase due to deflection, delamination, and damage evolution in low velocity impact (Yu and Gao, 2016; Li and Chen, 2016; Abir et al., 2017*a*; Tan et al., 2015*a*,*b*; Richardson and Wisheart, 1996; Feng and Aymerich, 2014; Fatima et al., 2021). Different perspectives, with respective computational cost particularities, can be chosen, as two-dimensional simulations (Davies and Zhang, 1995; Christoforou and Yigit, 2009; Tiberkak et al., 2008) and three-dimensional (Hou et al., 2000; Lin and Waas, 2021). Impact tests may be performed experimentally with different apparatus, as impact

hammer or drop tower (AIT, 2010; ASTM, 2014), as described by Choi and Chang (1992), Gonzales et al. (2009), Olsson (2010), Hazzard et al. (2017), Santiago et al. (2017), and Yasaee et al. (2017).

Special attention needs to be taken, during tests and/or numerical model development, in order deal with and incorporate nonlinear behaviors such as material degradation and large deformations in the results. The impact damage positions effect affects and is affected by the buckling and post-buckling behaviors of stiffened composite panels under axial compression (Feng et al., 2016; Abir et al., 2017*b*). Experimental strain analysis indicated that the outer sublaminate at the damage location presents buckling before the global buckling occurred (Wang et al., 2015). Investigations of buckling, post-buckling and progressive failure of composite laminated plates have been developed numerically and experimentally and, if compared to panels without delamination, interaction of buckling modes reduced panel buckling strains (Rhead et al., 2017; Namdar and Darendeliler, 2017; Zhao et al., 2017). Based in delamination models, studies were able to analyze the load drop force threshold over time due to the damage generated loss of stiffness, verifying the development of interlaminar failure (Schoeppner and Abrate, 2000; Zhang et al., 2017), including intralaminar stress effects in the delamination model (Hou et al., 2001; Panettieri et al., 2016), and numerically demonstrating different delamination mechanisms given by load variation (Aymerich, Lecca and Priolo, 2008; Shor and Vaziri, 2017; bin Du et al., 2021). In order to clearly predict delamination, some studies adopted cohesive hypotheses. These models are composed by a penalty contact, responsible for the initial adhesion of the elements, and the cohesive zone model itself, based on a damage formulation that reduces adhesion forces and tensions due to adjacent delamination (Borg et al., 2004). The adopted laws consist of an initial linear elastic phase, followed by a stage of stiffness linearity loss, that simulates the interface decohesion after the onset of damage. The complete interface fracture occurs when the cohesive traction forces disappear at the end of the decohesive stage

(Aymerich, Dore and Priolo, 2008).

2.3 Macro, Micro and Multiscale Modeling

Laminate orientation and ply arrangement plays an important role in impact and compression after impact results. As an example, the use of thin ply presents direct benefits in terms of increasing laminate orientation possibilities, especially when relatively thin laminates are used, where the orientation possibilities variation are limited by the maximum number of layers. The ply thickness reduction presents advantages such as the reduction of the probability of critical defects, the better control of crack propagation, the controlled improvement of stress distribution due to the sub-laminated scaling or ply-blocking scaling, and improvements in microstructure and processing (Amacher et al., 2014). However, the effect of thickness on the microstructure damage is a subject with dificult approach by conventional techniques, since the analysis will present similar stress magnitudes different thickness laminae when requested by the same axial stress (Sihn, 2007; Caminero et al., 2017; Rozylo et al., 2017; Soto et al., 2018; Caminero et al., 2018; Seamone et al., 2022; van Hoorn et al., 2022). Thus, a tension magnitude based criteria will not be able to predict such effect without a more accurate description of the microstructure (Xu et al., 2021). Ren et al. (2017) proposed a multiscale finite element method for small-deflection analysis of thin composite plates with aperiodic microstructure characteristics, in order to obtain the macroscopic and microscopic response fields.

Considering that full-scale testing is limited due to size and cost restraints, a small-scale coupon impact test program is more suitable to provide the necessary information. In these tests, a flat, rectangular composite coupon plate is subjected to an out-of-plane, concentrated impact load using a drop-weight device with a hemispherical impactor (ASTM, 2012, 2014). The drop-weight potential energy is defined by the specified mass and drop height of the impactor (Fotouhi et al., 2020; Liu, Jiang

and Wen, 2020; Zhang et al., 2020; Meon et al., 2020). Information obtained from computer models and experimental results on the coupon-scale analysis can be then used to investigate the behavior of the full-scale component. These impact studies require the acquaintance of the dynamics of the event, predicting the induced damage extension and estimating the structure residual properties. The obtained results are dependent on a large number of parameters, which generates a large number of possibilities of different models, which can be classified into three main categories with different levels of complexity and applicability (Abrate, 2001): energy equilibrium models, where a quasi-static structural behavior is assumed; spring-mass models, where the structural dynamics is represented in simplified form; complete models, where the dynamic behavior of the structure is fully modeled. It is also observed that, for a constant impact energy, the force and duration of the impact vary with the impactor and structure characteristics, thus influencing the type and extension of material degradation (Christoforou, 2001; Hou et al., 2021; Anuse et al., 2022).

Every structural or natural material has certain fine-scale properties that affect its overall features. However, all those micro-details usually cannot be directly taken into account in modeling since it would result in enormous size and complexity of computation (Cecot and Oleksy, 2015). A transition from the microscopic properties to their macroscopic counterparts, based on an averaging principles, is termed homogenization. The simplest method to obtain homogenized modulus of heterogeneous material is based on the rule of mixture. This approach takes only one microstructural characteristic into consideration: the volume ratio of the heterogeneity (Molina and Curiel-Sosa, 2015). Composite materials have multiple-scale features, thus in order to capture more detailed information, many multiscale methods have been elaborated since 1970's (Xing et al., 2017). In an experimental analysis investigation, as presented by Mortell et al. (2016), the damage mechanisms may be observed from the micro-scale with fibre-matrix debonding and crack coalescence,

to transverse ply fracture at the meso-scale, through to formation of macroscopic delamination.

Montero et al. (2017) proposed a CAI methodology wich starts with material modeling, characterization and qualification using micromechanics theories and constituent material properties (fiber and matrix) at the unit cell level. The composite behavior needs to be calibrated with the experimental data for different loading conditions until a good agreement with the test data is achieved and, once the material is modeled, the structural analysis may be carried out. Applying multiscale models to CAI problems, Yang et al. (2016) proposed a method for the simulation of fibre reinforced polymeric composite laminate subjected to low velocity impact, based on the embedded cell method, with detailed microstructure embedded into the macro laminate beneath the impact point, and a transition zone is introduced to link these two scales, presenting good agreement between the simulation results and available experimental results from literature. Liu et al. (2016) have developed a study of the effects of different failure criteria on the dynamic progressive failure properties of carbon fiber composite laminates. In this work, the intralaminar damage models using three failure criteria are implemented by explicit finite element subroutine (ABAQUS®-VUMAT) and the delamination is simulated by the bilinear cohesive model in Abaqus® on carbon fiber composite specimens with different materials, layups and impact energies to study the impact force- time/displacement curves and the dissipated energy as well as the damage evolution behaviors of the matrix and delamination interface, showing consistency between the three criteria except for differences in matrix cracking and delamination. Lopes et al. (2016) proposed a continuum material model for the simulation of intraply damage phenomena, were delaminations are simulated using of cohesive surfaces. In this work, the use of structured meshes, aligned with fiber directions allowed the physically-sound simulation of matrix cracks parallel to fiber directions, and their interaction with the development of delaminations.

The multiscale approach, such as Micro-Mechanics of Failure (MMF) developed by Prof. Sung Kyu Ha (Ha et al., 2008, 2010), is advantageous to include different material scales in complex problems as impact and fatigue damage, being able to minimize the number of experimental tests required during project development. Considering unit cell models, microstresses in constituents can be calculated from ply stresses and effective properties estimated based on constituent material properties (Figure 2.4). This three-dimensional Micro-Mechanics of Failure model was developed and applied in order to predict triaxial failure envelopes and stress-strain curves for 12 test cases in the Second World-Wide Failure Exercise (WWFE-II) presenting good prediction results for unidirectional and laminate composites under multi-axial loadings (Huang, Jin and Ha, 2012). The original predictions were compared with experimental data, supplied in WWFE-II Part B, enabling the development of improvements and the analysis of discrepancies (Huang, Xu and Ha, 2012). Lou et al. (2017) proposed a multiscale analysis method which combines the micromechanics of failure (MMF) theory for intralaminar damage and cohesive model for interlaminar failure, being able to successfully identify the failure modes of fiber and matrix in microscale as well as delamination. Huang et al. (2011) proposed a MMF based fatigue life prediction, developed for the analysis of polymeric matrix composites.

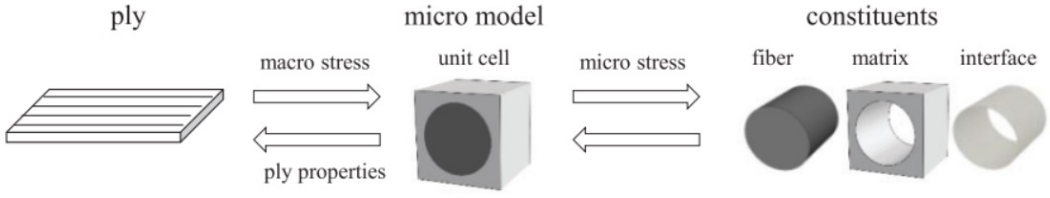

Figure 2.4: Ply and constituents material scale levels (Huang et al., 2020).

Considering a composite laminate, the stress and failure analyses are generally considered at ply level. However, in order to better understand the mechanical

behavior, the micromechanics approach is needed.(Huang et al., 2020). When a unidirectional fibre-reinforced composite is examined microscopically in a plane perpendicular to the fibers in a real world case, the observed fibers in the matrix are usually completely randomly distributed (Li, 1999). Representative volume element (RVE) are commonly built considering boundary conditions which satisfies the periodicity and continuity conditions associated with displacements and force reactions, since they are commonly suitable for multiaxial loads combination, assuming that the fibers are infinitely long and every cross-section of the composite perpendicular to the fibres is identical (Aboudi, 1990; Li, 2001; Xia et al., 2003; Gopinath and Batra, 2020; Vignoli et al., 2022; Zhang et al., 2022). Based on linear stress-strain relations, a micromechanical approach may be developed applying the concept of stress amplification factors, introducing correlations between macro stress and micro stress, mainly applying one of the three different unit cell models shown in Figure 2.5, condidering square, hexagonal, or diamond fiber arrays (Sun and Vaidya, 1996; Jin et al., 2008).

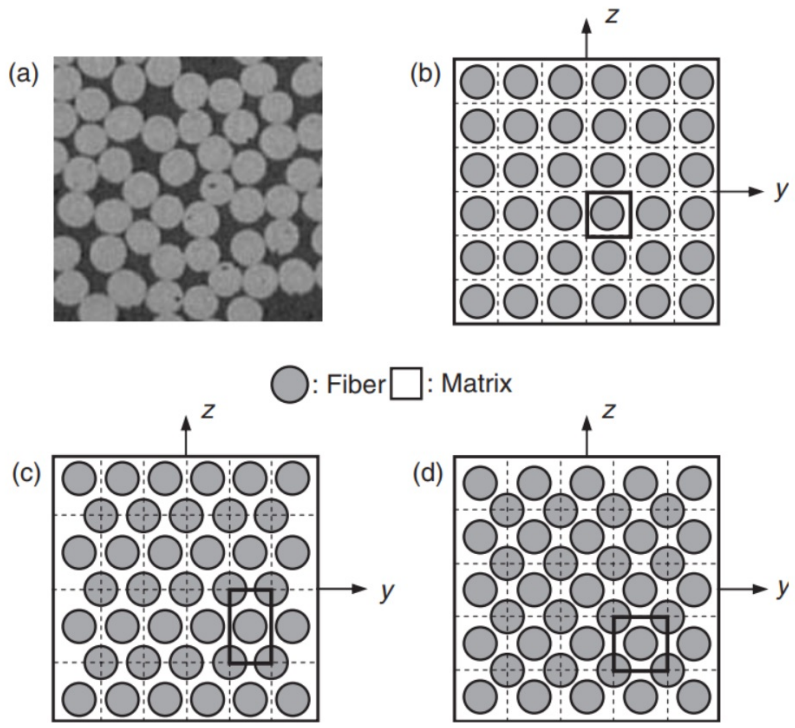

Figure 2.5: Comparison of real fiber arrangement and idealized fiber arrays; (a) Fiber arrangement in real composite, (b) Square fiber array, (c) Hexagonal fiber array, (d) Diamond fiber array. (Jin et al., 2008).

Finite element models of each proposed regular fiber array may be then built as shown in Figure 2.6. These constituent scale models may be paralleled processed to a ply level composite model, receiving the current stress state and providing the degradation information of constituents. Due to effects as randomly distribution of fibers, voids and defects, mechanical properties of the materials tend to have fluctuations indefinite range. This kind of uncertainty in property values can have a significant effect on the stochastic material behavior that can be addressed using methods as Monte Carlo Simulation (Sun and Vaidya, 1996; Yerbolat et al., 2018). The problem complexity when including detailed microscale events leads to increased result quality, but also increases the computational costs when processing these simulations.

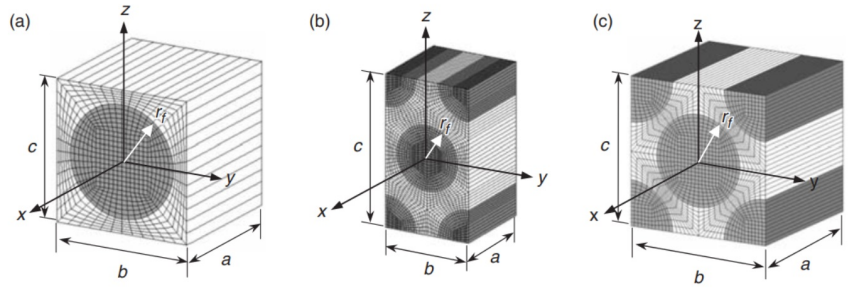

Figure 2.6: Finite element model of regular fiber arrays; (a) Square array, (b) Hexagonal array, (c) Diamond array. (Jin et al., 2008).

Different micromechanical models approximations may be applied in order to reduce the system computational cost and complexity, where a set of composite micromechanics equations is developed for predicting the ply microstresses when the ply stresses are known (Chamis, 1987; Aboudi, 1990; Yerbolat et al., 2018; Huang et al., 2020; Vignoli et al., 2022). A set of equations is then proposed for predicting three-dimensional stresses in the matrix, fiber, and interface (Chamis, 1987). The effective elastic properties of unidirectional composites, based on geometric simplifications and the rule of mixtures (Figure 2.7), are approximated and establishes as closed-form expressions to calculate the effective elastic properties of unidirectional laminae (Yerbolat et al., 2018; Vignoli et al., 2022). The proposed equantions can be used to predict unidirectional composite (ply) geometric, mechanical, thermal and hygral properties using constituent material (fiber/matrix) properties, and may also include approximate equations for predicting effects as moisture absorption, glass transition temperature of wet resins and hygrothermal degradation effects (Chamis, 1983).

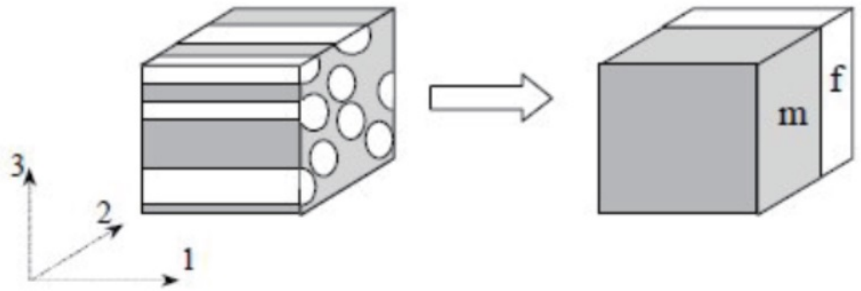

Figure 2.7: Rule of mixtures matrix and fiber volume elements (Yerbolat et al., 2018).

The proposed micromechanics analysis may also be considered as a repeating cell in a fiber-reinforced material, based on the assumption that the unidirectional composite can be represented by aligned fibers distributed regularly in the matrix, forming a doubly periodic array (Figure 2.8). The micromechanical analysis may be then simplified, being performed on this representative cell (Aboudi, 1990, 1991). Elastic properties of unidirectional composites with approximated fiber cross sections may be approximated using different method, applying Finite Element Method (FEM) and experimental data as reference solutions in order to verify the model capability to estimate the elastic properties (Vignoli et al., 2022).

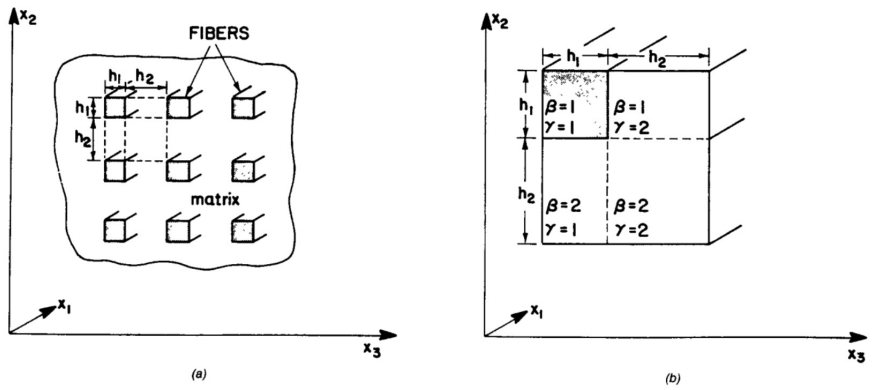

Figure 2.8: (a) Unidirectional fiber composite and (b) representative cell (Aboudi, 1990, 1991).

Besides most analytical micromechanical models being developed using rectangular simplified fiber cross-section for simplification purposes, the fiber geometry presents an important role on the estimation of elastic properties, as proposed in works from Huang et al. (2020) and Vignoli et al. (2022). Huang et al. (2020) proposes a square unit cell model containing a central fiber with an octagonal cross-section, named Octagonal Fiber Model (OFM), wich may be considered a slightly sacrifice the simplicity for more detailed description of micro stress distribution in constituents. The micromechanical unit cell model for continuous fiber reinforced composites, features a fiber with an octagonal cross-section embedded in surrounding matrix, subdivided into five by five sub-regions, as presented in Figure 2.9. The conditions of equilibrium and deformation compatibility were applied to derive expressions for effective ply properties and stress amplification factors, as shown in subsection 3.3.1, which may be applied to correlate ply level stresses to constituint level microstresses in each of the sub-regions, as proposed in section 5.2.

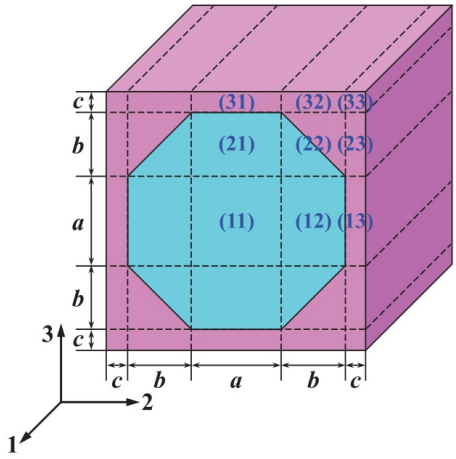

Figure 2.9: Octogonal Fiber Model (OFM) Geometry (Huang et al., 2020).

Chapter 3

Theoretical Basis

This chapter presents a short explanation of classical laminated theory failure criteria (subsection 3.1.1), followed a criteria modification based on Puck and Schurmann (1998) (subsection 3.1.2). Then, in section 3.2, the Cohesive Failure Criteria (section 3.2) used for interlaminar failure simulation is described. Lastly, section 3.3 aims to present the basic concepts necessary to the implementation of the proposed multiscale analysis capabilities, including Octogonal Fiber Model based Stress Amplification Factors applied to obtain fiber, matrix and interface microstresses (subsection 3.3.1), and the respective failure criterias applied for fiber (subsection 3.3.2), matrix (subsection 3.3.3) and interface (subsection 3.3.4).

It is noteworthy that the Hashin's bi-dimensional form criteria, described in subsection 3.1.1, and the cohesive criteria, described in section 3.2, are natively available in Abaqus®. The Puck and Schurmann (1998) modified three dimensional Hashin failure criteria, described in subsection 3.1.2, was implemented in Abaqus® using a VUMAT named *uniFiber.f* (Nie, 2014), wich is available in Abaqus® documentation (Dassault Systemes, 2014). Based on the available VUMAT developed by Nie (2014), the three dimensional Hashin's criteria, described in subsection 3.1.1, was inserted in Abaqus® by means of a modified VUMAT. The proposed multiscale metodology, as described in section 3.3, was also implemented using the same Abaqus® available VUMAT structure (Nie, 2014; Dassault Systemes, 2014) as starting point, and was inserted in Abaqus® by means of a VUMAT.

3.1 Classical Lamina Level Theory Failure Criteria

3.1.1 Hashin Failure Criteria

Hashin damage initiation criteria is applied in order to model anisotropic damage in fiber-reinforced materials. The response of the undamaged material is assumed to be linearly elastic, and the model is intended to predict behaviour of fiber-reinforced materials for which damage can be initiated without a large amount of plastic deformation. The Hashin's initiation criteria are used to predict the onset of damage, and the damage evolution law is based on the energy dissipated during the damage process and linear material softening. Four different modes of failure are considered: fiber rupture in tension; fiber buckling and kinking in compression; matrix cracking under transverse tension and shearing; and matrix crushing under transverse compression and shearing (Hashin, 1980).

Fiber tension ($\sigma_{11} > 0$):

$$F_f^T = \left(\frac{\sigma_{11}}{X_T}\right)^2 + \alpha \times \left(\frac{\sigma_{12}}{S_L}\right)^2 \tag{3.1}$$

$$\text{where } 0 \leq \alpha \leq 1$$

Fiber compression ($\sigma_{11} < 0$):

$$F_f^C = \left(\frac{\sigma_{11}}{X_C}\right)^2 \tag{3.2}$$

Matrix tension ($\sigma_{22} > 0$):

$$F_m^T = \left(\frac{\sigma_{22}}{Y_T}\right)^2 + \left(\frac{\sigma_{12}}{S_L}\right)^2 \tag{3.3}$$

Matrix compression ($\sigma_{22} < 0$):

$$F_m^C = \left(\frac{\sigma_{22}}{2S_T}\right)^2 + \left[\left(\frac{Y_C}{2S_T}\right)^2 - 1\right] \times \frac{\sigma_{22}}{Y_C} + \left(\frac{\sigma_{12}}{S_L}\right)^2 \tag{3.4}$$

In the above equations, X_T denotes the longitudinal tensile strength, X_C denotes the longitudinal compressive strength; Y_T denotes the transverse tensile strength; Y_C denotes the transverse compressive strength; S_L denotes the longitudinal shear strength; S_T denotes the transverse shear strength; α is a coefficient that determines shear stress contribution to the fiber initiation criterion; and σ represents the effective stress, with its components intended to represent the stress acting over the damaged area that effectively resists the internal forces.

The initiation criteria presented above can be specialized to obtain the model proposed in Hashin and Rotem in 1973 (Hashin and Rotem, 1973) by setting $\alpha = 0$ and $S_T = \frac{Y_C}{2}$, or the model proposed in Hashin in 1980 by setting $\alpha = 1$ (Hashin, 1980). An output variable is associated with each initiation criterion (fiber tension, fiber compression, matrix tension, and matrix compression) to indicate whether the criterion has been met. A value of 1.0 or higher indicates that the initiation criterion has been met (Hashin, 1980).

These criteria were originally developed for unidirectional composites, as in the aforementioned configuration, and hence, implemented within two dimensional classical lamination approach for point stress calculations with ply discounting as the material degradation model. Failure indices for Hashin criteria are related to fiber and matrix failures and involve four failure modes. The criteria may be extended to three dimensional problems where the maximum stress criteria are used for transverse normal stress component. The failure modes included in three dimensional Hashin's criteria may be written as follows (Hashin, 1980).

Fiber tension ($\sigma_{11} > 0$):

$$F_f^T = \left(\frac{\sigma_{11}}{X_T}\right)^2 + \left(\frac{\sigma_{12}^2 + \sigma_{13}^2}{S_L^2}\right) \tag{3.5}$$

Fiber compression ($\sigma_{11} < 0$):

$$F_f^C = \left(\frac{\sigma_{11}}{X_C}\right)^2 \tag{3.6}$$

Matrix tension ($\sigma_{22} + \sigma_{33} > 0$):

$$F_m^T = \left(\frac{(\sigma_{22} + \sigma_{33})^2}{Y_T^2} \right) + \left(\frac{\sigma_{23}^2 - \sigma_{22}\sigma_{33}}{S_T^2} \right) + \left(\frac{\sigma_{12}^2 + \sigma_{13}^2}{S_L^2} \right) \tag{3.7}$$

Matrix compression ($\sigma_{22} + \sigma_{33} < 0$):

$$F_m^C = \left[\left(\frac{Y_C}{2S_T} \right)^2 - 1 \right] \times \left(\frac{\sigma_{22} + \sigma_{33}}{Y_C} \right) + \left(\frac{(\sigma_{22} + \sigma_{33})^2}{4S_T^2} \right) + \left(\frac{\sigma_{23}^2 - \sigma_{22}\sigma_{33}}{S_T^2} \right) + \left(\frac{\sigma_{12}^2 + \sigma_{13}^2}{S_L^2} \right) \tag{3.8}$$

This three dimensional Hashin's criteria was inserted in Abaqus® by means of an user-defined material model (Abaqus® VUMAT). This modification was developed during this work in order to evaluate Hashin 3D failure criterion for fiber and matrix, based on the original VUMAT presented in Abaqus® documentation (Dassault Systemes, 2014), implemented using the modified Hashin criteria described in subsection 3.1.2.

3.1.2 Constitutive model proposed by Nie (2014), based on Hashin's failure criteria for unidirectional fiber composites (Hashin, 1980) and on Puck's action plane theory (Puck and Schurmann, 1998)

This failure criteria, implemented for Abaqus® using a VUMAT named *uniFiber.f* (Nie, 2014), which is available in Abaqus® documentation (Dassault Systemes, 2014), is based on Hashin's failure criteria for unidirectional fiber composites (Hashin, 1980), using the constitutive model with minor modifications for fibers. For the matrix failure modes, a constitutive model based on Puck's action plane theory (Puck and Schurmann, 1998) was developed for both tension and compression cases. In this Puck and Schurmann (1998) modified three dimensional Hashin failure criteria, four

distinct failure modes were considered: tensile fiber failure, compressive fiber failure, tensile matrix failure, and compressive matrix failure, expressed mathematically as below (Nie, 2014).

Fiber tension ($\sigma_{11} > 0$):

$$F_f^T = \left(\frac{\sigma_{11}}{X_T}\right)^2 + \left(\frac{\sigma_{12}}{S_{12}}\right)^2 + \left(\frac{\sigma_{13}}{S_{13}}\right)^2 \tag{3.9}$$

Fiber compression ($\sigma_{11} < 0$):

$$F_f^C = \left(\frac{\sigma_{11}}{X_C}\right) \tag{3.10}$$

Matrix tension ($\sigma_{22} + \sigma_{33} > 0$):

$$F_m^T = \left(\frac{\sigma_{11}}{2X_T}\right)^2 + \left(\frac{\sigma_{22}^2}{Y_T Y_C}\right) + \left(\frac{\sigma_{12}}{S_{12}}\right)^2 + \left(\frac{\sigma_{22}}{Y_T Y_C}\right) \tag{3.11}$$

Matrix compression ($\sigma_{22} + \sigma_{33} < 0$):

$$F_m^C = \left(\frac{\sigma_{11}}{2X_T}\right)^2 + \left(\frac{\sigma_{22}^2}{Y_T Y_C}\right) + \left(\frac{\sigma_{12}}{S_{12}}\right)^2 + \left(\frac{\sigma_{22}}{Y_T Y_C}\right) \tag{3.12}$$

where S_{12}, S_{13} and S_{23} denote allowable shear strengths in the respective principal material directions. One may observe that, besides being defined as a material input for this Abaqus® documentation (Dassault Systemes, 2014) available VUMAT (*uniFiber.f*), the transverse shear strength (S_{23}) is not used during the failure criteria.

3.1.3 Damage evolution laws

Considering each of the presented failure onset criteria, different damage evolution approaches may be applied. If considering a brittle failure for fiber breakage under longitudinal tension or compression (no buckling), a simplifies material property degradation model may be applied as proposed by Nie (2014) material. Considering this brittle failure, progressive damage evolution was not considered in

the model in as implemented in Abaqus® available VUMAT named *uniFiber.f* (Nie, 2014; Dassault Systemes, 2014).

On the other hand, a non-binary damage evolution may be proposed focusing on improving numerical stability or even obtaining a more reliable material models. Considering the Abaqus® native two-dimensional Hashin criteria (Hashin, 1980), as described in subsection 3.1.1, the undamaged material response is assumed to be linearly elastic, and the most commonly applied damage evolution law is based on the energy dissipated during the damage process and linear material softening, as shown in Figure 3.1. For each failure mode, the energy dissipated due to failure (G^c equals to OAC area in grey on Figure 3.1 (a)), must be specified, defining G^c_{ft}, G^c_{fc}, G^c_{mt}, and G^c_{mc} as energies dissipated during damage for failure modes in fiber tension, fiber compression, matrix tension, and matrix compression, respectively. Unloading from a partially damaged state (point B in Figure 3.1 (a)), a linear path toward the origin will occur, and the same path is followed back to point B upon reloading (Dassault Systemes, 2014).

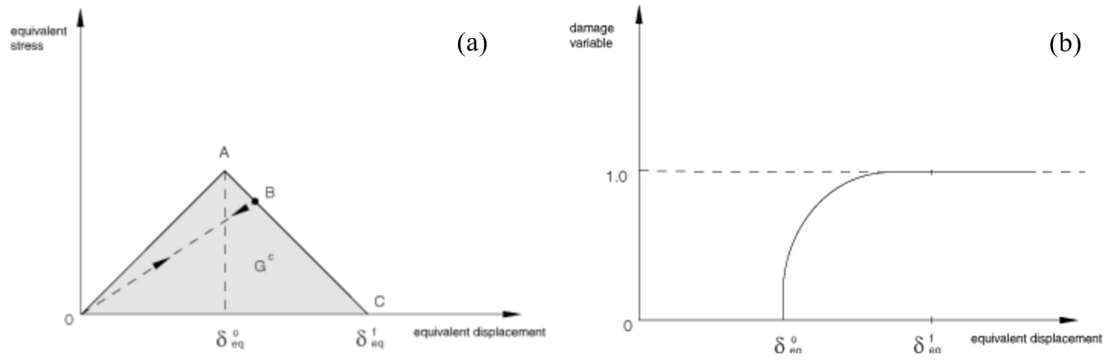

Figure 3.1: (a) Linear energy-based damage evolution and (b) damage variable (Dassault Systemes, 2014).

The damage variable for a particular mode, represented in Figure 3.1 (b), is defined as:

$$d = \frac{\delta_{eq}^{f}\left(\delta_{eq} - \delta_{eq}^{0}\right)}{\delta_{eq}\left(\delta_{eq}^{f} - \delta_{eq}^{0}\right)} \tag{3.13}$$

with initial value of zero (no damage), and gradually increasing until reaching the unitary value from damage onset to final damage. The tensile fiber damage variable ($\sigma_{11} > 0$) can be defined as

$$\delta_{eq}^{ft} = L^{c}\sqrt{\langle\varepsilon_{11}\rangle^{2} + \alpha\varepsilon_{12}^{2}} \tag{3.14}$$

the compressive fiber damage variable ($\sigma_{11} < 0$) as

$$\delta_{eq}^{fc} = L^{c}\langle-\varepsilon_{11}\rangle \tag{3.15}$$

the tensile matrix damage variable ($\sigma_{22} > 0$) as

$$\delta_{eq}^{mt} = L^{c}\sqrt{\langle\varepsilon_{22}\rangle^{2} + \varepsilon_{12}^{2}} \tag{3.16}$$

and the compressive matrix damage variable ($\sigma_{22} < 0$) as

$$\delta_{eq}^{mc} = L^{c}\sqrt{\langle-\varepsilon_{22}\rangle^{2} + \varepsilon_{12}^{2}} \tag{3.17}$$

The characteristic element length L_c is defined in order to alleviate mesh dependency during material softening. For membranes and shells it is computed as the square root of the measured area in the reference surface (Dassault Systemes, 2014). The post-damage initiation material response behavior may be expressed as:

$$\sigma = C_{d}\varepsilon \tag{3.18}$$

where ε is the strain, C_d is the damaged elasticity matrix, defined as:

$$C_{d} = \frac{1}{D}\begin{bmatrix} (1-d_f)E_1 & (1-d_f)(1-d_m)v_{12}E_1 & 0 \\ (1-d_f)(1-d_m)v_{12}E_1 & (1-d_m)E_2 & 0 \\ 0 & 0 & (1-d_s)GD \end{bmatrix} \tag{3.19}$$

And defining D as:

$$D = 1 - (1 - d_f)(1 - d_m) v_{12} v_{21} \tag{3.20}$$

The damage variable d_f represents the current state of fiber damage variable, and d_m the current state of matrix damage variable, both according the traction or compression status of each direction. Also, d_s is the current state of shear damage variable, defined as:

$$d_s = 1 - \left(1 - d_f^t\right)\left(1 - d_f^c\right)\left(1 - d_m^t\right)\left(1 - d_m^c\right) \tag{3.21}$$

3.2 Mesoscale Interply Cohesive Failure Criteria

Complementarily to the intralaminar failure criteria, it is proposed the use an interlaminar criteria, since delamination, as a result of impact, or even due to manufacturing defects, can cause a significant reduction in the compressive load-carrying capacity of a structure (Camanho and Davila, 2002). The cohesive damage initiation refers to the beginning of cohesive response degradation at a contact point, which begins when the contact stresses and/or contact separations satisfy the specified damage initiation criteria, as presented below:

Maximum stress criterion - Damage is assumed to initiate when the maximum contact stress ratio (as defined in the expression below) reaches a value of one. This criterion can be represented as (Dassault Systemes, 2014):

$$max\left\{\frac{< t_n >}{t_n^o}, \frac{t_s}{t_s^o}, \frac{t_t}{t_t^o}\right\} = 1 \tag{3.22}$$

Maximum separation criterion - Damage is assumed to initiate when the maximum separation ratio (as defined in the expression below) reaches a value of one. This criterion can be represented as (Dassault Systemes, 2014):

$$max\left\{\frac{<\delta_n>}{\delta_n^o}, \frac{\delta_s}{\delta_s^o}, \frac{\delta_t}{\delta_t^o}\right\} = 1 \tag{3.23}$$

Quadratic stress criterion - Damage is assumed to initiate when a quadratic interaction function involving the contact stress ratios (as defined in the expression below) reaches a value of one. This criterion can be represented as (Dassault Systemes, 2014):

$$\left\{\frac{<t_n>}{t_n^o}\right\}^2 + \left\{\frac{t_s}{t_s^o}\right\}^2 + \left\{\frac{t_t}{t_t^o}\right\}^2 = 1 \tag{3.24}$$

Quadratic separation criterion - Damage is assumed to initiate when a quadratic interaction function involving the separation ratios (as defined in the expression below) reaches a value of one. This criterion can be represented as (Dassault Systemes, 2014):

$$\left\{\frac{<\delta_n>}{\delta_n^o}\right\}^2 + \left\{\frac{\delta_s}{\delta_s^o}\right\}^2 + \left\{\frac{\delta_t}{\delta_t^o}\right\}^2 = 1 \tag{3.25}$$

Where $\mathbf{t}$ is the nominal traction stress vector, and δ the correspondent separations in normal and first/second shear directions (n, s and t respectively). The Macaulay brackets (<>) are used to signify that a purely compressive displacement (i.e., a contact penetration) or a purely compressive stress state does not initiate damage.

The cohesive material response was developed based on Benzeggagh-Kenane fracture criterion (Dassault Systemes, 2014; Benzeggagh and Kenane, 1996), given by

$$G_n^C + \left(G_S^C - G_n^C\right)\left\{\frac{G_S}{G_T}\right\}^\eta = G^C, \tag{3.26}$$

where G_n, G_s, and G_t stands for the work done by the traction and their conjugate relative displacements in the normal, first, and second shear directions, $G_S = G_s + G_t$, $G_T = G_n + G_S$, and η is a material parameter-based exponent. Figure 3.2 shows traction (vertical axis) versus the magnitudes of the normal and the shear separations (two horizontal axes). The unshaded triangles in the two vertical

coordinate planes are the response under pure normal and pure shear deformation, and intermediate vertical planes stands for a damage response under mixed mode conditions. Again, unloading from a partially damaged state occurs along a linear path toward the origin, and the same path is followed back upon reloading (Dassault Systemes, 2014).

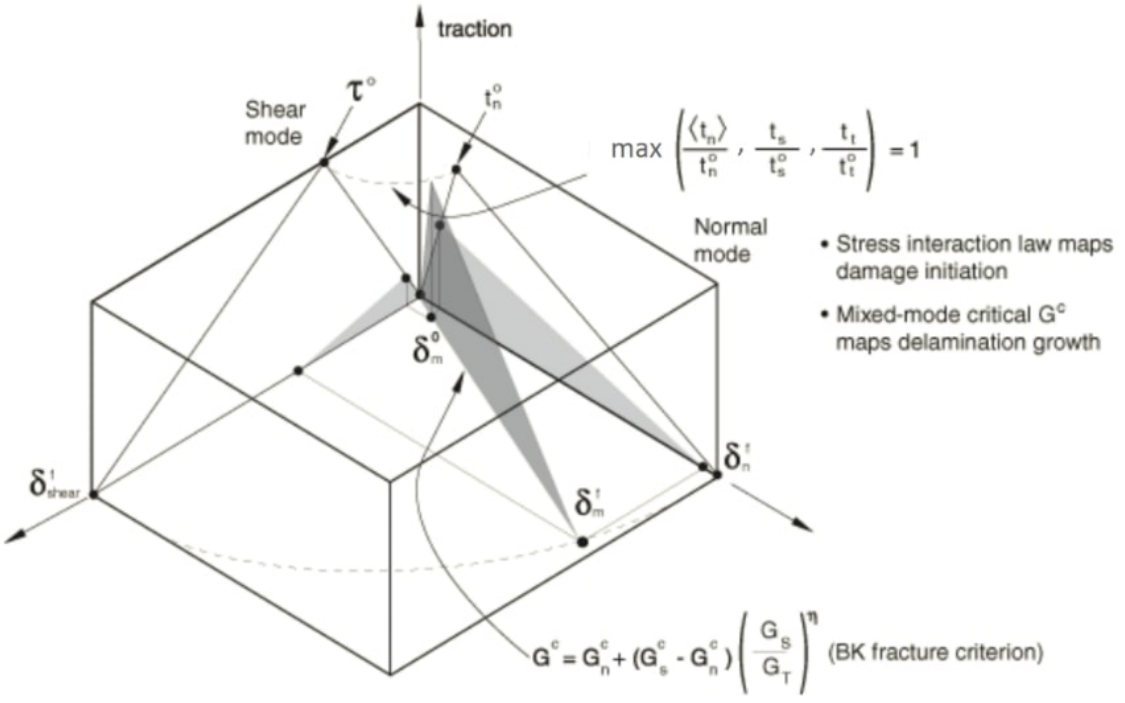

Figure 3.2: Mixed-mode response in cohesive elements - Adapted from Abaqus® CAE user's manual (Dassault Systemes, 2014)

3.3 Microscale and Multiscale Analysis

Due to the microstructural randomness of composites, the main emphasis of research was on the determination of their overall properties that could allow its use in a deterministic continuous descriptions. In other words, an inhomogeneous material (discrete medium) is substituted by an equivalent homogenous one (continuous

medium). This can be implemented by means of homogenisation procedures (Kwon et al., 2007).

In other hand, microstructural (local) randomness of heterogeneous materials does affect their response at the macroscopic (global) level. The increase in the considered control area, in local scale, reduces the effects of properties' fluctuations, working as an averaging procedure. On the other hand, mechanisms causing spatial localisation of deformation and/or fracture processes, for instance, plastic flow and crack nucleation and/or propagation, inherit some of the randomness of the microscopic structure (Kwon et al., 2007). The transversal arrangements of fibers randomness, as seen in Figure 3.3, when analysed in layers of real composites, are a very difficult task to characterize in both micro and macro scales.

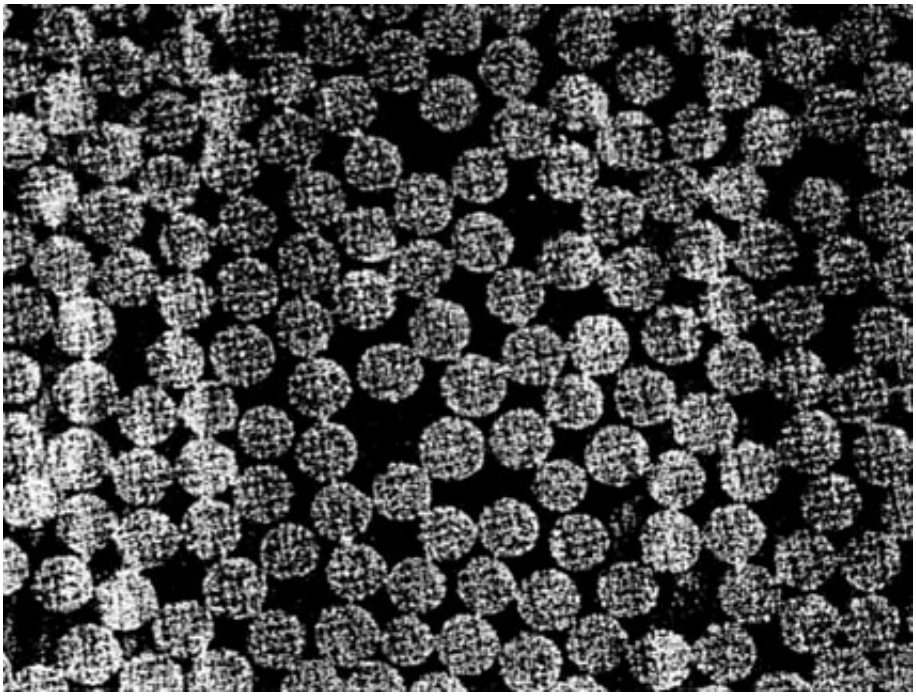

Figure 3.3: Photomicrograph of Carbon-Epoxy composite material (Daniel and Ishai, 2005).

In a micromechanical scale, composites have the advantage of high-stiffness and

high-strength fiber, whose usually low toughness is enhanced by the matrix ductility and by the energy dissipation at the fiber/matrix interface. The matrix stress transfer capability enables the development of multiple-site and multiple path failure mechanisms. The conventional used macromechanical analysis treats the material as quasi-homogeneous, using its anisotropy to control and predict the material behaviour based on properties of the constituents. The mechanical characterization requires the input of average material characteristics, obtained by experimental verification of the analysis or by a extensive test program for determination of a large number of mean engineering parameters (Daniel and Ishai, 2005).

Taking as an example the comparison in the mechanical performance of thick-ply and thin-ply composites, one may observe several sources of size effects (Amacher et al., 2014), such as volume and probability of critical defects, where the strength of a composite part may be related to the probability of finding a critical defect; the crack propagation controlled mechanisms, being the ultimate strength of a composite structure expected to be inversely proportional to the square root of the characteristic size of the crack, which is bounded by the ply thickness in the case of an intra-laminar crack constrained by the surrounding plies; Laminate scaling, where up-scaling in laminate thickness can be achieved by either changing the number of identical plies in the laminate thickness (laminate block scaling) or by repeating the lay-up sequence several times using a single ply for each orientation (sub-laminate scaling), triggering of different failure mechanisms; and the micro-structure and processing generated residual strains, fiber alignment and waviness, porosity and the amount of fiber clustering, as well as resin rich zones.

The direct introduction of stochastic microscopic features into computational models is, due to extremely high computational costs, prohibitive and counterproductive. A significantly better strategy is to employ multi-scale models that separate the levels of descriptions into (at least) local and global ones. The local level is used

to incorporate data from composites micro-structure and the global one takes in account the geometry of composite components/structures and loading/environmental conditions to study problems of their macroscopic behavior, structural integrity and/or durability. The diversity of composites (in terms of constituents, their morphology and a type of reinforcement) makes a general analysis of their behavior, including damage accumulation, practically infeasible (Kwon et al., 2007), generating the need for specific methodologies for different problems to be addressed, such as the Compression After Impact analysis methodology proposed in this work.

3.3.1 Octogonal Fiber Model

In a cost-effective strategy in multiscale modelling to integrate the local and global levels of descriptions, Stress Amplification Factors (SAF), expressed as M_{ij} in Equation 3.27, may be defined as the relationship between ply stresses, at macroscale level, and microstresses in fiber and matrix constituents, at microscale level (Jin et al., 2008; Huang et al., 2020). This relationship can be expressed by equation at a certain material point inside a constituent, while $\bar{\sigma}$ and σ represent ply stresses and microstresses at the same material point, respectively. In the following equations the subscript "c" stands for constituent, which can be either "f" for fiber, "m" for matrix, and "i" for interface; the superscripts "ij" denote sub-regions in OFM.

$$\left(\sigma_i \right) = \left[M_{ij} \right]_{\mathbf{c}} \left(\bar{\sigma}_j \right) \tag{3.27}$$

The micro-tractions at a point located at the fiber-matrix interface can be obtained by transforming the micro-stresses at a point inside matrix and in the neighborhood of the aforesaid interfacial point, as defined in Equation 3.28.

$$\left(t_i \right) = \left[M_{ij} \right]_{\mathrm{i}} \left(\bar{\sigma}_j \right) \tag{3.28}$$

Where:

$$\begin{pmatrix} t_1 \\ t_2 \\ t_3 \end{pmatrix} = \begin{pmatrix} \tau_x \\ \sigma_n \\ \tau_t \end{pmatrix} \tag{3.29}$$

It is important to notice that, as described in Figure 3.4), the Stress Amplification Factor matrix built for interface case will be used to achieve shear values on the interface plane, and a normal traction.

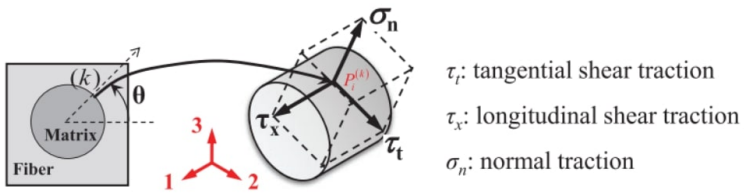

Figure 3.4: Microstresses at interface between the fiber and matrix (Huang et al., 2020).

The Octagonal Fiber Model (OFM) micromechanical unit cell, developed by Huang et al. (2020) for continuous fiber reinforced composites, features an octagonal fiber cross-section approximation embedded in surrounding matrix. Considering this approximation, a square unit cell model may be divided into 5-by-5 sub-regions (Figure 3.5), where the blue octagonal area represents the fiber and purple area represents the matrix.

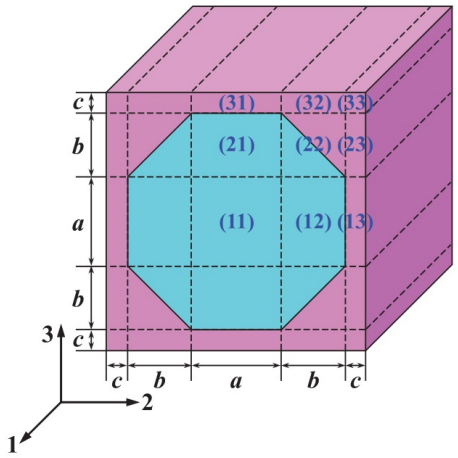

Figure 3.5: Geometry of the OFM (Huang et al., 2020).

Considering unitary width and height for the OFM cell, a transversely isotropic fiber, an isotropic matrix, and that among 25 sub-regions shown in Figure 3.5, only nine are independent, which are highlighted by blue numeric superscripts (ij). Huang et al. (2020) demonstrated the expressions of effective ply properties and Stress Amplification Factors at each of these sub-regions. Also, the following equalities due to the material symmetry and the geometric symmetry of OFM were utilized to simplify this derivation, where E, G, v represent elastic modulus, shear modulus, and Poisson's ratio, respectively.

$$
\begin{aligned}
&\bar{E}_2 = \bar{E}_3 \\
&\bar{v}_{21} = \bar{\nu}_{31}, \quad \bar{\nu}_{12} = \bar{\nu}_{13}, \quad \bar{\nu}_{32} = \bar{\nu}_{23} \\
&\bar{G}_5 = \bar{G}_6, \qquad \bar{G}_4 = \frac{\bar{E}_2}{2\left(1 + \bar{v}_{32}\right)} \\
&M_{\mathrm{c22}}^{(ij)} = M_{\mathrm{c33}}^{(ji)}, \quad M_{\mathrm{c21}}^{(ij)} = M_{\mathrm{c31}}^{(ji)}, \\
&M_{\mathrm{c12}}^{(ij)} = M_{\mathrm{c13}}^{(ji)}, \quad M_{\mathrm{c23}}^{(ij)} = M_{\mathrm{c32}}^{(ji)}, \\
&M_{\mathrm{c44}}^{(ij)} = M_{\mathrm{c44}}^{(ji)}, \quad M_{\mathrm{c55}}^{(ij)} = M_{\mathrm{c66}}^{(ji)}
\end{aligned}
\tag{3.30}
$$

The main results of SAFs derivation for OFM sub-regions, developed by Huang et al. (2020), were reproduced bellow, thus indicating the full article for more details.

SAFs relating the microlongitudinal stresses in constituents to ply longitudinal stress are defined as:

$$\begin{cases} M_{\mathrm{f11}}^{(ij)} \equiv \frac{\sigma_{\mathrm{f1}}^{(ij)}}{\bar{\sigma}_1} = \frac{\sigma_{\mathrm{f1}}}{\bar{\sigma}_1} = \frac{E_{\mathrm{f1}}\bar{\varepsilon}_1}{\bar{E}_1\bar{\varepsilon}_1} = \frac{E_{\mathrm{fl}}}{\bar{E}_1} \\ M_{\mathrm{m11}}^{(ij)} \equiv \frac{\sigma_{\mathrm{m1}}^{(ij}}{\bar{\sigma}_1} = \frac{\sigma_{\mathrm{m1}}}{\bar{\sigma}_1} = \frac{E_{\mathrm{m}}\bar{\varepsilon}_1}{\bar{E}_1\bar{\varepsilon}_1} = \frac{E_{\mathrm{m}}}{\bar{E}_1} \end{cases} \tag{3.31}$$

SAFs relating micro transverse stresses in subregions to ply longitudinal stress are defined as:

$$\begin{cases} M_{\mathrm{c21}}^{(1j)} \equiv \frac{\sigma_2^{(1)}}{\bar{\sigma}_1} = \frac{(a+2b)(v_{\mathrm{f21}}-v_{\mathrm{m}})+(v_{\mathrm{m}}-\bar{v}_{21})}{(a+2b)h_1+1}\frac{\hat{E}_{\mathrm{m}}}{\bar{E}_1} \\ M_{\mathrm{c21}}^{(2j)} \equiv \frac{\sigma_2^{(2)}}{\bar{\sigma}_1} = \frac{(a+b)(v_{\mathrm{f21}}-v_{\mathrm{m}})+(v_{\mathrm{m}}-\bar{v}_{21})}{(a+b)h_1+1}\frac{\hat{E}_{\mathrm{m}}}{\bar{E}_1} \\ M_{\mathrm{c21}}^{(3j)} \equiv \frac{\sigma_2^{(3)}}{\bar{\sigma}_1} = \left(v_{\mathrm{m}} - \bar{v}_{21}\right)\frac{\hat{E}_{\mathrm{m}}}{\bar{E}_1} \end{cases} \tag{3.32}$$

SAFs correlating micro transverse stresses in sub-regions with ply transverse stress are defined as:

$$\begin{cases} M_{\mathrm{c22}}^{(1j)} \equiv \frac{\sigma_2^{(1)}}{\bar{\sigma}_2} = \frac{1}{(a+2b)h_2+1}\frac{\tilde{E}_{\mathrm{m}}}{\bar{E}_2} \\ M_{\mathrm{c22}}^{(2j)} \equiv \frac{\sigma_2^{(2)}}{\bar{\sigma}_2} = \frac{1}{(a+b)h_2+1}\frac{\tilde{E}_{\mathrm{m}}}{\bar{E}_2} \\ M_{\mathrm{c22}}^{(3j)} \equiv \frac{\sigma_2^{(3)}}{\bar{\sigma}_2} = \frac{\tilde{E}_{\mathrm{m}}}{\bar{E}_2} \end{cases} \tag{3.33}$$

SAFs correlating micro through-thickness stresses in sub-regions with ply transverse stress are defined as:

$$\begin{cases} M_{\mathrm{c32}}^{(i1)} \equiv \frac{\sigma_3^{(1)}}{\bar{\sigma}_2} = \frac{d_1-(\bar{v}_{21}\bar{v}_{12}+\bar{v}_{32})/\bar{E}_2}{(a+2b)h_2+1}\tilde{E}_{\mathrm{m}} \\ M_{\mathrm{c32}}^{(i2)} \equiv \frac{\sigma_3^{(2)}}{\bar{\sigma}_2} = \frac{d_2-(\bar{v}_{21}\bar{v}_{12}+\bar{v}_{32})/\bar{E}_2}{(a+b)h_2+1}\tilde{E}_{\mathrm{m}} \\ M_{\mathrm{c32}}^{(i3)} \equiv \frac{\sigma_3^{(3)}}{\bar{\sigma}_2} = \left(d_3 - \frac{\bar{v}_{21}\bar{v}_{12}+\bar{v}_{32}}{\bar{E}_2}\right)\tilde{E}_{\mathrm{m}} \end{cases} \tag{3.34}$$

SAFs associating micro longitudinal stresses in sub-regions with ply transverse stress are defined as:

$$\begin{cases} M_{\mathrm{f12}}^{(1j)} \equiv \frac{\sigma_{\mathrm{f1}}^{(1)}}{\bar{\sigma}_2} = v_{\mathrm{f21}}M_{\mathrm{c22}}^{(1j)} - \bar{v}_{12}\frac{E_{\mathrm{f1}}}{\bar{E}_2} \\ M_{\mathrm{m12}}^{(1j)} \equiv \frac{\sigma_{\mathrm{m}}^{(1)}}{\bar{\sigma}_2} = v_{\mathrm{m}}M_{\mathrm{c22}}^{(1j)} - \bar{v}_{12}\frac{E_{\mathrm{m}}}{\bar{E}_2} \\ M_{\mathrm{f12}}^{(2j)} \equiv \frac{\sigma_{\mathrm{fl}}^{(2)}}{\bar{\sigma}_2} = v_{\mathrm{f21}}M_{\mathrm{c22}}^{(2j)} - \bar{v}_{12}\frac{E_{\mathrm{fl}}}{\bar{E}_2} \\ M_{\mathrm{m12}}^{(2j)} \equiv \frac{\sigma_{\mathrm{m}}^{(2)}}{\bar{\sigma}_2} = v_{\mathrm{m}}M_{\mathrm{c22}}^{(2j)} - \bar{v}_{12}\frac{E_{\mathrm{m}}}{\bar{E}_2} \\ M_{\mathrm{m12}}^{(3j)} \equiv \frac{\sigma_{\mathrm{m}}^{(3)}}{\bar{\sigma}_2} = v_{\mathrm{m}}M_{\mathrm{c22}}^{(3j)} - \bar{v}_{12}\frac{E_{\mathrm{m}}}{\bar{E}_2} \end{cases} \tag{3.35}$$

SAFs associating micro in-plane shear stresses with ply in-plane shear stress are defined as:

$$\begin{cases} M_{\mathrm{c66}}^{(1j)} \equiv \frac{\sigma_6^{(1)}}{\bar{\sigma}_6} = \frac{1}{(a+2b)h_3+1}\frac{G_{\mathrm{m}}}{\bar{G}_6} \\ M_{\mathrm{c66}}^{(2j)} \equiv \frac{\sigma_6^{(2)}}{\bar{\sigma}_6} = \frac{1}{(a+b)h_3+1}\frac{G_{\mathrm{m}}}{\bar{G}_6} \\ M_{\mathrm{c66}}^{(3j)} \equiv \frac{\sigma_6^{(3)}}{\bar{\sigma}_6} = \frac{G_{\mathrm{m}}}{\bar{G}_6} \end{cases} \tag{3.36}$$

SAFs correlating micro transverse shear stresses with ply transverse shear stress are defined as:

$$\begin{cases} M_{\mathrm{c44}}^{(i)} \equiv \frac{\sigma_4^{(1)}}{\bar{\sigma}_4} = \frac{1}{(a+2b)h_4+1}\frac{G_{\mathrm{m}}}{\bar{G}_4} \\ M_{\mathrm{c44}}^{(i2)} \equiv \frac{\sigma_4^{(2)}}{\bar{\sigma}_4} = \frac{1}{(a+b)h_4+1}\frac{G_{\mathrm{m}}}{\bar{G}_4} \\ M_{\mathrm{c44}}^{(i3)} \equiv \frac{\sigma_4^{(3)}}{\bar{\sigma}_4} = \frac{G_{\mathrm{m}}}{\bar{G}_4} \end{cases} \tag{3.37}$$

In order to visually simplify the SAF equations presented above, some OFM based definitions were defined. Each of this equations are also described in Huang et al. (2020). Considering that the matrix is isotropic it's possible to define:

$$\begin{aligned} &E_{\mathrm{m1}} = E_{\mathrm{m2}} = E_{\mathrm{m3}} = E_{\mathrm{m}} \\ &v_{\mathrm{m21}} = v_{\mathrm{m31}} = v_{\mathrm{m12}} = v_{\mathrm{m13}} = v_{\mathrm{m32}} = v_{\mathrm{m23}} = v_{\mathrm{m}} \\ &G_{\mathrm{m4}} = G_{\mathrm{m5}} = G_{\mathrm{m6}} = G_{\mathrm{m}} = \frac{E_{\mathrm{m}}}{2\left(1+v_{\mathrm{m}}\right)} \end{aligned} \tag{3.38}$$

The effective ply longitudinal elastic modulus may be obtained.

$$\bar{E}_1 = E_{\mathrm{fl}}V_{\mathrm{f}} + E_{\mathrm{m}}V_{\mathrm{m}} \tag{3.39}$$

The effective ply major Poisson's ratio was obtained as:

$$\bar{v}_{21} = \frac{(a+2b)m_1 + (a+b)m_2}{m_1+m_2+m_3}\left(v_{\mathrm{f21}} - v_{\mathrm{m}}\right) + v_{\mathrm{m}} \tag{3.40}$$

Defining:

$$
\begin{aligned}
&m_1 \equiv a\left[(a+b)h_1+1\right], \quad m_2 \equiv 2b\left[(a+2b)h_1+1\right] \\
&m_3 \equiv 2c\left[(a+b)h_1+1\right]\left[(a+2b)h_1+1\right] \\
&h_1 \equiv \frac{\hat{E}_{\mathrm{m}}}{\hat{E}_{\mathrm{f2}}}-1, \quad \hat{E}_{\mathrm{f2}} \equiv \frac{E_{\mathrm{f2}}}{1-v_{\mathrm{f32}}}, \quad \hat{E}_{\mathrm{m}} \equiv \frac{E_{\mathrm{m}}}{1-v_{\mathrm{m}}}
\end{aligned}
\tag{3.41}
$$

The effective ply transverse elastic modulus E2 can be expressed as:

$$
\bar{E}_2 = \tilde{E}_{\mathrm{m}}\left[\frac{a}{(a+2b)h_2+1}+\frac{2b}{(a+b)h_2+1}+2c\right] \tag{3.42}
$$

Defining:

$$
h_2 \equiv \frac{\tilde{E}_{\mathrm{m}}}{\tilde{E}_{\mathrm{f2}}}-1, \quad \tilde{E}_{\mathrm{f2}} \equiv \frac{E_{\mathrm{f2}}}{1-v_{\mathrm{f21}}v_{\mathrm{f12}}}, \quad \tilde{E}_{\mathrm{m}} \equiv \frac{E_{\mathrm{m}}}{1-v_{\mathrm{m}}^2} \tag{3.43}
$$

The effective ply transverse Poisson's ratio can be obtained

$$
\bar{v}_{32} = \frac{n_1 d_1 + n_2 d_2 + n_3 d_3}{n_1+n_2+n_3}\bar{E}_2 - \bar{v}_{21}\bar{v}_{12} \tag{3.44}
$$

Defining:

$$
\begin{aligned}
&n_1 \equiv a\left[(a+b)h_2+1\right], \quad n_2 \equiv 2b\left[(a+2b)h_2+1\right] \\
&n_3 \equiv 2c\left[(a+b)h_2+1\right]\left[(a+2b)h_2+1\right] \\
&d_1 \equiv aM_{\mathrm{c22}}^{(1j)}\frac{\tilde{v}_{\mathrm{f32}}}{E_{\mathrm{f2}}}+2bM_{\mathrm{c22}}^{(2j)}\frac{\tilde{v}_{\mathrm{f32}}}{E_{\mathrm{f2}}}+2cM_{\mathrm{c22}}^{(3j)}\frac{\tilde{v}_{\mathrm{m}}}{E_{\mathrm{m}}} \\
&d_2 \equiv aM_{\mathrm{c22}}^{(1j)}\frac{\tilde{v}_{\mathrm{f32}}}{E_{\mathrm{f2}}}+bM_{\mathrm{c22}}^{(2j)}\left(\frac{\tilde{v}_{\mathrm{f32}}}{E_{\mathrm{f2}}}+\frac{\tilde{v}_{\mathrm{m}}}{E_{\mathrm{m}}}\right)+2cM_{\mathrm{c22}}^{(3j)}\frac{\tilde{v}_{\mathrm{m}}}{E_{\mathrm{m}}} \\
&d_3 \equiv \frac{\tilde{v}_{\mathrm{m}}}{E_{\mathrm{m}}}, \quad \tilde{v}_{\mathrm{f32}} \equiv v_{\mathrm{f21}}v_{\mathrm{f12}}+v_{\mathrm{f32}}, \quad \tilde{v}_{\mathrm{m}} \equiv v_{\mathrm{m}}\left(1+v_{\mathrm{m}}\right)
\end{aligned}
\tag{3.45}
$$

The effective ply minor Poisson's ratio can be obtained as:

$$
\bar{v}_{12} = \frac{\left\{\begin{array}{l}\left[a(a+2b)v_{\mathrm{f21}}+2acv_{\mathrm{m}}\right]M_{\mathrm{c22}}^{(1j)} \\ +\left[2b(a+b)v_{\mathrm{f21}}+2b(b+2c)v_{\mathrm{m}}\right] \\ M_{\mathrm{c22}}^{(2j)}+2c(a+2b+2c)v_{\mathrm{m}}M_{\mathrm{c22}}^{(3j)}\end{array}\right\}}{\left\{\begin{array}{c}\left[a(a+2b)+2b(a+b)\right]E_{\mathrm{f1}} \\ +\left[2ac+2b(b+2c)+2c(a+2b+2c)\right]E_{\mathrm{m}}\end{array}\right\}}\bar{E}_2 \tag{3.46}
$$

The effective ply in-plane shear modulus may be written as:

$$\bar{G}_6 = G_{\mathrm{m}} \left[\frac{a}{(a+2b)h_3 + 1} + \frac{2b}{(a+b)h_3 + 1} + 2c \right] \tag{3.47}$$

Defining:

$$h_3 \equiv \frac{G_{\mathrm{m}}}{G_{\mathrm{f6}}} - 1 \tag{3.48}$$

And the expression of the effective ply transverse shear modulus may be written as:

$$\bar{G}_4 = G_{\mathrm{m}} \left[\frac{a}{(a+2b)h_4 + 1} + \frac{2b}{(a+b)h_4 + 1} + 2c \right] \tag{3.49}$$

Defining:

$$h_4 \equiv \frac{G_{\mathrm{m}}}{G_{\mathrm{f4}}} - 1 \tag{3.50}$$

Based on OFM aproximation, its possible to verify the damage onset considering fiber, matrix and interface microstresses separately as presented respectively in subsection 3.3.2, subsection 3.3.3 and subsection 3.3.4.

3.3.2 Fiber maximum longitudinal stress failure criterion

As proposed by Ha et al. (2008), a quadratic failure criterion for fiber, similar to the Tsai-Wu failure criterion for ply is adopted considering transversely isotropic reinforcing fibers and high tensile and compressible strengths, in the longitudinal direction, compared to strengths in transverse directions. The defined interactive terms are determined so that the quadratic failure criterion is equivalent to the generalized von Mises failure criterion when only the two normal stress components are not zero.

$$\sum_{j=1}^{6} \sum_{i=1}^{6} F_{ij} \sigma_i \sigma_j + \sum_{i=1}^{6} F_i \sigma_i = 1 \tag{3.51}$$

Defining the coefficients as:

$$
\begin{aligned}
&F_{11} = \frac{1}{X_f X'_f}, \quad F_{22} = F_{33} = \frac{1}{Y_f Y'_f}, \quad F_{44} = \frac{1}{S^2_{f4}}, \quad F_{55} = F_{66} = \frac{1}{S^2_{f6}}, \\
&F_1 = \frac{1}{X_f} - \frac{1}{X'_f}, \quad F_2 = F_3 = \frac{1}{Y_f} - \frac{1}{Y'_f}, \quad F_{23} = F_{32} = -\frac{1}{2Y_f Y'_f}, \\
&F_{12} = F_{21} = -\frac{1}{2\sqrt{X_f X'_f Y_f Y'_f}}, \quad F_{13} = F_{31} = -\frac{1}{2\sqrt{X_f X'_f Y_f Y'_f}}
\end{aligned}
\tag{3.52}
$$

where $X_f, X'_f, Y_f, Y'_f, S_{f4}$, and S_{f6} are longitudinal tensile, longitudinal compressive, transverse tensile, transverse compressive, transverse shear, and longitudinal shear strengths of the fiber, respectively.

All transverse and shear stresses terms can be removed from the fiber failure criterion considering longitudinally continuous fibers with higher modulus and strength than those of matrix, which indicates that fiber supports almost the entire longitudinal tensile load applied to a ply, and that the strengths of matrix are major factors in determining ply strengths under those circumstances. Also this simplification is useful since that transverse tensile and compressive fiber strengths are difficult to measure through experiments. No material property degradation model is applied, since considering a brittle behavior for fiber breakage under longitudinal tension or compression (no buckling). The simplified fiber failure criterion becomes the maximum longitudinal stress failure criterion Ha et al. (2008).:

$$
-X'_f < \sigma_x < X_f \tag{3.53}
$$

3.3.3 Matrix Failure Criteria

Considering a tensor for general stress state,

$$
\begin{bmatrix}
\sigma_x & \tau_{xy} & \tau_{zx} \\
\tau_{xy} & \sigma_y & \tau_{yz} \\
\tau_{zx} & \tau_{yz} & \sigma_z
\end{bmatrix}
\tag{3.54}
$$

The first, second, and third stress invariants may be expressed as:

$$
\begin{aligned}
I_1 &= \sigma_{kk} = \mathrm{tr}(\boldsymbol{\sigma}) \\
&= \sigma_{11} + \sigma_{22} + \sigma_{33} \\
&= \sigma_x + \sigma_y + \sigma_z \\
I_2 &= \begin{vmatrix} \sigma_{22} & \sigma_{23} \\ \sigma_{32} & \sigma_{33} \end{vmatrix} + \begin{vmatrix} \sigma_{11} & \sigma_{13} \\ \sigma_{31} & \sigma_{33} \end{vmatrix} + \begin{vmatrix} \sigma_{11} & \sigma_{12} \\ \sigma_{21} & \sigma_{22} \end{vmatrix} \\
&= \sigma_{11}\sigma_{22} + \sigma_{22}\sigma_{33} + \sigma_{11}\sigma_{33} - \sigma_{12}^2 - \sigma_{23}^2 - \sigma_{31}^2 \\
&= \frac{1}{2}\left(\sigma_{ii}\sigma_{jj} - \sigma_{ij}\sigma_{ji}\right) = \frac{1}{2}\left[(\mathrm{tr}(\sigma))^2 - \mathrm{tr}\left(\sigma^2\right)\right] \\
&= \sigma_x\sigma_y + \sigma_y\sigma_z + \sigma_z\sigma_x - \tau_{xy}^2 - \tau_{yz}^2 - \tau_{zx}^2 \\
I_3 &= \det\left(\sigma_{ij}\right) = \det(\boldsymbol{\sigma}) \\
&= \sigma_{11}\sigma_{22}\sigma_{33} + 2\sigma_{12}\sigma_{23}\sigma_{31} - \sigma_{12}^2\sigma_{33} - \sigma_{23}^2\sigma_{11} - \sigma_{31}^2\sigma_{22} \\
&= \sigma_x\sigma_y\sigma_z + 2\tau_{xy}\tau_{yz}\tau_{zx} - \sigma_x\tau_{yz}^2 - \sigma_y\tau_{zx}^2 - \sigma_z\tau_{xy}^2
\end{aligned}
\tag{3.55}
$$

The von Mises maximum distortion energy criterion states that the maximum yield stress is reached when the material's distortion energy per volume surpasses its distortion energy when subjected to yielding in an uniaxial tension test (Hibbeler, 2000). For a general state of stresses, it is given by:

$$
\begin{aligned}
\sigma_{VM} &= \sqrt{I_1^2 - 3I_2} \\
&= \frac{1}{\sqrt{2}}\sqrt{\left(\sigma_x - \sigma_y\right)^2 + \left(\sigma_y - \sigma_z\right)^2 + \left(\sigma_x - \sigma_z\right)^2 + 6\left(\tau_{xy}^2 + \tau_{yz}^2 + \tau_{zx}^2\right)}
\end{aligned}
\tag{3.56}
$$

Based on principal stresses only, it can be reduced to:

$$
\sigma_{VM} = \frac{1}{\sqrt{2}}\sqrt{\left(\sigma_x - \sigma_y\right)^2 + \left(\sigma_y - \sigma_z\right)^2 + \left(\sigma_x - \sigma_z\right)^2} \tag{3.57}
$$

Matrix materials are in most cases isotropic, but have different tensile and compressive strengths. Matrix failure depends not only on the deviatoric stress invariant (von Mises) equivalent stress but also on the volumetric stress invariant (I_1) which, if considered mutually independent, could be written as (Ha et al., 2008):

$$\frac{\sigma_{VM}}{\sigma_{VM}^{cr}} = 1 \quad \text{or} \quad \frac{I_1}{I_1^{cr}} = 1 \tag{3.58}$$

A modified version of the von Mises criterion, as proposed by Bauwens (1970), was considered in this work for matrix damage onsetconsidering the influence of the hydrostatic stress on yielding of the material:

$$\frac{1}{2}\left(\frac{1}{C_m} + \frac{1}{T_m}\right)\sigma_{VM} + \frac{1}{2}\left(\frac{1}{T_m} - \frac{1}{C_m}\right)I_1 = 1 \tag{3.59}$$

A linear property degradation process is then started when the matrix failure condition is met, until the ultimate damage occurs.

3.3.4 Interface Failure Criterion

Similar to the interlaminar criteria proposed to simulate delamination, presented in section 3.2, an interface failure such as debonding or detachment between fiber and matrix can be caused by normal and tangential traction on the interface (Camanho and Davila, 2002).

$$\left(\frac{\langle t_n \rangle}{Y_n}\right)^2 + \left(\frac{t_t}{Y_t}\right)^2 + \left(\frac{t_x}{Y_x}\right)^2 = 1 \tag{3.60}$$

where angular brackets $\langle\rangle$ stand for the Macaulay brackets (returns argument if positive and zero otherwise), representing that no damage will occur under compression. t_n, t_t, and t_x and Y_n, Y_t, and Y_x, indicate interfacial tractions and maximum allowable values in normal, tangential (to the circumference), and longitudinal directions, respectively. Considering the overall effect of interfacial shear traction, its possible to rewrite as (Ha et al., 2008):

$$\left(\frac{\langle t_n \rangle}{Y_n}\right)^2 + \left(\frac{t_s}{Y_s}\right)^2 = 1 \tag{3.61}$$

in which t_s and Y_s represents interfacial shear traction and interfacial shear

strength, respectively. The material will undergo a linear property degradation process when the interface failure condition is met, until the ultimate damage occurs.

Chapter 4

Methodology

The scope of the present work is to develop a multiscale-based prediction of compression after impact (CAI) in composite materials. The CAI analysis is fundamental in the characterization of composite materials for applications such as airframe structures, conventionally demanding expensive experimental verification in order to obtain reliable results. In this work, a multiscale (Ha et al., 2008, 2010) based alternative design methodology is proposed, based on Octogonal Fiber Model (OFM) aproximation (Huang et al., 2020). A micro-structural material failure and degradation model is then proposed to provide a computationally efficient multiscale methodology to be applied in aircraft design. The proposed methodology aims to provide the ability to simulate material tests with various parameters, reducing the number of physically tested systems.

Pre-processing simulation tools were developed in Python, coded within the program development framework of the commercial finite element platform Abaqus® user environment as a plug-in tool to be accessed directly in the user-friendly Graphical User Interface environment (Dassault Systemes, 2014). This architecture allowed greater flexibility and simplicity in simulations based on impact and CAI standards (ASTM, 2014, 2012) standards. The idea here was to allow a simulation analysis of each respective mechanical test, also called virtual testing, with dimensions and boundary conditions based on the geometric parameters established by these standards.

The test specimens (Figure 4.1) as well as test method and apparatus, used as contour conditions, were developed based on ASTM (2012). First, an uni-axial Drop-Weight Impact test is imposed to a laminated plate.

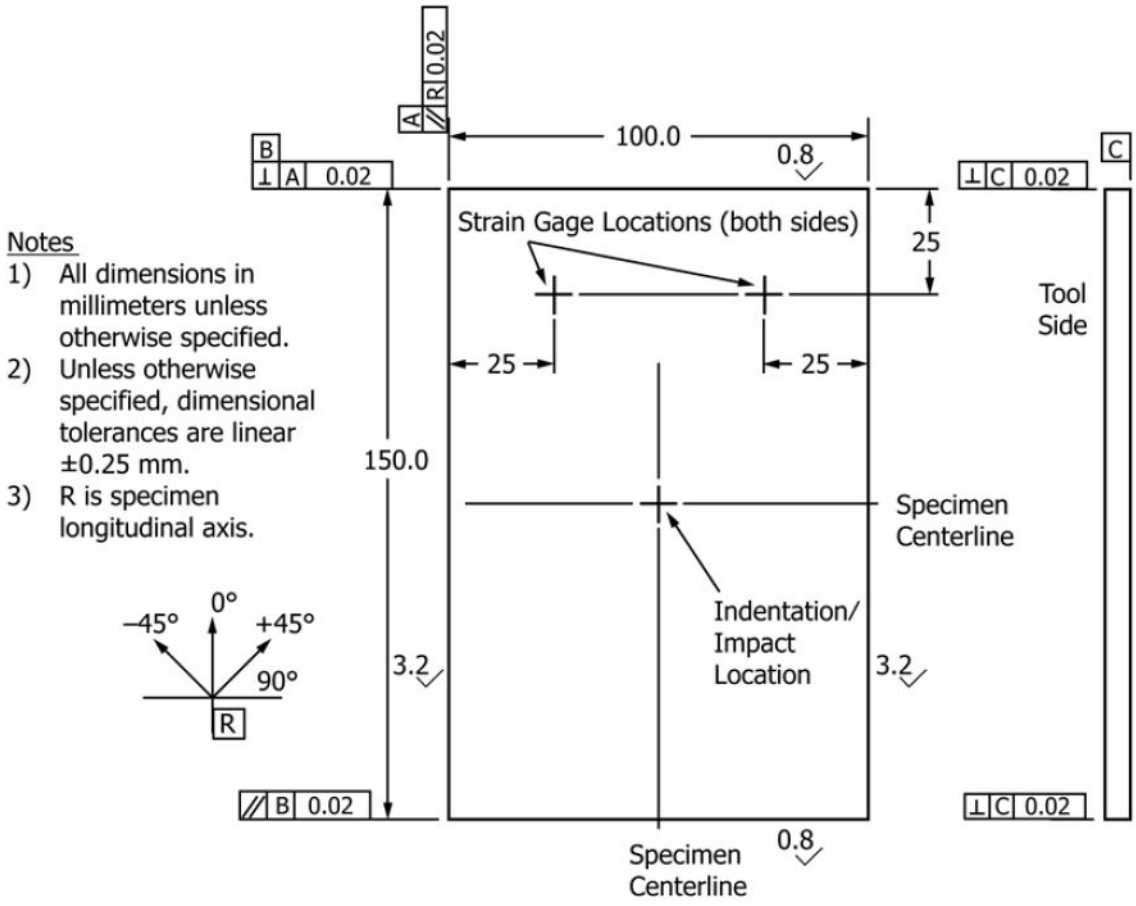

Figure 4.1: Compression residual strength test specimen (ASTM, 2012).

The damaged plate is then installed in a multi-piece support fixture (Figure 4.2), that has been aligned to minimize loading eccentricities and induced specimen bending. The specimen/fixture assembly is placed between flat platens and end-loaded under compressive force until failure. Applied force, crosshead displacement, and strain data are recorded while loading.

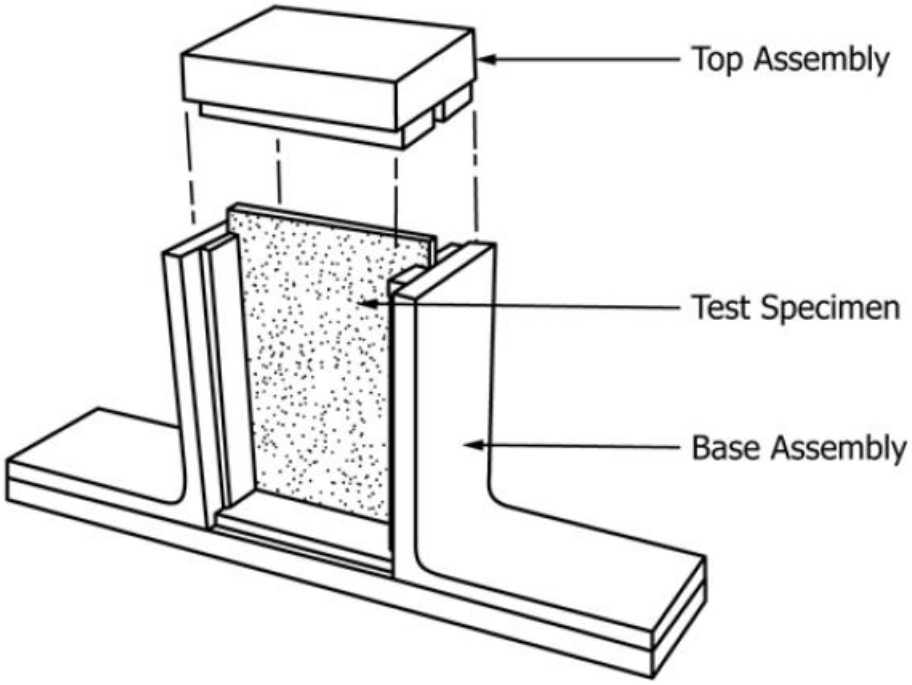

Figure 4.2: Schematic of compressive residual strength support fixture with specimen in place (ASTM, 2012).

As described in the test standard (ASTM, 2012), the acceptable failure modes obtained after the aforementioned tests (Figure 4.3) may be classified as preferred failure modes, which pass through the damage in the test specimen, and non-preferable acceptable failures, in wich case it initiates away from the damage site, in instances when the damage produces a relatively low stress concentration or if the extent of damage is small, or both. Unacceptable failure modes are those related to load introduction by the support fixture, local edge support conditions, and specimen instability (unless the specimen is dimensionally representative of a particular structural application) .

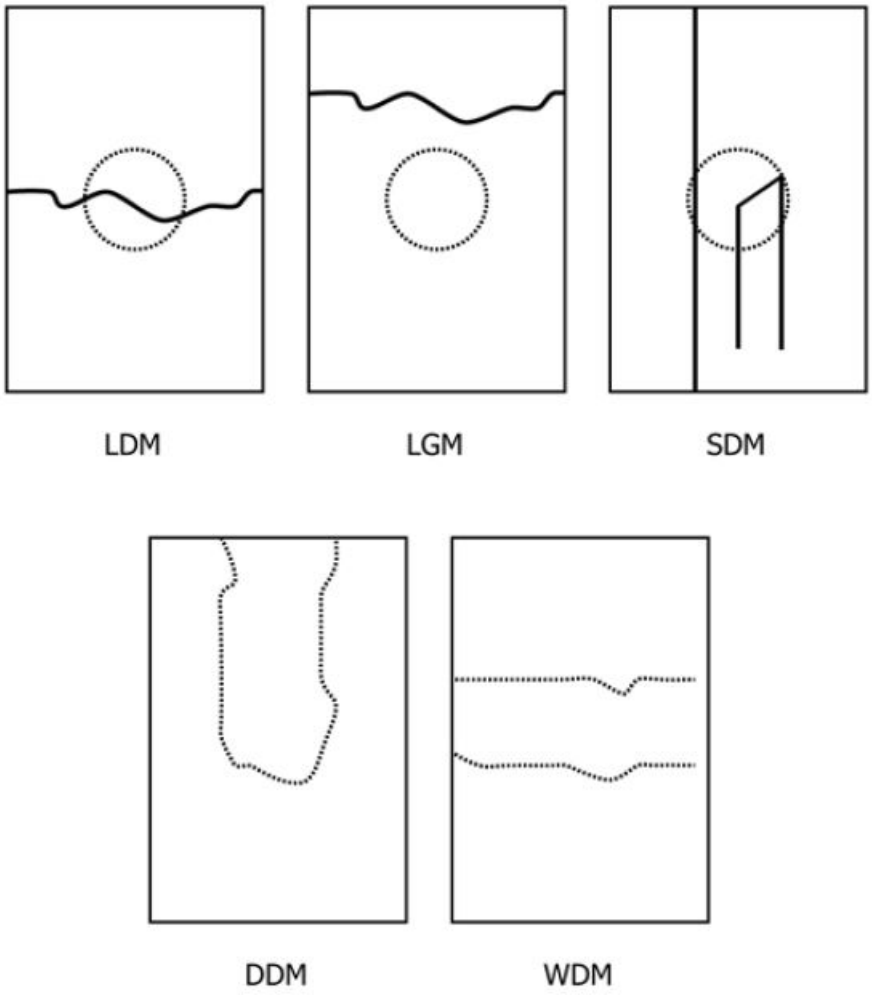

Figure 4.3: Commonly observed acceptable compressive residual strength failure modes (ASTM, 2012). In LDM, LGM, SDM DDM and WDM CAI failure descriptions: L stands for lateral failure; G for gauge/away from damage failure area; M is the middle location; D for at/through damage failure area; and W for transversal failure.

A semi-automatic measurement procedure tool was also developed aiming to achieve a fair judgement on the measurements when post-processing numerical and experimental graphical results. In this procedure, the damaged specimen raw image is first imported and converted to a grayscale array. Otsu's method (Otsu, 1979) is applied to calculate an optimal threshold and, using the obtained threshold as reference, the in-house semi-automatic tool tracks borderline polygons, filters the

obtained data, and calculate its area, and the maximum damage length for each studied case, reducing human factor in obtained measurements.

The proposed studies were developed focusing mainly in carbon test specimens, using available material data for both constituents and homogenized laminate (e.g.: Huang, Jin and Ha (2012), and Huang, Xu and Ha (2012)). Also, whenever possible, experimental data, previously obtained and/or available in the literature (e.g.: Ha et al. (2008), Hongkarnjanakul et al. (2013), Rivallant et al. (2013), and Tan et al. (2015*a*)), were used for the validation of the models, allowing to keep focus on the proposed numerical methodology development.

Due to the composite material characteristic in-homogeneity, non-uniform micro-stresses are presented at the constituent level (fiber, matrix, interface). Ply failures initiate and can have dissimilar failure mechanisms depending on where the critical points exist, demanding a failure criteria designed for each set, and capable to judge where failure initiates, demanding information about the correlation between macro (ply) stress/strain and micro stress/strain (Ha et al., 2008).

Multiscale approaches may be divided into two main classes (Metoui et al., 2018): the first, applied in this work due to its propensity to be more computationally efficient, considers a set of microscopic volumes, generally representative volume element (RVE), being generally based on an extension of the homogenization theory for non linear materials. This kind of methods requires to introduce some additional hypothesis to make the link between the microscale and the macroscale. The second class takes into account the microscale solution in each point of the macroscopic domain. In this case each fine-scale degree of freedom has to be treated at least one time in the algorithm. Therefore, these methods are generally more expensive than the methods belonging to the first class.

The use of unit cell RVE (Figure 4.4) model is capable to provide a laminate structural data, based in the material's fiber, matrix and interface structural properties, in a way that is not subject to the assumptions inherent in the analytical

approaches used in standard homogenization techniques. Additionally, a material local fields evolution behavior can be studied in the RVE model for a given far-field loading history. A far-field loading may be applied through periodic or symmetric boundary conditions (Huang, Jin and Ha, 2012; Heydari-Meybodi et al., 2016), and setting up the loads and analysis steps necessary to perform homogenization of properties or imposition of a far-field load history, being possible to define the homogenized properties of the RVE from the completed analysis as well as performing averaging and statistical analysis of the fields in the whole RVE and within individual RVE constituents (Kwon et al., 2007). The RVE size must be chosen sufficiently large relative to the microstructural size and small enough compared to the macroscopic body, containing adequate number of elements to have sufficient information about the microstructure and be a good representation of a continuum (Heydari-Meybodi et al., 2016). As shown by Dixit et al. (2013), a parametric study should be developed in order to explore the effectiveness of the model and to evaluate the influence of geometric and material parameters on the overall mechanical behavior.

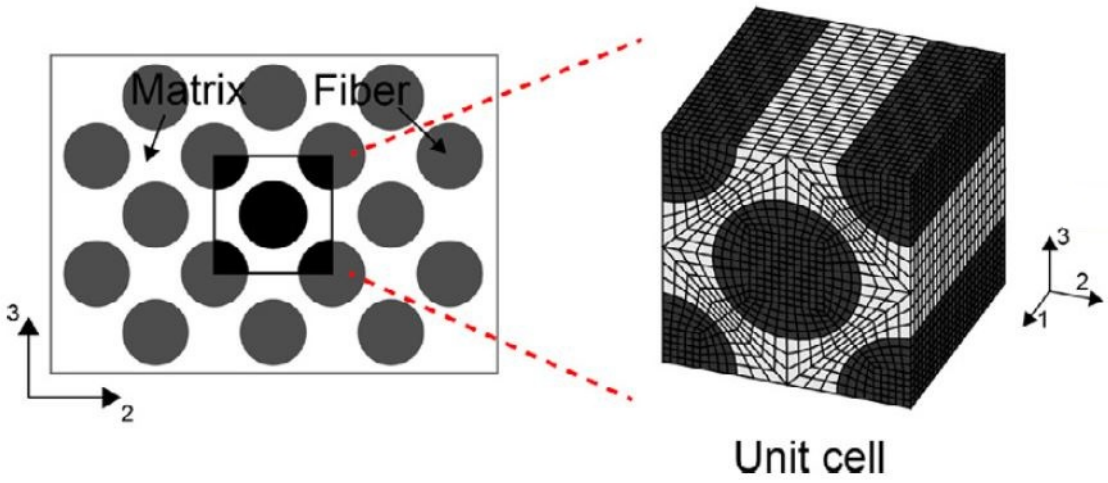

Figure 4.4: Unit cell RVE representation (Lou et al., 2017).

The microscale model approach was herein considered as a simplified composite materials periodic unit cell, based on Octogonal Fiber Model (OFM) aproximation (Huang et al., 2020). For materials that have this characteristic of structure repetition, a representative or effective response can be obtained from a single repeating cell through the application of periodic boundary conditions. The Representative Volume Element (RVE) microstresses and failure criteria were implemented by means of an user-defined material model, implemented in Fortran, as an Abaqus® user subroutine VUMAT (Dassault Systemes, 2014). As shown in Figure 4.5, considering the OFM model, the code is capable to convert macrostresses to microstresses for each OFM sub-region applying the Stress Amplification Factors (SAFs) presented in subsection 3.3.1. Considering the calculated microstresses, the subroutine is capable to verify micro-mechanical material failure for fiber, matrix and interface, separately. An area-based Damage Homogenization method is then proposed, as described in section 5.2, and the calculated damage is then included in the macroscale model as a degradation of the material's stiffness matrix.

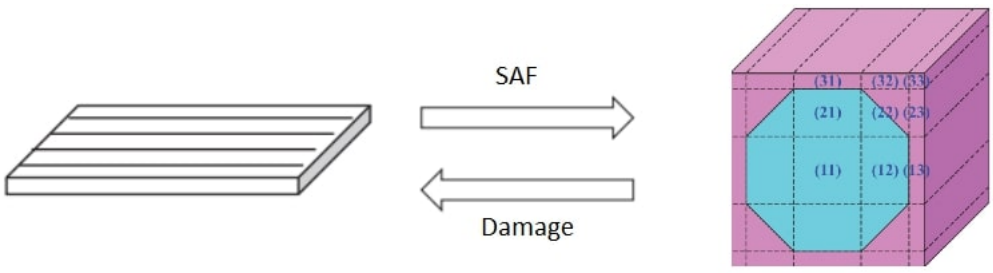

Figure 4.5: OFM-based micromechanics approach (addapted from Huang et al. (2020).

As a result, we intend to obtain a tool for developing a Compression After Impact (CAI) multi-scale virtual test in composite materials. Besides that, before its application in CAI models, it was verified considering simplified load-cases (chapter 6):

unidirectional tensile loads and simplified bidirectional loads. For both cases, literature available materials and reference results where considered, keeping the focus of this work mainly in the numerical model development.

A Mesh convergence was analyzed using damage area and residual stiffness measurements and, considering the converged mesh, the following five numerical cases are considered and compared to literature available experimental results:

In the first case (**Case 1**) the proposed model was analyzed considering continuum shell elements, using the Abaqus native form of the Hashin criterion (subsection 3.1.1) and the also native energy-based linear progressive damage model. Considering for **Case 2** the same intralaminar criterion as in Case 1, an inter-laminar cohesive failure criterion, described in section 3.2, was added at each lamina interface.

In the following cases, the use of the cohesive failure criterion is maintained. In these models, the use of three-dimensional elements is proposed instead of continuum shell elements. Considering that in **Case 3**, the intralaminar failure were verified considering the subroutine *uniFiber.f*, which is available in Abaqus® documentation (Dassault Systemes, 2014; Nie, 2014). In this VUMAT it is possible to observe the use of the Hashin criterion (Hashin, 1980) for fiber direction, and the Puck's plane of action theory Puck and Schurmann (1998) is considered for tension and compression for failure perpendicular to the fiber, as described in subsection 3.1.2.

In **Case 4**, the modified VUMAT proposed in the thesis is considered. In this modification it is proposed to consider Hashin criterion (Hashin, 1980) for both fiber ans matrix directions. The Hashin criterion in its conventional form is proposed for the plane stress state. In order not to completely disregard the out-of-plane stresses from the three-dimensional elements, it was proposed here to consider the equations presented in Hashin's original article just before the plane stress simplifications. The subroutine, like the original one, did not include progressive damage (binary failure) and the cohesive failure criterion was kept in the model.

Finally, **Case 5** considers the VUMAT proposed in this work, presented in section 5.2, which contains the multiscale criterion based on the Octagonal Fiber Model subsection 3.3.1. In summary, the macroscale model feeds the VUMAT with material data and macro-scale stresses. Using the stress amplification factors (SAFs) calculated for the OFM (Huang et al., 2020), macro-stresses are converted into micro-stresses for fiber, matrix and interface in each of the OFM's quadrants. These approximated micro-scale stresses are then analyzed separately: For fibers, the verification is performed by a criterion of maximum longitudinal tension. This criterion is a simplification of the Tsai-Wu criterion (subsection 3.3.2) when considering that the fiber has a high module compared to the matrix. Next, a damage homogenization criterion is proposed based on each of the 9 fiber's sub-regions. Similarly, the Bauwens criterion (subsection 3.3.3) is considered to verify each of the 20 regions of the matrix. Again, a damage homogenization criterion is proposed based on the proportion of the matrix damaged area. Finally, the stresses at the interface are verified considering the cohesive failure criterion (subsection 3.3.4), and a damage homogeneization was proposed considering the eight equal sides of the octagon. The calculated homogenized damage is then used to feed back the macroscale model as a degradation of the material's stiffness matrix.

Applying the parametric modeling tool developed in this work (section 5.1), impact and CAI models are automatically generated based on material and laminate data. The Impact model is processed and its laminate damage results are used as input to the post impact compression model. It is also performed, applying the tool proposed in this work (section 5.3), the impact damaged area measurement is performed considering an inter-laminar and intralaminar damage envelope. Again literature available materials and reference results where considered and compared to each of the 5 described cases, keeping the focus of this work mainly in the numerical model development.

Chapter 5

Virtual Testing Modeling, Processing, and Post Processing Strategies

This chapter presents a description of the computational tools proposed and developed during this work focusing in perform composite materials multiscale-based prediction of Compression After Impact (CAI). First, a semiautomatic user-friendly Abaqus® Graphic User Interface (GUI) is presented in section 5.1, capable to automatically build Impact and CAI models and to be used with different user developed subroutines (VUMAT). section 5.2 presents a cost effective Abaqus® user subroutine (VUMAT), developed based in Octagonal Fiber Model (Huang et al., 2020) and micromechanics analysis-based criteria. section 5.3 presents a semi-automatic damage area measurement procedure for impact test results, which may be applied to experimental and numerical tests, developed focusing in human factor reduction in impact damaged area measurements.

5.1 Compression After Impact (CAI) Virtual Test Parametric Modeling Tool

A Compression After Impact (CAI) Virtual Test Parametric Modeling Tool was coded within the program development framework of the commercial finite element platform Abaqus®. The developed layup modeling automation may be applied for

many other composite simulation problems. Besides not being the main focus of this work, the presented Virtual Test Parametric Modeling Tool was already modified by the author of these studies to simulate others problems of interest for damage tolerance in composite aeronautical structures, specifically developing tools for Open hole laminates subjected to traction and compression, and for Adhesive and Pinned Single-lap joints.

The idea here was to allow a simulation analysis of each respective mechanical test, also called virtual testing. The proposed architecture allowed greater flexibility and simplicity in using the tool, being capable to automatic process different layups based in a free tabular description consisting in one line representing each new ply. The automation process was designed to also allow the use of different materials and criteria, focusing on avoiding limitations due to the specificities of this work, being a tool to study damage tolerance and residual compression strength after impact in composite aeronautical components. CAI test is one of the most important material characterization tests to be used in structural components, consuming time and resources. Therefore, a computational tool was developed to virtually analyze this problem, which is composed of two parts: the impact test and the subsequent compression test (Figure 5.1).

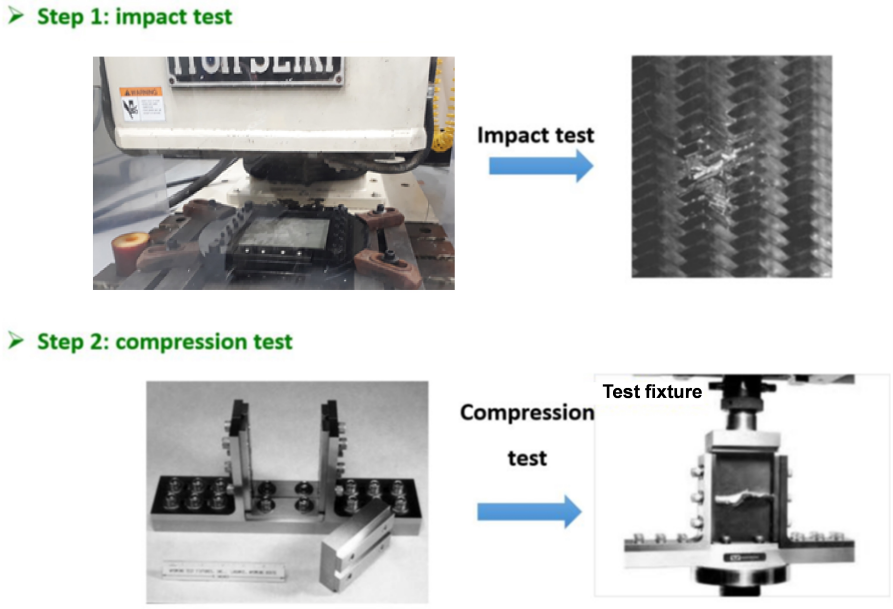

Figure 5.1: Compression After Impact (CAI) test (based from Professor Sung Ha (Hanyang University) and Professor Carlos Cimini (UFMG)).

The developed tool was based on ASTM D7136 (ASTM, 2014) and ASTM D7137 (ASTM, 2012) standards, which respectively deal with the impact on specimen and evaluation of its residual compressive strength with focus in bending-impact effects. The tool may also be applied to different standards, as AIT (2010) which was considered in chapter 7, with direct model modifications. The tool may also be customized to automatic generate a final model respecting a different standard. It is important to observe that the choice of boundary conditions can have a significant impact on the results of composite material impact tests. Clamped or simple supported boundary conditions tend to produce bending-impact effects as a greater deformation is observed in results. Fixed boundary conditions, on the other hand, tend to produce produce higher stresses and strains in the material, as the material is completely constrained and cannot deform freely. Also, besides different studies commonly performs tests with different energy levels, a standard calculation is

commonly proposed. As an example, ASTM (2014) proposes an impact energy calculated as function of the nominal thickness of the specimen (mm), considering a specified ratio of impact energy to specimen thickness of 6.7 J/mm.

The three-dimensional model for the compression after impact problem was developed with the option of using either a perfect union or a cohesive surface between plies. Each ply composed of eight-node C3D8R three-dimensional elements from the Abaqus® element library, resulting in a regular mesh for modeling the problem. The elements assume a small dimension in the thickness direction when compared to the other dimensions. However, the mesh presents no ill-conditioning, which needs to be checked during the analyses. The meshes and boundary conditions can be seen in Figure 5.2. Although the CAI test is essentially quasi-static, it proposed to be simulated using ABAQUS®/Explicit to avoid the severe convergence difficulties encountered with implicit analysis when modeling highly non-linear behavior (Tan et al., 2015*a*). Optionally is also possible to consider the plate stiffened by T-stiffeners.

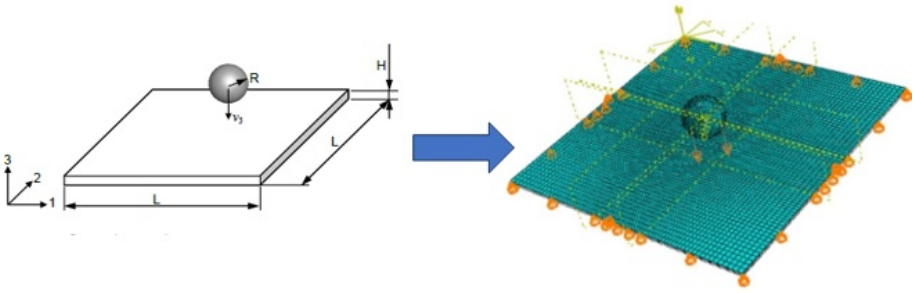

Figure 5.2: Finite element model example for impact (CAI).

Developed in Python into Abaqus® user environment, the tool is composed of seven tabs, each one presenting self-explanatory input choices to control model parameters and input data. The first (Figure 5.3) asks for basic model, as work directory ans reference name, laminate sizes, mechanical properties, layup sequence,

interface data, and Abaqus® VUMAT user subroutine to be used in simulations, allowing to apply a Fortran based user-defined material model and failure criteria.

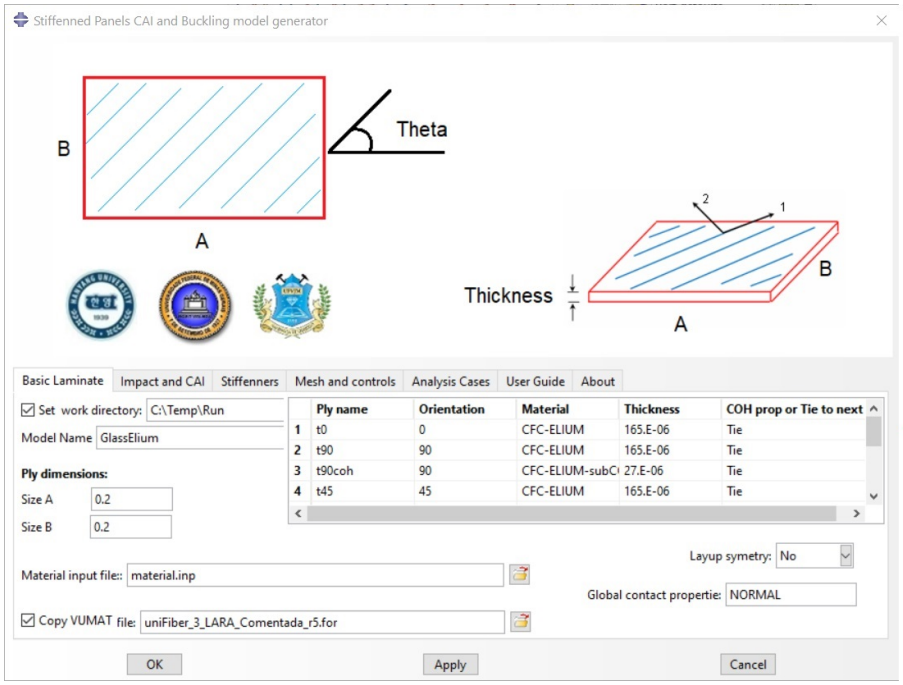

Figure 5.3: Tab for entering basic laminate data.

The second tab (Figure 5.4) defines impact and post-impact compression analysis initial data and output requests.

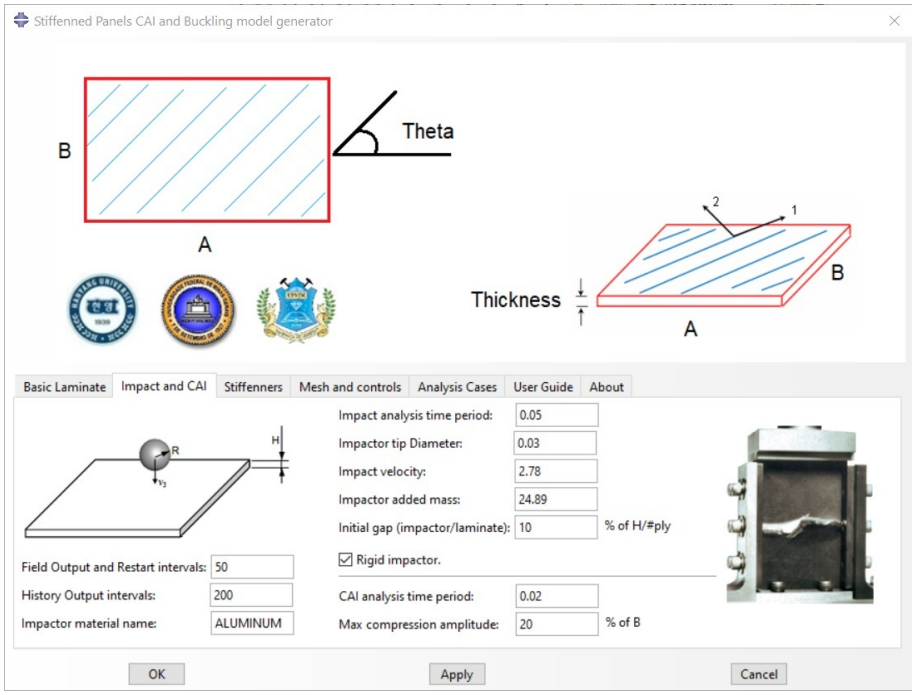

Figure 5.4: Tab to define the analysis phases of impact and compression after impact..

The third tab (Figure 5.5) may be used to insert optional data for including (or not) the T-stiffeners in the borders and/or middle plate positions. Also, if inserted, T-stiffeners dimensions, material, layup and mesh data are needed.

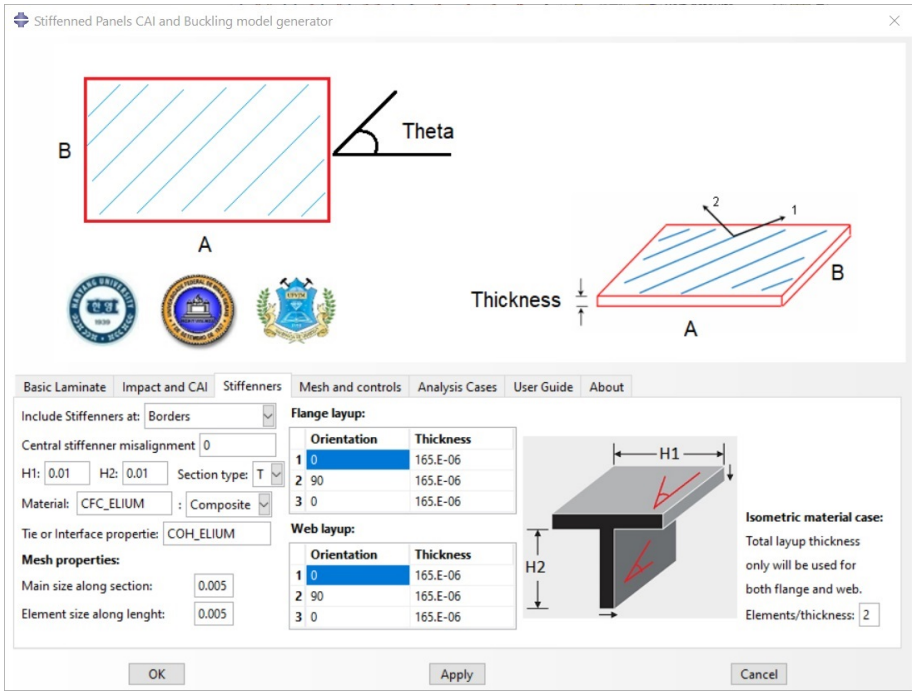

Figure 5.5: Tab to include (or not) T-stringers in the plate..

Tab number four (Figure 5.6) controls the mesh data and the analysis control parameters (Mesh and controls).

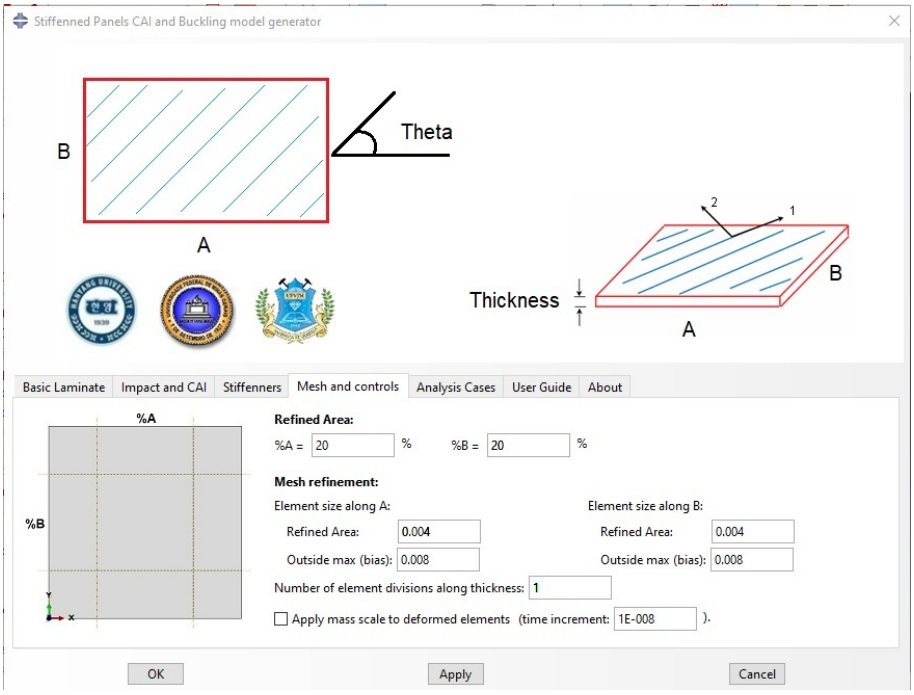

Figure 5.6: Tab for entering parameters for the mesh and analysis control.

The fifth tab (Figure 5.7) is used to select which analysis cases models and jobs should be created:

- None: creates laminate only;
- Impact: creates Impact case based on laminate, impactor, and stiffners (if included) input data;
- CAI: creates Compression After Impact analysis based on Impact results (Impact results needed to run this case);
- Undamaged compression: creates Compression case based on laminate and stiffners (if included) input data;
- Buckling: creates Buckling case based on laminate and stiffners (if included) input data;

- Post Buckling Compression: creates Post Buckling Compression analysis based on Buckling results (Buckling results needed to run this case).

Notice that the tool is also capable to create undamaged and buckling analysis models, and that some of the cases, as described, depends on the previous case to import initial data.

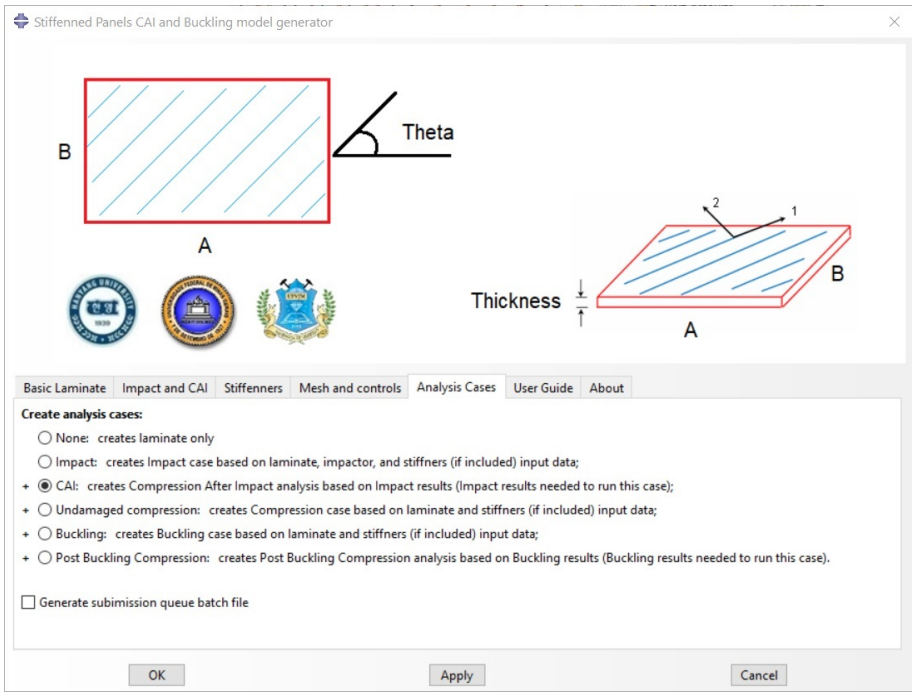

Figure 5.7: Tab for data entry of the analysis cases.

The last two tabs, shown in Figure 5.8 and Figure 5.9, are reference to the User Manual and identification data of the coded version, respectively.

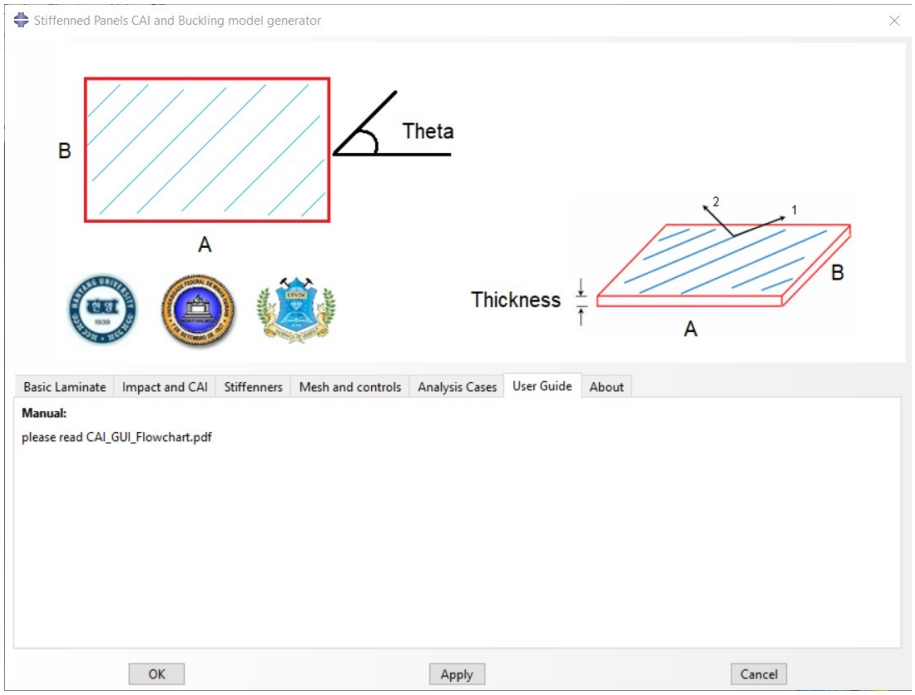

Figure 5.8: Tab with reference to the User's Manual.

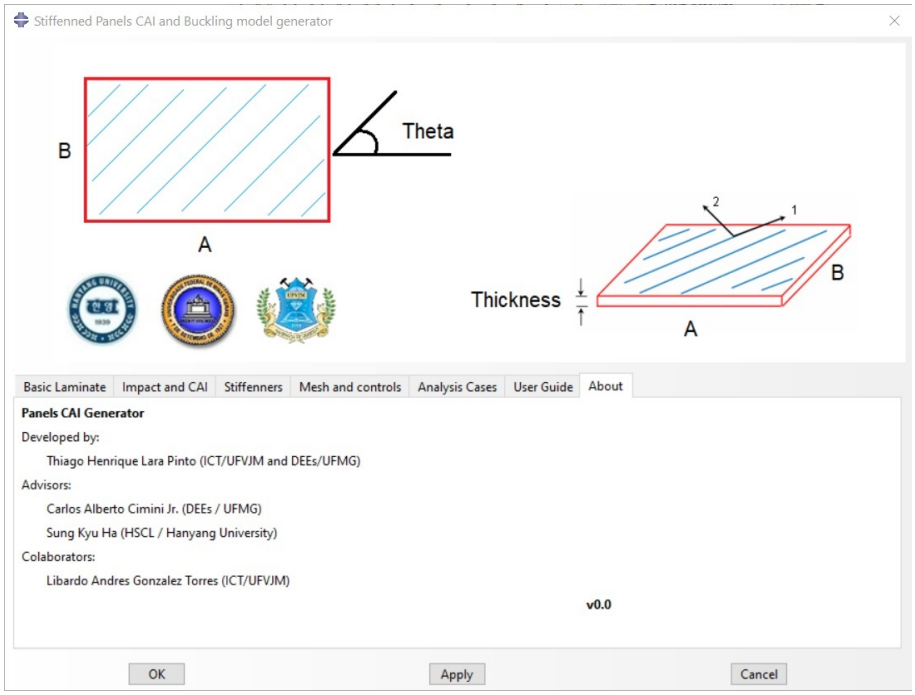

Figure 5.9: Tab with identification of the encoded version.

The flowchart in Figure 5.10 presents the main steps implemented in Compression After Impact (CAI) Virtual Test tool. The Graphic User Interface (GUI) described above is used to insert input data. The tool will then create each of the laminas and the impactor, as described the input, in separate parts, including and positioning them in a single assembly. Next, boundary conditions and tie constraints between each ply are inserted. A global interaction is created and, based on input laminate data, unnecessary tie constraints are replaced by cohesive contact surfaces. Optionally, the tool is capable to create T-stiffeners reinforcements to the layup. At this point, an Impact case Abaqus® job is created, then a copy of the full model is created, renamed, where boundary conditions are modified to CAI case and the Impact job result is set as initial condition, creating then a CAI case Abaqus® job. As extra features, this tool is also capable to modify the models and create undamaged compression case, where no impact is taken into account before compression case, Buckling analysis case, and Post-bukling compression, importing buckling results as initial condition for compression case.

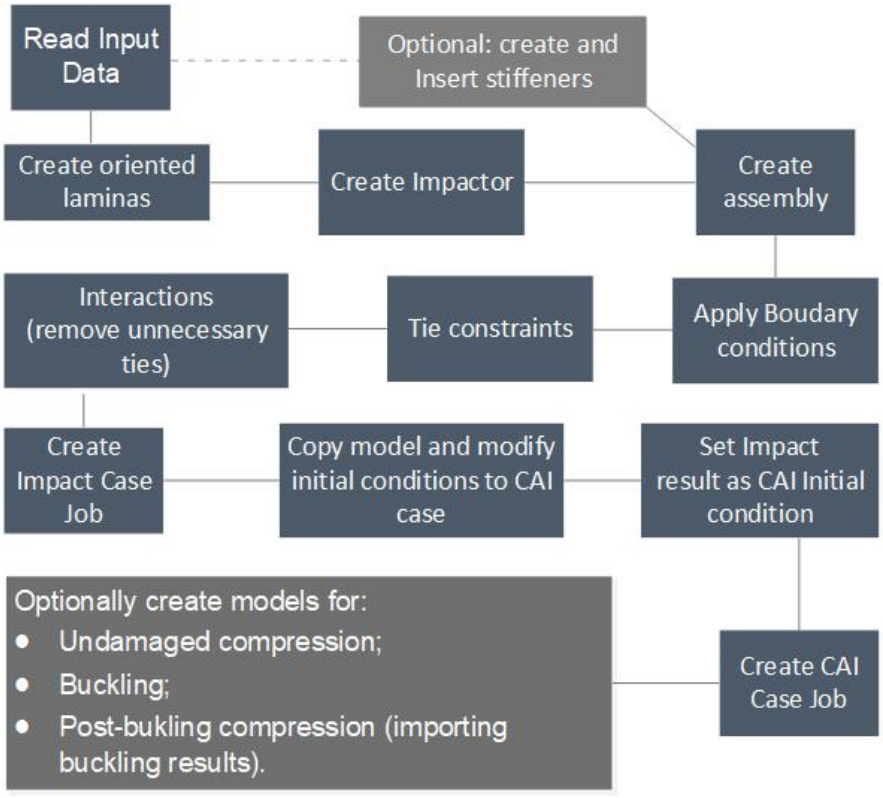

Figure 5.10: Compression After Impact (CAI) Virtual Test code flowchart.

Figure 5.11 shows typical result for CAI virtual testing analysis obtained in the Abaqus® environment using the presented tool.

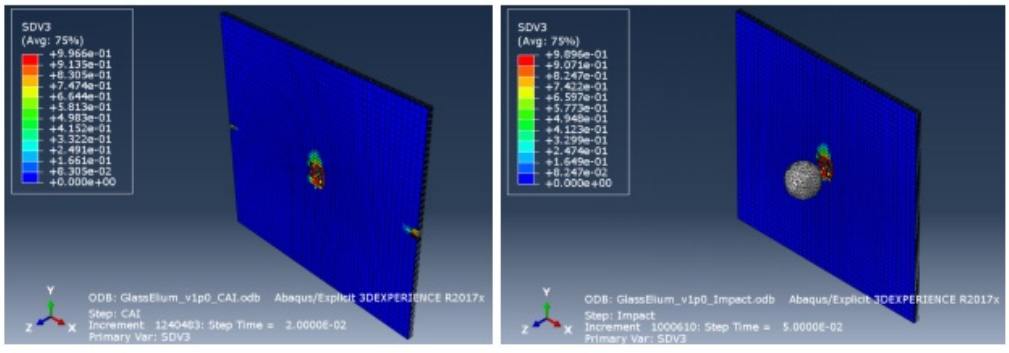

Figure 5.11: Typical failure index using Hashin criterion (CAI).

5.2 Octagonal Fiber Model Based Micromechanics Analysis and Failure Criteria

The proposed multiscale analysis was developed based on the Octagonal Fiber Model (Huang et al., 2020) and micromechanical failure criteria for fiber, matrix and interface, separately. The proposed model, summarized in Figure 5.12, was developed focusing in a cost effective Compression After Impact (CAI) virtual testing multiscale-based prediction. Following a similar structure to the one proposed in Nie (2014), the code first reads the material input data from the current macroscale model.

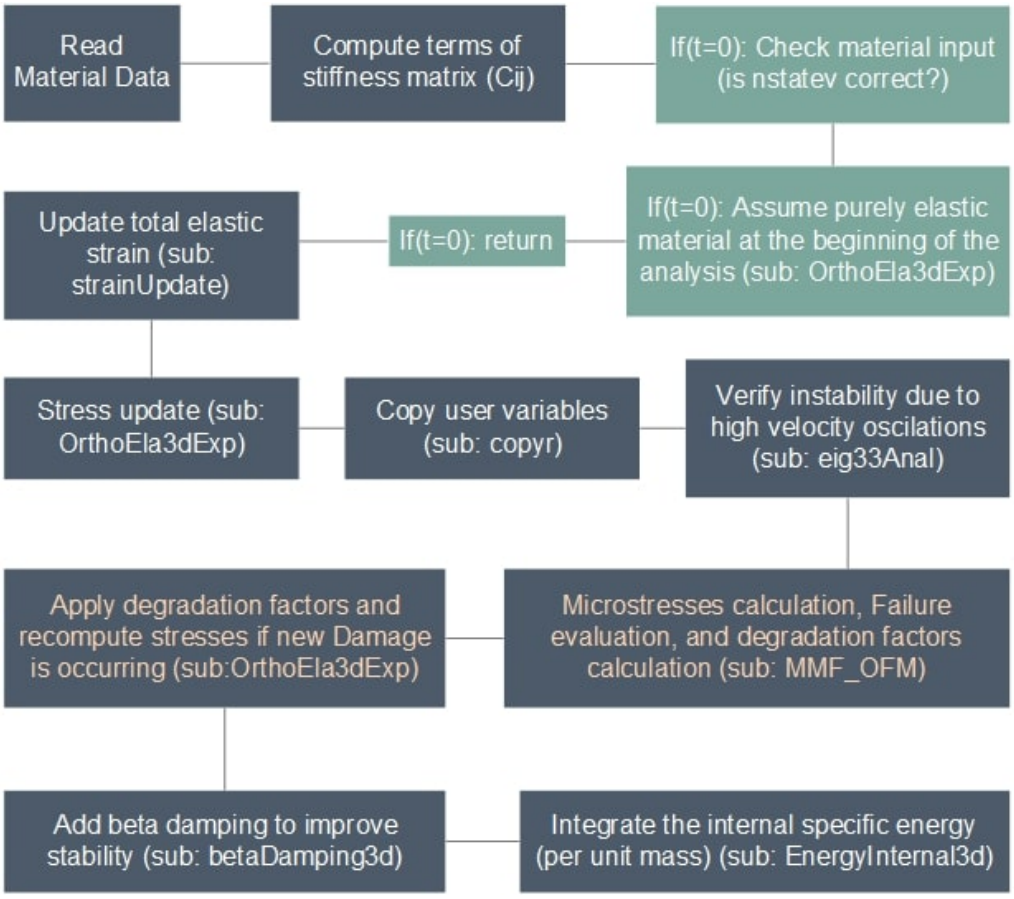

Figure 5.12: Micromechanics model flowchart.

Based on information read from the macroscale model, the proposed multi-scale model calculates the undamaged elastic constants (C_{ij}^{0}), based in material engineering constants (E_{ij}, G_{ij} and v_{ij}), as presented in Equation 5.1.

$$\begin{aligned}
C_{11}^{0} &= E_{11}\left(1 - v_{23}v_{32}\right)\Gamma \\
C_{22}^{0} &= E_{22}\left(1 - v_{13}v_{31}\right)\Gamma \\
C_{33}^{0} &= E_{33}\left(1 - v_{12}v_{21}\right)\Gamma \\
C_{12}^{0} &= E_{11}\left(v_{21} + v_{31}v_{23}\right)\Gamma \\
C_{23}^{0} &= E_{22}\left(v_{32} + v_{12}v_{31}\right)\Gamma \\
C_{13}^{0} &= E_{11}\left(v_{31} + v_{21}v_{32}\right)\Gamma \\
\Gamma &= 1/\left(1 - v_{12}v_{21} - v_{23}v_{32} - v_{31}v_{13} - 2v_{21}v_{32}v_{13}\right)
\end{aligned} \tag{5.1}$$

The code then verifies the step time and, if it finds itself in the beginning of the analysis (time equals to zero), it performs an input check, using the correct number of state variables as verification, assumes purely elastic material at the beginning of the analysis to perform a stress/strain relationship (Equation 5.2), and returns to the analysis.

$$\begin{pmatrix} \sigma_{11} \\ \sigma_{22} \\ \sigma_{33} \\ \sigma_{12} \\ \sigma_{23} \\ \sigma_{31} \end{pmatrix} = \begin{pmatrix} C_{11} & C_{12} & C_{13} & 0 & 0 & 0 \\ C_{12} & C_{22} & C_{23} & 0 & 0 & 0 \\ C_{13} & C_{23} & C_{33} & 0 & 0 & 0 \\ 0 & 0 & 0 & 2G_{12} & 0 & 0 \\ 0 & 0 & 0 & 0 & 2G_{23} & 0 \\ 0 & 0 & 0 & 0 & 0 & 2G_{31} \end{pmatrix} \begin{pmatrix} \varepsilon_{11} \\ \varepsilon_{22} \\ \varepsilon_{33} \\ \varepsilon_{12} \\ \varepsilon_{23} \\ \varepsilon_{31} \end{pmatrix} \tag{5.2}$$

For the following time steps, total elastic strain is calculated adding the incremental elastic strain, from the current step, to the elastic strain obtained in the last step. The elements of the stiffness matrix are calculated based on material input data, and used to calculate stresses, in a similar way to the described above for time equals to zero. A copy of each of the user variables is then created and eigenvalues are calculated in orther to verify model stability due to high velocity oscillations.

Based on the macro-mechanical model current condition, the micro-mechanical stresses were them calculated considering a micro-mechanical unit cell, implemented considering the Octagonal Fiber Model (OFM) theory presented in subsection 3.3.1 (Figure 5.13).

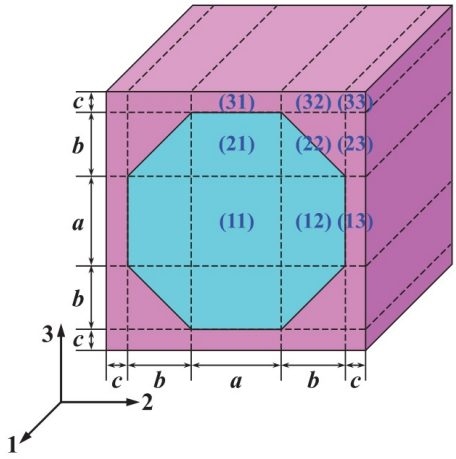

Figure 5.13: Geometry of the OFM. (Huang et al., 2020).

Evaluating the fiber volume fraction from the input material, and an unitary Representative Volume Element (RVE) based in the Octagonal Fiber Model (OFM), it is possible to write the following equations:

$$\begin{aligned} a + 2b + 2c &= 1 \\ V_f &= a^2 + 4ab + 2b^2 \end{aligned} \tag{5.3}$$

Also, considering that the octagonal geometry has eight equal dimension sides of lenght a, and considering the sub-region $ij = 22$, it is possible to conclude, by the application of the Pythagorean theorem, that:

$$a^2 = b^2 + b^2 \tag{5.4}$$

Solving the system composed of the three equations above, we can obtain the

dimensions a, b and c as a function of the fiber volume fraction from the input material. Since a unitary Representative Volume Element (RVE) is herein considered, the obtained values are dimensionless, being fractions of the total length.

$$\begin{cases} a = \sqrt{2b^2} \\ b = \frac{\sqrt{\sqrt{2}V_f - V_f}}{2} \\ c = \frac{1-\sqrt{2b^2}-2b}{2} \end{cases} \tag{5.5}$$

The fiber cross section area at each sub-region, and the total fiber cross section area, may be calculated as:

$$\begin{aligned} A^f_{11} &= a \times a \\ A^f_{12} &= A^f_{21} = a \times b \\ A^f_{22} &= b \times b/2 \\ A^f_{Total} &= A^f_{11} + 2 \times A^f_{12} + 2 \times A^f_{21} + 4 \times A^f_{22} \\ &= a^2 + 4ab + 2b^2 \end{aligned} \tag{5.6}$$

Similarly, the matrix cross section area at each sub-region, and the total matrix cross section area, may be calculated as:

$$\begin{aligned} A^m_{22} &= b \times b/2 \\ A^m_{13} &= A^m_{31} = a \times c \\ A^m_{23} &= A^m_{32} = b \times c \\ A^m_{33} &= c \times c \\ A^m_{Total} &= 4 \times A^m_{22} + 2 \times A^m_{13} + 4 \times A^m_{23} + 4 \times A^m_{33} + 2 \times A^m_{31} + 4 \times A^m_{32} \\ &= 2b^2 + 4ac + 8bc + 4c^2 \end{aligned} \tag{5.7}$$

As described in subsection 3.3.1, Stress Amplification Factor (SAFs) are then calculated and used to correlate ply stresses, at macro-scale level, and micro-stresses in fiber and matrix constituents, at micro-scale level (Jin et al., 2008; Huang et al., 2020), as shown in Figure 5.14.

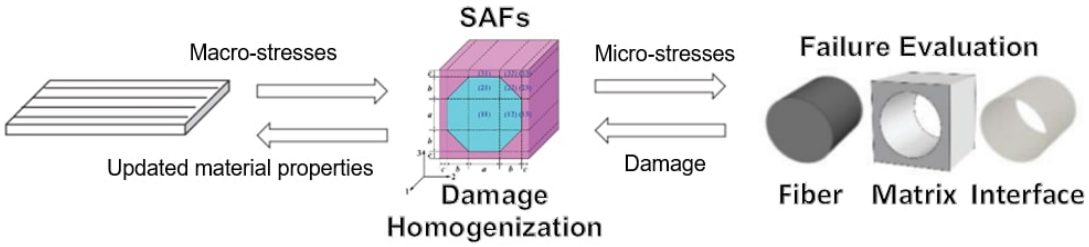

Figure 5.14: Octagonal Fiber Model based multiscale approach (Adapted from Huang et al. (2020)).

This relationship can be expressed by analytically at a certain material point inside a constituent, being Stress Amplification Factors (SAF) expressed as M_{ij}, while σ and $\bar{\sigma}$ represent ply stresses and micro-stresses at the same material point, respectively.

$$\left(\sigma_i \right) = \left[M_{ij} \right]_{\mathbf{c}} \left(\bar{\sigma}_j \right) \tag{5.8}$$

At the fiber-matrix interface, the micro-stresses (t_i) can be also obtained using a similar correlation, considering macro-stresses and SAFs.

$$\left(t_i \right) = \left[M_{ij} \right]_{\mathrm{i}} \left(\bar{\sigma}_j \right) \tag{5.9}$$

Considering longitudinal micro-stresses at fiber, the maximum longitudinal stress failure criterion Ha et al. (2008) is applied for each sub-region, as described in subsection 3.3.2

$$-X'_f < \sigma_x^f < X_f \tag{5.10}$$

Considering this criteria for each sub-region, a damage homogenization was proposed based on the damaged fiber area fraction at tension (A^f_{damT}) or compression (A^f_{damC}), with variable range from zero to one. Notice that, even though only nine

sub-regions are independent, all 25 sub-regions are considered for the proposed homogenization criteria.

$$
\begin{aligned}
A^f_{damT} &= \sum_{sub\text{-}regions=1}^{25} \frac{A^f_{ij}}{A^f_{Total}} \\
&\quad considering \quad A^f_{ij} = \begin{cases} A^f_{ij}, & \text{if } \sigma^f_x > X_f \\ 0, & \text{otherwise} \end{cases} \\
A^f_{damC} &= \sum_{sub\text{-}regions=1}^{25} \frac{A^f_{ij}}{A^f_{Total}} \\
&\quad considering \quad A^f_{ij} = \begin{cases} A^f_{ij}, & \text{if } \sigma^f_x < -X'_f \\ 0, & \text{otherwise} \end{cases}
\end{aligned}
\tag{5.11}
$$

Bauwens' criteria (Ha et al., 2008; Bauwens, 1970) is then applied considering matrix microstresses, also for each sub-region separately, as described in subsection 3.3.3

$$
C_{Bauwens} = \frac{1}{2}\left(\frac{1}{C_m} + \frac{1}{T_m}\right)\sigma_{VM} + \frac{1}{2}\left(\frac{1}{T_m} - \frac{1}{C_m}\right) I_1 \tag{5.12}
$$

A similar damaged area fraction (A^m_{dam}) homogenization was proposed based on the damaged matrix area fraction considering Bauwens' criteria ($C_{Bauwens}$).

$$
\begin{aligned}
A^m_{dam} &= \sum_{sub\text{-}regions=1}^{25} \frac{A^m_{ij}}{A^m_{Total}} \\
C^m_{Mean} &= \sum_{sub\text{-}regions=1}^{25} C_{Bauwens} \times \frac{A^m_{ij}}{A^m_{Total}} \\
&\quad considering \quad A^m_{ij} = \begin{cases} A^m_{ij}, & \text{if } C_{Bauwens} > 1 \\ 0, & \text{otherwise} \end{cases}
\end{aligned}
\tag{5.13}
$$

And, considering the calculated interfacial microstresses, interface failure criteria (Ha et al., 2008; Camanho and Davila, 2002) is applied for each subregion, as described in subsection 3.3.4

$$C_{Interface} = \left(\frac{\langle t_n \rangle}{Y_n}\right)^2 + \left(\frac{t_s}{Y_s}\right)^2 \tag{5.14}$$

For interface failure criteria ($C_{Interface}$), a damaged length fraction (L^i_{dam}) homogenization was proposed based on the eight equal sides of the fiber's octagonal model, again with variable range from zero to one.

$$\begin{aligned} L^i_{dam} &= \sum_{sub\text{-}regions=1}^{25} \frac{len}{8} \\ C^i_{mean} &= \sum_{sub\text{-}regions=1}^{25} C_{Interface} \times \frac{len}{8} \\ where \quad len &= \begin{cases} 1, & \text{if} \quad i+j=4 \quad and \quad C_{Interface} > 1 \\ 0, & \text{otherwise} \end{cases} \end{aligned} \tag{5.15}$$

A mean tension homogenization procedure was proposed, also based in fiber and matrix areas, considering longitudinal stress for fibers (σ^f_x) and the all six matrix stress and shear (σ^m_{dir} and τ^m_{dir}).

$$\begin{aligned} \left(\sigma^f_x\right)_{\text{homog}} &= \sum_{sub\text{-}regions=1}^{25} \left[\left(\sigma^f_x\right)_{ij}\right] \frac{A^f_{ij}}{A^f_{Total}} \\ \left(\sigma^m_{dir}\right)_{\text{homog}} &= \sum_{sub\text{-}regions=1}^{25} \left[\left(\sigma^m_{dir}\right)_{ij}\right] \frac{A^m_{ij}}{A^m_{Total}} \\ \left(\tau^m_{dir}\right)_{\text{homog}} &= \sum_{sub\text{-}regions=1}^{25} \left[\left(\tau^m_{dir}\right)_{ij}\right] \frac{A^m_{ij}}{A^m_{Total}} \\ & \qquad dir = x, y, z \end{aligned} \tag{5.16}$$

A normal (t_n) and shear (t_s) interface stress homogenization procedure was also proposed, based in the eight equal length interface sections.

$$\begin{aligned} \left(t_{dir}\right)_{\text{homog}} &= \sum_{section=1}^{8} \left[\frac{\left(t_{dir}\right)_{ij}}{8}\right] \\ & \qquad dir = n, s \end{aligned} \tag{5.17}$$

Following, as described in Figure 5.12, a section-based homogenization method is proposed for OFM micro-mechanical model approximation. No material property

degradation model is applied for fiber case, since considering a brittle behavior for fiber breakage under longitudinal tension or compression (no buckling), so a binary damage index (d_f) is considered for fiber case. In case of fiber traction failure, the element is directly removed from the model, otherwise, a linear property degradation process is started when the matrix (d_m) or interface (d_i) failure condition is met, with values varying linearly from zero at damage onset, to one when the ultimate damage occurs. As shown in Figure 5.14, the proposed damage homogenization is then considered to update the main model material properties. The damaged elastic constants in the material stiffness matrix (Equation 5.2) were recomputed in terms of the initial elastic constants C_{ij}^0 (Equation 5.1).

$$
\begin{aligned}
C_{11} &= (1 - d_f)\, C_{11}^0 \\
C_{22} &= (1 - d_f)\,(1 - d_{mi})\, C_{22}^0 \\
C_{33} &= (1 - d_f)\,(1 - d_{mi})\, C_{33}^0 \\
C_{12} &= (1 - d_f)\,(1 - d_{mi})\, C_{12}^0 \\
C_{23} &= (1 - d_f)\,(1 - d_{mi})\, C_{23}^0 \\
C_{13} &= (1 - d_f)\,(1 - d_{mi})\, C_{13}^0 \\
G_{12} &= (1 - d_f)\,(1 - S_{mtc} d_{mi})\, G_{12}^0 \\
G_{23} &= (1 - d_f)\,(1 - S_{mtc} d_{mi})\, G_{23}^0 \\
G_{31} &= (1 - d_f)\,(1 - S_{mtc} d_{mi})\, G_{31}^0 \\
d_f &= 1 - (1 - d_{ft})\,(1 - d_{fc}) \\
d_{mi} &= 1 - (1 - d_m)\,(1 - d_i)
\end{aligned}
\tag{5.18}
$$

The factors s_{mtc} in the definitions of the shear module were introduced to control the loss of shear stiffness caused by matrix tensile and compressive failure. The factor value was assumed empirically as 0.9 and 0.5 for traction and compression cases, respectively Nie (2014). The global fiber (d_f), and matrix and interface (d_{mi}) damage variables are computed from fiber tension and compression (d_{ft} and d_{fc}),

matrix (d_m) and interface (d_i) failure indexes, respectively, calculated as described in Equation 5.19.

$$
\begin{aligned}
d_{ft} &= \begin{cases} 1, & \text{if} \quad A^f_{damT} > 1 \\ 0, & \text{otherwise} \end{cases} \\
d_{fc} &= \begin{cases} 1, & \text{if} \quad A^f_{damC} > 1 \\ 0, & \text{otherwise} \end{cases} \\
d_m &= \begin{cases} 0, & \text{if} \quad A^m_{dam} < 1 \\ C^m_{Mean} - 1, & \text{if} \quad A^m_{dam} > 1 \quad and \quad C^m_{Mean} < 2 \\ 1, & \text{if} \quad A^m_{dam} > 1 \quad and \quad C^m_{Mean} > 2 \end{cases} \\
d_i &= \begin{cases} 0, & \text{if} \quad L^i_{dam} < 1 \\ C^i_{Mean} - 1, & \text{if} \quad L^i_{dam} > 1 \quad and \quad C^i_{Mean} < 2 \\ 1, & \text{if} \quad L^i_{dam} > 1 \quad and \quad C^i_{Mean} > 2 \end{cases}
\end{aligned}
\tag{5.19}
$$

After applying the aforementioned degradation factors, if damage is occurring in the current analyses, the stress are recomputed based on material property degraded model. A damping factor (beta damping) is then applied into the failure model to improve the numerical analysis stability during finite element solver process, the internal specific energy (per unit mass) is integrated, and finally the subroutine returns the calculated data to the main model.

5.3 Damage Measurement Procedure Automatization

A standard damage measurement procedure is proposed to verify the main damaged area images, creating a damage outline, as proposed based by Tan et al. (2019). The tool has been designed to carry out measurements with minimal human interference. Optionally, the maximum damage length may be also measured to perform a quantitative reference of non-negligible cracks outside the main damage area. As described in the flowchart shown in Figure 5.15, the Python image processing routine begins with the raw image being imported and converted to a grayscale array.

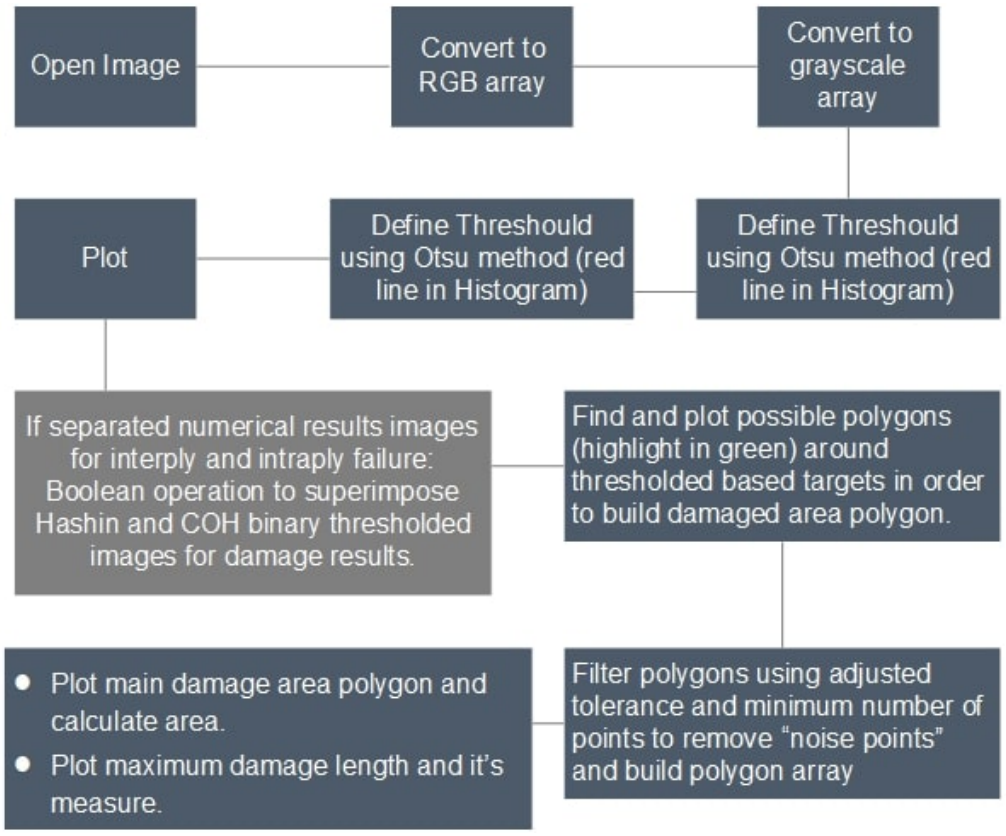

Figure 5.15: Damage Measurement Procedure Flowchart.

Then Otsu's method (Otsu, 1979) is applied to calculate an optimal threshold, maximizing the variance between two classes of pixels and minimizing the intra-class

variance (Walt et al., 2014). It consists in a thresholding technique used in image processing to automatically segment an image into foreground and background by finding the threshold value that maximizes the variance between two classes of pixels. A binary image is then created considering the two classes separated by the threshold line in the histogram (Figure 5.16, in red): values bellow threshold are replaced by zero, and values above threshold are replaced by one.

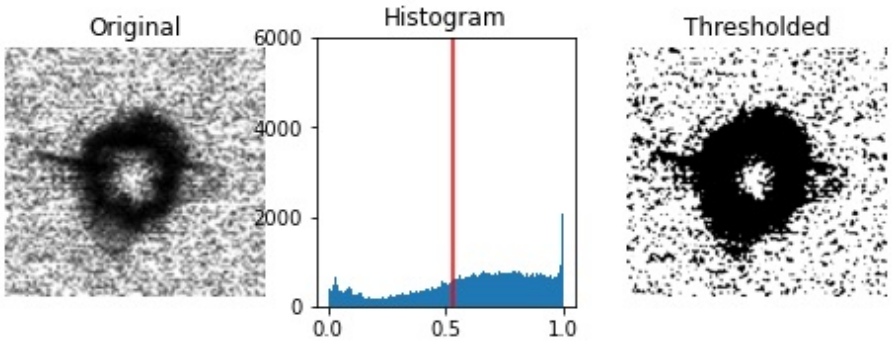

Figure 5.16: Image processing using Otsu's method to set threshold.

After converting the grayscale array to binary array, using threshold as reference, the in-house semi-automatic tool tracks borderline polygons (Figure 5.17 a). Filtering the obtained polygons, it is possible to remove "noisy regions", build the approximated damage polygon array, calculate its area, and (optionally) find the maximum damage length of each damage case (Figure 5.17 b).

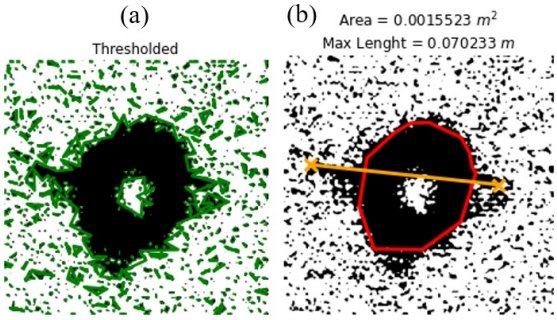

Figure 5.17: Processed image plotting for a typical C-Scan image: (**a**) possible polygons and (**b**) final result.

This procedure was adapted to also measure the main damage area in finite element model graphical results. Focusing in obtaining comparable results to C-Scan images, as proposed by Liu, Liu, Ding, Zhou and Kong (2020), superimposed model images from each ply in the numerical results were used to perform a delamination envelope and an intra-laminar damage envelope. Image to binary process for Hashin and Cohesive damage results are processed separately, as shown in Figure 5.18, and a Boolean operation is used to superimpose both images. Then the routine proceeds finding damage polygon, and calculating its area.

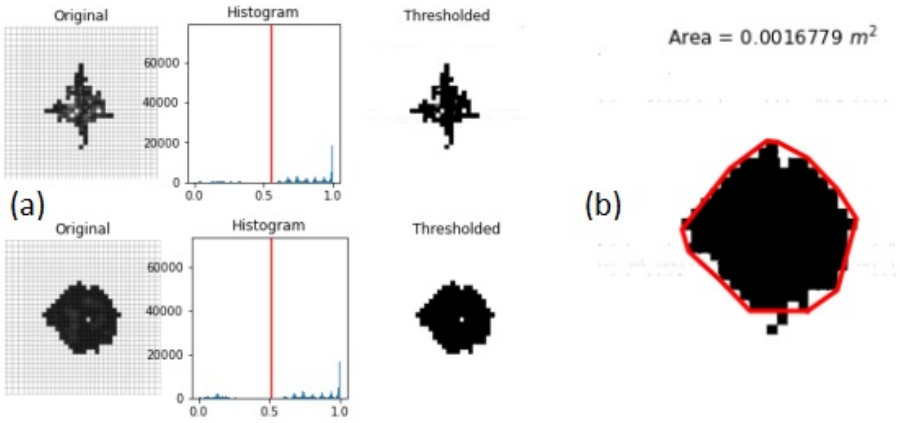

Figure 5.18: Image processing (**a**) and final result (**b**) for a typical numerical case.

Chapter 6

Proposed multiscale methodology verification considering simple load cases in unidirectional composites.

An single element unidirectional tensile/compression lamina plane (X-Y) study was developed aiming verify the proposed model consistency. Figure 6.1 presents a single element model boundary conditions example considering X-direction tensile case. The boundary conditions consists of an single element with normal displacement restrictions at three of its sides, one for each direction. A tensile or compressive lamina plane (X-Y) load is then applied on the opposite face for each direction.

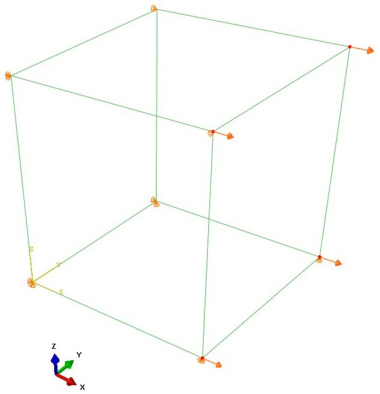

Figure 6.1: Single element model boundary conditions example considering X-direction tensile case.

An unidirectional carbon/epoxy material, $AS4/3501-6$, was defined to each lamina, using the elastic properties shown in Table 6.1 (Herakovich, 1997). It is important to note that the presented material data, obtained from literature, were considered without the application of parametric studies.

Table 6.1: Elastic properties of the unidirectional carbon/epoxy ply.

Lamina elastic parameter description	Value
Young's modulus in 1-direction [MPa]	126000
Young's modulus in 2-direction [MPa]	10500
Young's modulus in 3-direction [MPa]	10500
Poisson's ratio	0.30
Shear modulus [MPa]	5610

As micromechanical model input, an unidirectional carbon/epoxy material micromechanical data was approximated based in available literature parameters (Cuntze and Freund, 2004; Ha et al., 2008; Eizaguirre, 2011; Huang, Jin and Ha, 2012; Yang et al., 2017), considering fiber micromechanical data as presented in Table 6.2. It is important to observe that the applied micro-scale parameters are here considered approximations due to the great dispersion in literature values, mostly presented as numerical approximations, and even to the lack of parameter measurement standardization.

Table 6.2: Aproximated micromechanical fiber data considered in tests.

Fiber parameter description	Value
Longitudinal elastic modulus [MPa]	208000
Transverse elastic modulus [MPa]	54000
In-plane shear modulus [MPa]	27600
In-plane shear modulus [MPa]	6890
Major Poisson's ratio	0.27
Transverse Poisson's ratio	0.30
Fiber maximum longitudinal failure stress - traction [MPa]	2420
Fiber maximum longitudinal failure stress - compression [MPa]	1500

The matrix micromechanical data as presented in Table 6.3

Table 6.3: Aproximated micromechanical matrix data considered in tests.

Matrix parameter description	Value
Elastic modulus [MPa]	2270
Poisson's ratio	0.35
Matrix maximum failure stress - traction [MPa]	45
Matrix maximum failure stress - compression [MPa]	70

And interface data as presented in Table 6.4

Table 6.4: Aproximated micromechanical interface data considered in tests.

Interface parameter description	Value
Interfacial traction strength [MPa]	60
Interfacial shear strength [MPa]	180

Figure 6.2 presents results considering unidirectional results a single element model with unitary length size (1 mm x 1mm x 1 mm) for compressive loading in Y direction (A), tensile loading in Y direction (B), compressive loading in X direction (C), and tensile loading in X direction (D).

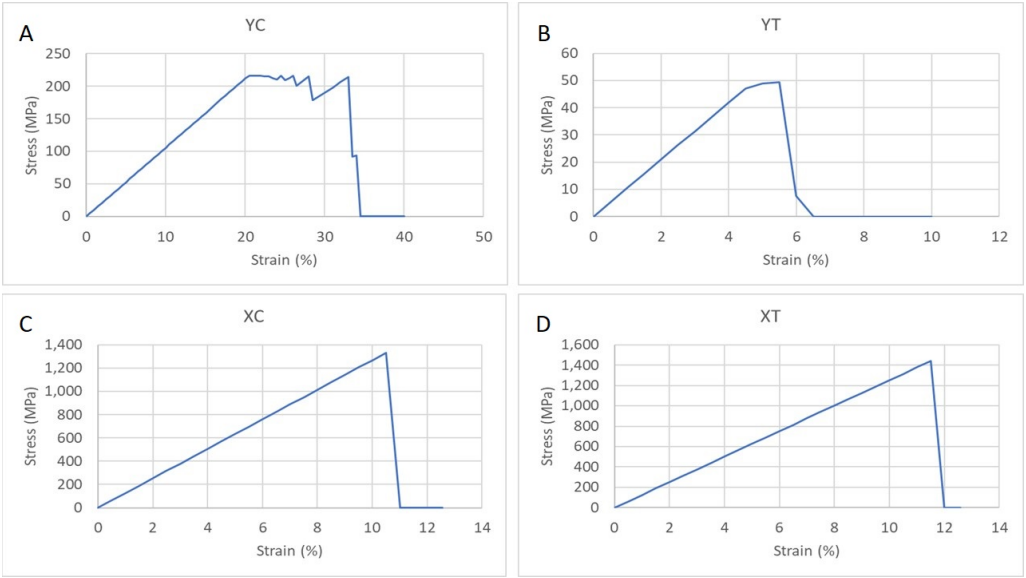

Figure 6.2: Single element unidirectional results: **(A)** compressive loading in Y direction, **(B)** tensile loading in Y direction, **(C)** compressive loading in X direction, **(D)** tensile loading in X direction.

For reference purposes, the experimental allowable strength values adopted in this work are presented in Table 6.5 (Herakovich, 1997).

Table 6.5: Allowable stresses of the unidirectional carbon/epoxy ply.

Lamina damage parameter description	Value
Ultimate tens stress in 1-direction [MPa]	1450
Ultimate comp stress in 1-direction [MPa]	1296
Ultimate tens stress in 2-direction [MPa]	53.4
Ultimate comp stress in 2-direction [MPa]	238

A length parametric result is presented in Figure 6.3, considering single element model results for 0.1 mm, 1 mm, 10 mm and 100 mm, again for compressive loading in Y direction (YC), tensile loading in Y direction (YT), compressive loading in X direction (XC), and tensile loading in X direction (XT). For each case the experimental allowable strength values are included for comparison. The obtained results were considered acceptable as a subroutine initial verification. Also, one may notice that the element size parametric presents no considerable effect in results. Being so, a conventional mesh convergence analysis is indicated when using the proposed model.

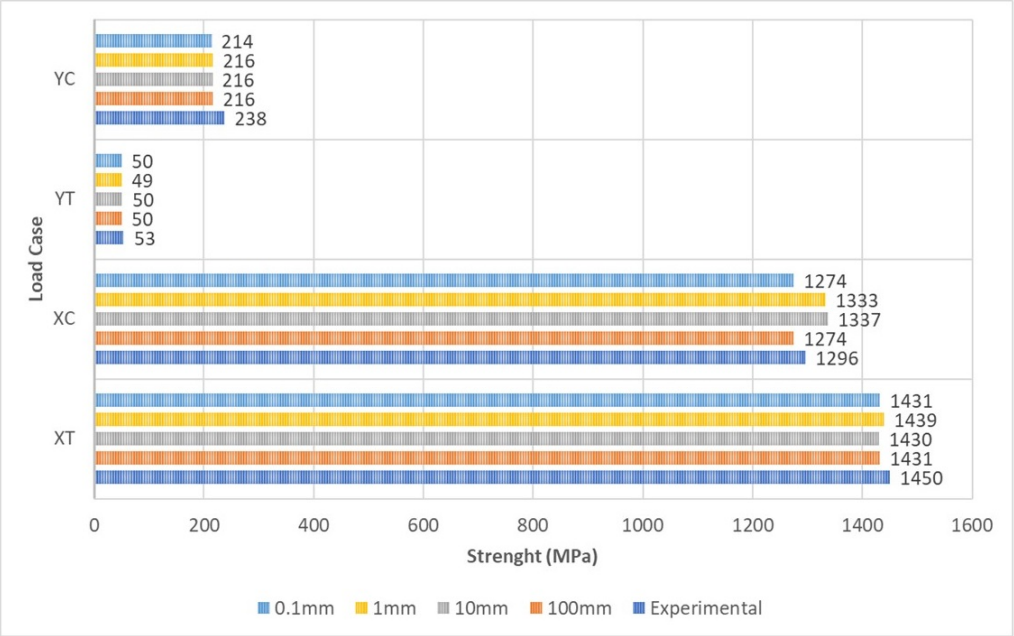

Figure 6.3: Single element model boundary conditions example considering X-direction tensile case.

An unidirectional tensile test study, again considering AS4/3501-6 specimens, was developed aiming to map the effect of fiber direction on the tensile strength behavior of unnotched UD composites. The experimental data considered are summarized in Table 6.6.

Table 6.6: Experimental tests summarized data (Herakovich, 1997)

	Composition	Structure	Manufacturing process	Dimensions	Test specifications
Unidirectional tensile tests	AS4/3501-6	4-ply unidirectional laminate	vacuum drying oven prior to testing	152.4 mm x 12.7 mm x 0.615 mm	tested under axial tension

.

Standard unidirectional models of tension samples (ASTM, 2010) were used in unidirectional force application, as in Figure 6.4.

Figure 6.4: Boundary conditions.

The adopted model mesh size (Figure 6.5), with totals of 2338 elements and 5040 nodes was used for each verification case.

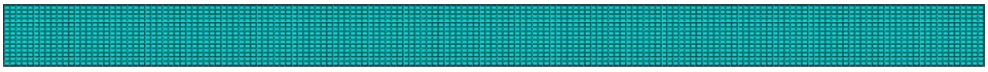

Figure 6.5: Basic mesh distribution.

Figure 6.6 presents examples of experimental tensile tested samples (Herakovich, 1997) where it is possible to observe the failure orientation according to principal axis for different fiber oriented materials.

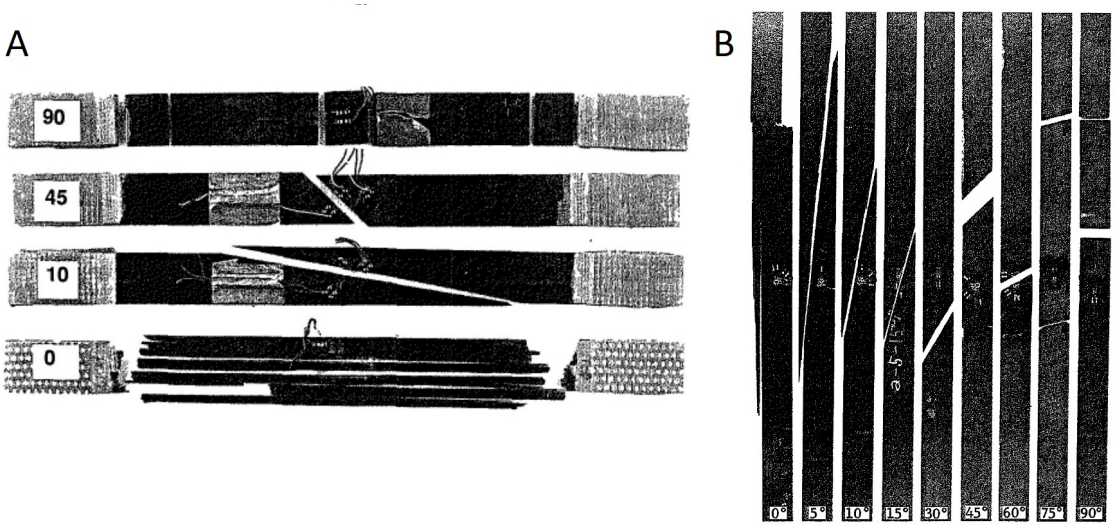

Figure 6.6: Tensile tested samples for T300/934 (**A**) and 6000/PMR-15 (**B**) (Herakovich, 1997).

Focusing on verifying the methodology proposed in section 5.2 the proposed analyzed verifying the failure of the simulated specimens for each fiber direction (Figure 6.7). Besides the proposed simplifications, the obtained numerical results presents similar patterns to the experimental examples (Figure 6.6).

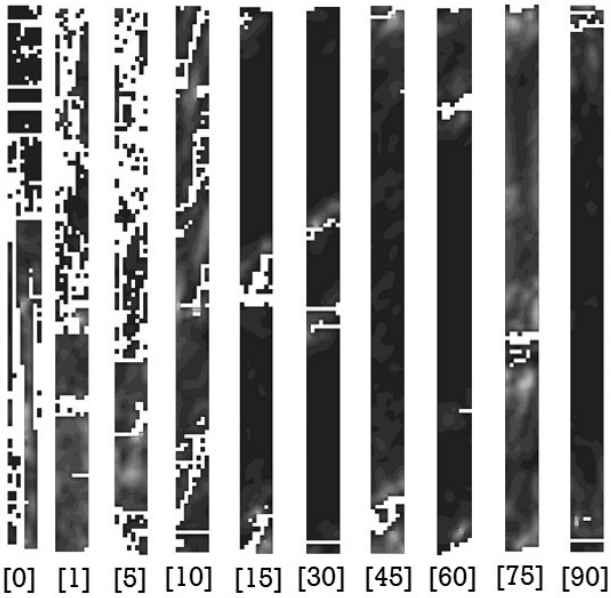

Figure 6.7: Proposed multiscale failure criteria tensile tests applying the proposed methodology.

Figure 6.8 the proposed analyzed verifying the force versus displacement curve foe each simulated fiber direction.

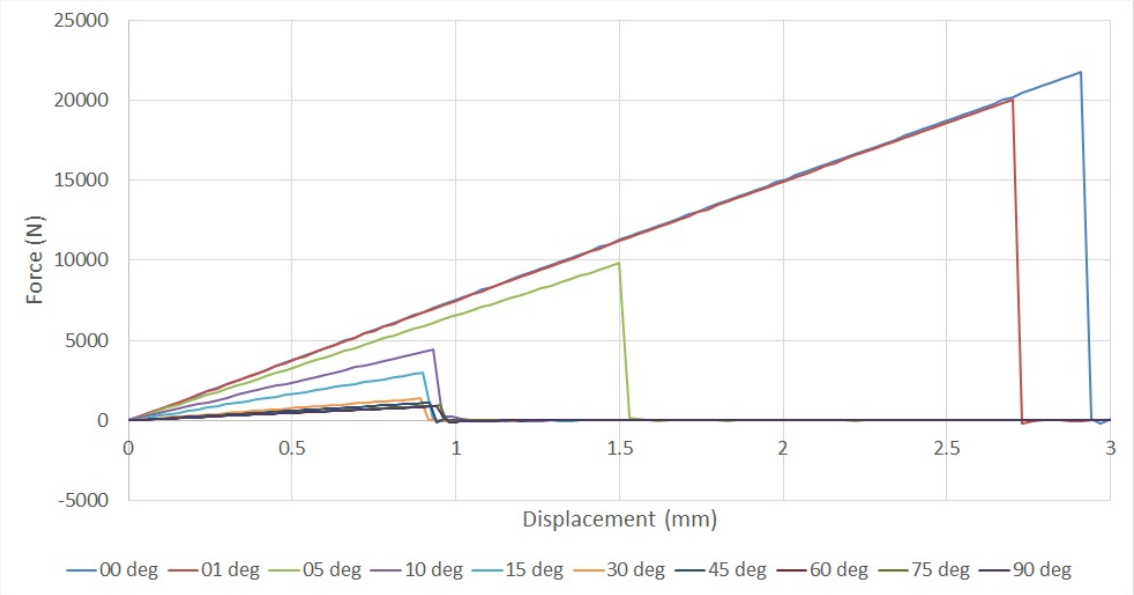

Figure 6.8: Proposed multiscale failure criteria tensile force versus displacement curves.

Figure 6.9 presents the maximum axial tension for each case presented above, again compared with the experimental test data (Test AS4/3501-6) presented by Herakovich (1997).

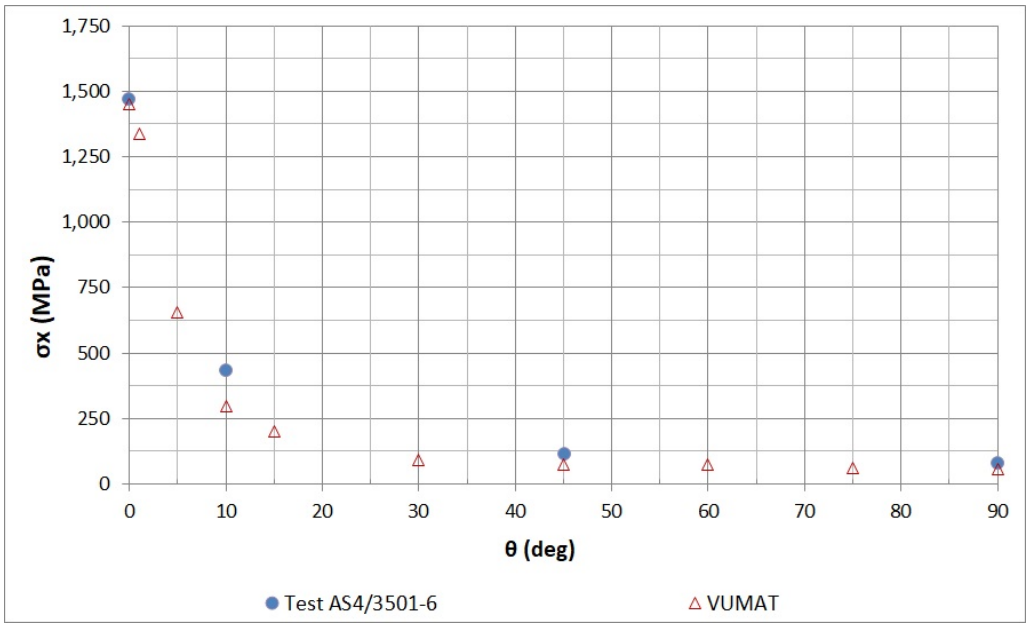

Figure 6.9: Maximum axial tension for each fiber direction configuration.

The same data is presented in Table 6.7, were the errors were calculated using the experimental data as reference. This criterion, even based limited number of results, was considered in following tests.

Table 6.7: Maximum axial tension considering proposed methodology.

	Test AS4/3501-6	VUMAT	
Theta	[MPa]	[MPa]	%Error
0	1470	1450	-1%
1	-	1337	-
5	-	655	-
10	431	297	-31%
15	-	199	-
30	-	91	-
45	112	76	-32%
60	-	75	-
75	-	62	-
90	79	59	-26%

Considering the developed Abaqus® user subroutine (VUMAT), a combined loading test (Figure 6.10) is proposed to be applied in unidirectional laminate models.

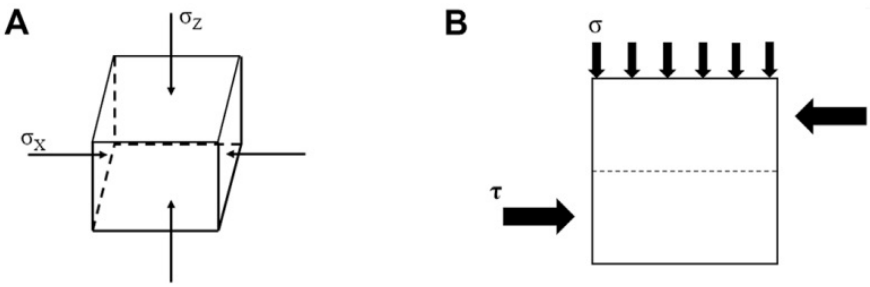

Figure 6.10: Biaxial loading schematic diagram for (**A**) biaxial compression-compression, and (**B**) compression-shear (Zhang et al., 2021).

Combined biaxial compression-compression, tension-compression, tension-tension, tension-shear and compression-shear load cases were them imposed considering a unidirectional laminate in a plane state of stress, as presented in Figure 6.11.

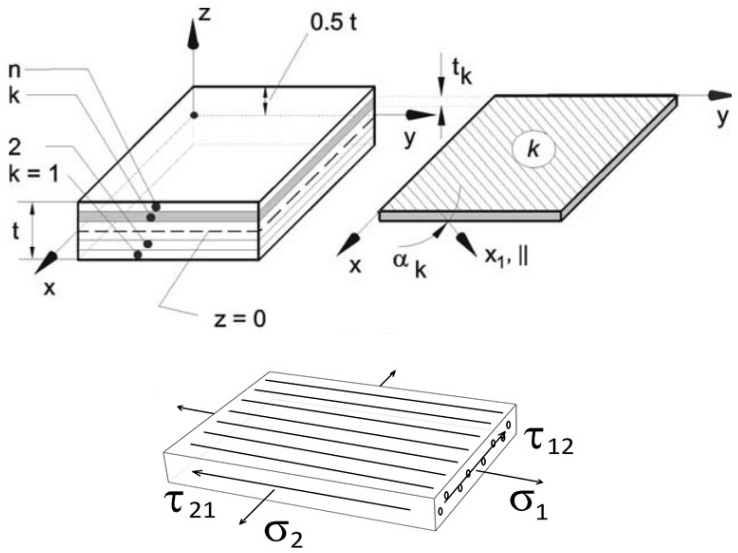

Figure 6.11: Laminate and k^{th} lamina subjected to a plane state of stress (mid-plane z=0) (Adapted from Cuntze and Freund (2004)).

The unidirectional carbon/epoxy lamina elastic properties, for $T300/LY556$ material, were defined based on literature (Huang, Jin and Ha, 2012; Ha et al., 2008), as shown in Table 6.8.

Table 6.8: Approximated elastic properties of the unidirectional $T300/LY556$ carbon/epoxy ply.

Lamina elastic parameter description	Value
Young's modulus in 1-direction [MPa]	129000
Young's modulus in 2-direction [MPa]	5420
Young's modulus in 3-direction [MPa]	5420
Poisson's ratio	0.264
Poisson's ratio	0.264
Poisson's ratio	0.471
Shear modulus [MPa]	1390
Shear modulus [MPa]	1390
Shear modulus [MPa]	1880

Considering fiber micromechanical data as presented in Table 6.9 (Ha et al., 2008).

Table 6.9: Micromechanical fiber data considered in bidirectional loading tests.

Fiber parameter description	Value
Longitudinal elastic modulus [MPa]	230000
Transverse elastic modulus [MPa]	15000
In-plane shear modulus [MPa]	15000
In-plane shear modulus [MPa]	7000
Major Poisson's ratio	0.20
Transverse Poisson's ratio	0.20
Fiber maximum longitudinal failure stress - traction [MPa]	2460
Fiber maximum longitudinal failure stress - compression [MPa]	1500

Matrix micromechanical data as presented in Table 6.10 (Ha et al., 2008).

Table 6.10: Micromechanical matrix data considered in bidirectional loading tests.

Matrix parameter description	Value
Elastic modulus [MPa]	3350
Poisson's ratio	0.35
Matrix maximum failure stress - traction [MPa]	103
Matrix maximum failure stress - compression [MPa]	265

And micromechanical interface data as presented in Table 6.11 (Ha et al., 2008).

Table 6.11: Micromechanical interface data considered in bidirectional loading tests.

Interface parameter description	Value
Interfacial traction strength [MPa]	60
Interfacial shear strength [MPa]	180

A 6 millimeter thick layup model with totals of 25000 elements and 28611 nodes was used for the bidirectional load case configuration, with 3 elements per thickness and no inter-laminar failure criteria considered, as presented in Figure 6.12.

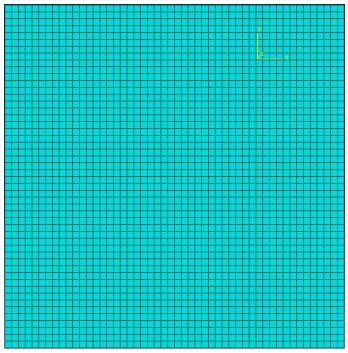

Figure 6.12: Bidirectional loading models mesh configuration.

Figure 6.13 (A) presents the considered boundary conditions for compression-compression, tension-compression and tension-tension load cases, consisting in normal displacement restrictions at two borders of the lamina, applying compressive/tensile loading to the opposite borders. Figure 6.13 (B) presents the considered boundary conditions for tension-shear and compression-shear load cases, consisting in fixed restrictions at one border of the lamina, applying compressive/tensile and shear loading to the opposite border.

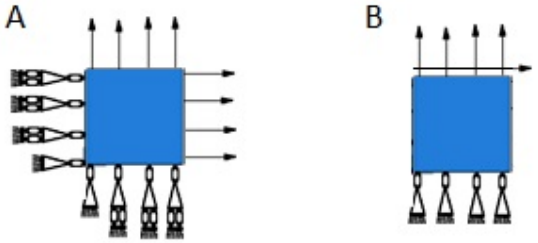

Figure 6.13: Boundary conditions for compression-compression, tension-compression and tension-tension load cases **(A)**, and tension-shear and compression-shear load cases **(B)**.

Again, the obtained results are superposed to literature results obtained from Ha et al. (2008), considering RVE predicted failure envelopes by the MMF in hexagonal and square unit cells configurations (Ha et al., 2008), Tsai-Wu failure criterion (Tsai and Wu, 1971; Ha et al., 2008), and experimental results for

wound tension/compression-torsion tube specimens presented in Ha et al. (2008) and Cuntze and Freund (2004). The experimental data are summarized in Table 6.12.

Table 6.12: Experimental tests summarized data (Ha et al., 2008; Cuntze and Freund, 2004)

	Composition	Structure	Manufacturing process	Dimensions	Test specifications
Biaxial failure envelope	T300/914C unidirectional carbon/epoxy	uniaxial	axially wound prepreg tubes	32 mm in diameter and 1.9–2.3 mm thick	tested under combined axial tension or compression and torsion.

Considering the proposed combined biaxial compression-compression and tension-compression load cases, imposed considering a unidirectional laminate in a plane state of stress, it is possible to obtain a failure stress envelope for unidirectional lamina, as presented in Figure 6.14. For visual comparison purposes, the obtained results are superposed to literature results obtained from Ha et al. (2008), considering RVE predicted failure envelopes by the MMF in hexagonal and square unit cells configurations Ha et al. (2008) and the Tsai-Wu failure criterion (Tsai and Wu, 1971; Ha et al., 2008).

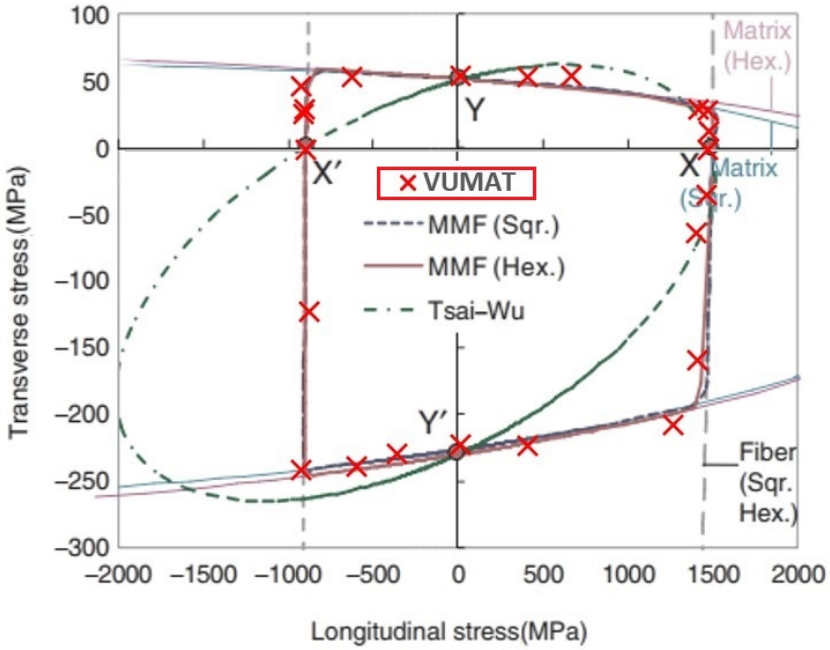

Figure 6.14: Obtained biaxial tension/compression failure stress envelope for unidirectional lamina versus literature results (Ha et al., 2008).

The failure characteristics of composite laminate plates under bidirectional tension/compression loading varies significantly for each load configuration. In composite laminate plates, bidirectional compressive loading can result in buckling, which was avoided in this model due to the aspect ratio of the plate. The most common failure mode observed in the proposed models is matrix failure.

Considering the proposed combined biaxial compression-shear load cases, a failure stress envelope for unidirectional lamina is obtained, as presented in Figure 6.15.

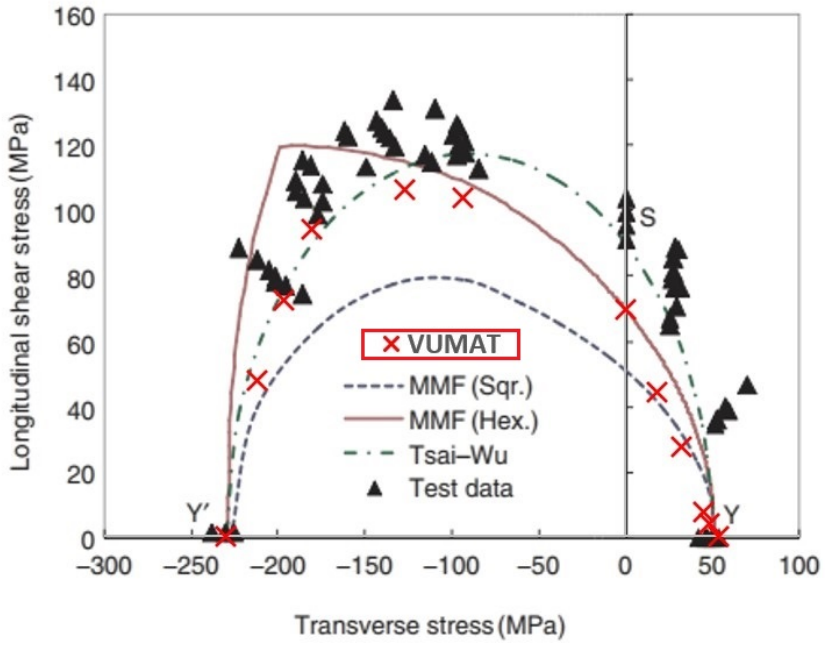

Figure 6.15: Obtained transverse tension/compression versus shear failure stress envelope for unidirectional lamina versus literature results (Ha et al., 2008; Cuntze and Freund, 2004).

Under biaxial compression-shear loading, the magnitude of the applied stresses can affect the failure behavior of the material. In general, when the shear stresses are relatively low compared to the compressive stresses, the failure mode is dominated by compressive failure, at higher shear stresses, the failure mode shifts towards shear failure, and under biaxial compression-shear loading, the plate experiences compressive and shear stresses simultaneously. Matrix failure is still the most common failure mode observed in the proposed models. Considering the proposed multi-scale process simplifications, the conservative results obtained in these studies were considered acceptable for developing the following compression after impact studies.

Chapter 7

Compression After Impact (CAI) virtual test methodology verification

A Compression After Impact (CAI) Virtual Test model is then developed by applying the proposed methodology described in chapter 5, with a semi-automatic model pre and pre and post processing tools. Conventional failure criteria results are compared with simplified multi-scale analysis results, where micromechanical failure criteria for fiber, matrix and interface, are analyzed considering an Octogonal Fiber Model (Huang et al., 2020) based microscale model. The verification studies presented herein were developed based on experimental results presented by Rivallant et al. (2013) and Tan et al. (2015*a*). The experimental data are summarized in Table 7.1.

Table 7.1: Experimental tests summarized data (Rivallant et al., 2013; Tan et al., 2015*a*)

	Composition	Structure	Manufacturing process	Dimensions	Test specifications
Impact	T700/M21 unidirectional carbon/epoxy	$[0_2/45_2/90_2/-45_2]_S$	plate lamination not detailed	150 mm x 100 mm x 4.16 mm (inner unsupported region of 125mm x 75 mm)	drop tower system impact (8 mm radius, 2 kg) considering four impact energies (6.5 J, 17 J, 25 J and 29.5 J)
CAI	T700/M21 unidirectional carbon/epoxy	$[0_2/45_2/90_2/-45_2]_S$	plate lamination not detailed	150 mm x 100 mm x 4.16 mm (inner unsupported region of 130 mm x 90 mm)	hydraulic machine compression (3.75 m/min)

The virtual test set up may be divided in two steps: the first captures the

impact damage, which is imported as the initial condition to the second part, aiming to predict the CAI strength. As proposed by (Tan et al., 2015*a*), the impactor was modelled as a 2 kg spherically shaped rigid surface and four different impact energies (6.5 J, 17 J, 25 J and 29.5 J) were considered. The basic impact configuration is presented in (Figure 7.1 (A)) and represents a drop tower system impact, with an 8 mm impactor radius, following the Airbus Industries Test Method (AIT, 2010). Once the impact simulation is completed, the damaged specimen results are imported to the CAI model, with modified boundary conditions as in (Figure 7.1 (B)).

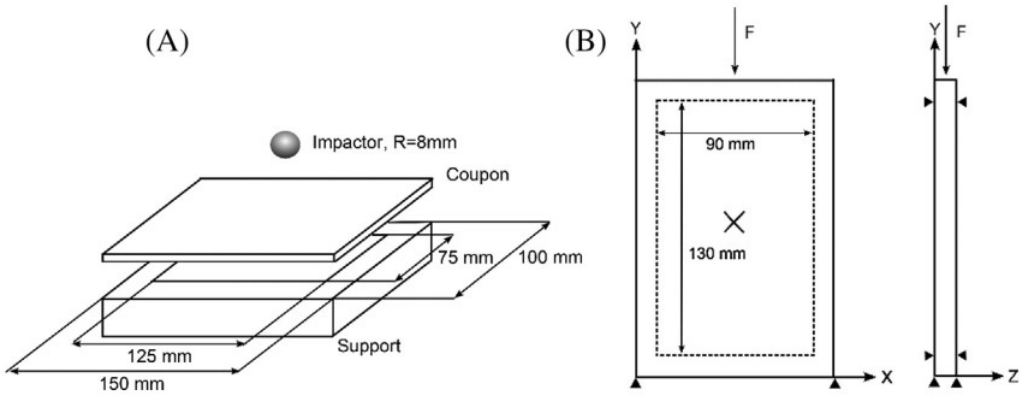

Figure 7.1: Test setup for (**A**) Impact and (**B**) CAI (Tan et al., 2015*a*).

The following five numerical cases were considered in numerical studies. Each result is then compared with experimental results obtained in the literature (Tan et al., 2015*a*).

- **Case 1:** Hashin "2D" criteria without cohesive model;
- **Case 2:** Hashin "2D" criteria with cohesive model;
- **Case 3:** Hashin/Puck-based Nie (2014) "3D" criteria with cohesive model;
- **Case 4:** Hashin "3D" criteria with cohesive model;

- **Case 5:** OFM-based multiscale criteria (3D) with cohesive model.

A mesh convergence analysis was performed considering the T700/M21 carbon/epoxy layup, varying from 42692 to 170948 nodes, as presented in Figure 7.2. The mesh convergence studies model were built considering a conventional model, built using continuum shell elements with Abaqus native Hashin criteria, and cohesive surfaces in each lamina interface (Case 2). The studied specimens consist in a $[0_2/45_2/90_2/-45_2]_S$ laminate and, as proposed by (Tan et al., 2015*a*), only one element through the thickness of each paired ply was used to reduce computational time.

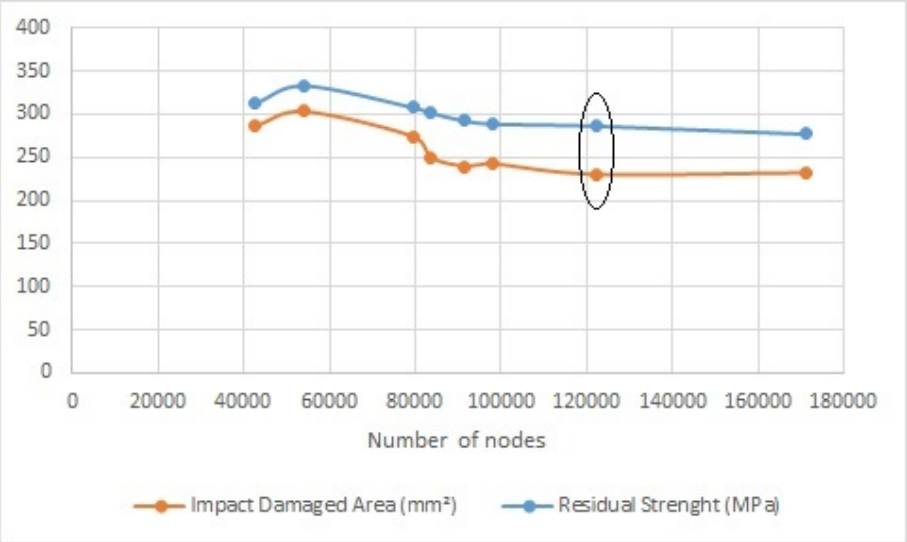

Figure 7.2: Model mesh convergence analysis.

It is important to point out that the mesh convergence analysis was carried out only by varying the size of the elements in the lamina plane. Given the already elevated computational cost of the models, despite the possible gain in results quality, it was considered impractical to increase the number of elements along lamina thickness.

The impact damaged area measurements, for each mesh case, were measured applying the proposed semi-automatic damage measurement procedure (section 5.3), as shown in Figure 7.3.

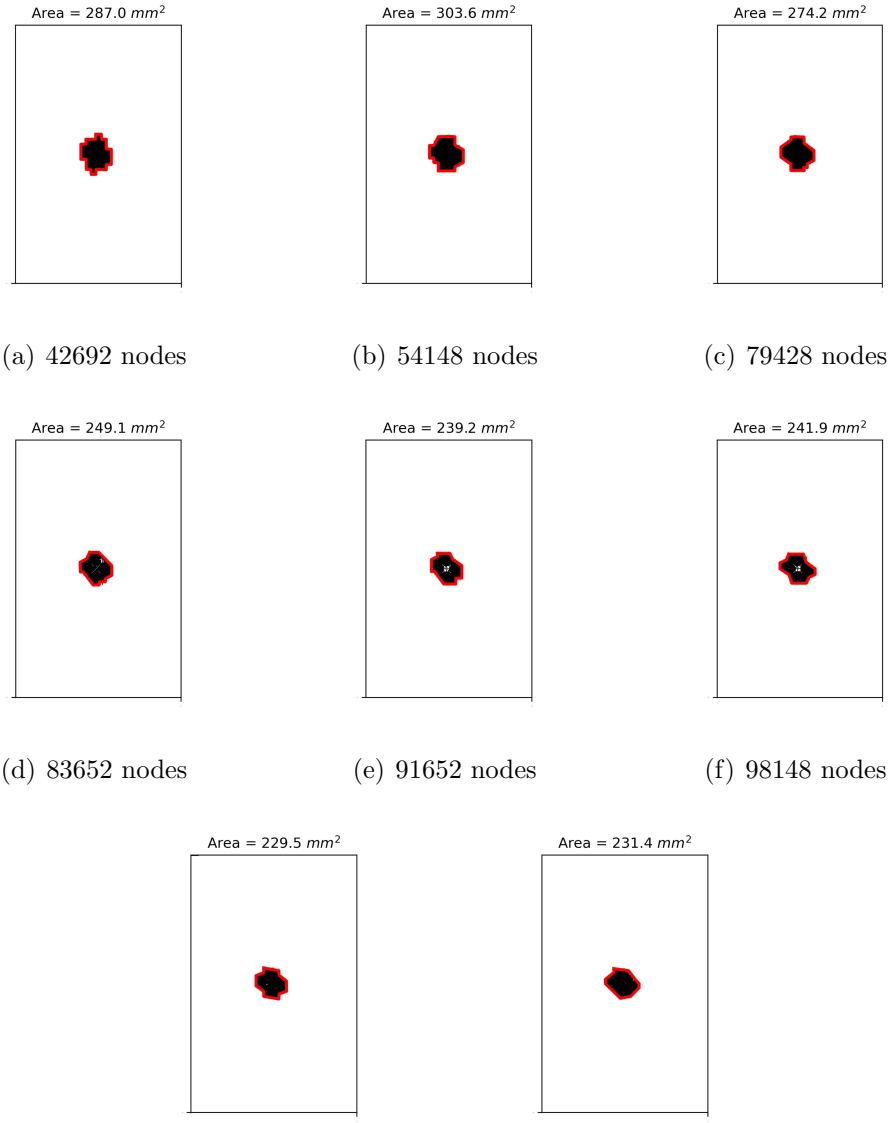

(a) 42692 nodes (b) 54148 nodes (c) 79428 nodes

(d) 83652 nodes (e) 91652 nodes (f) 98148 nodes

(g) **122404 nodes** (h) 170948 nodes

Figure 7.3: Impact damaged area measurements for each model mesh convergence analysis case.

The following results were developed with a mesh consisting of a total number of 122404 nodes and 60427 elements (55336 linear hexahedral and 5091 quadratic

tetrahedral elements). The model configuration, similar to the one used in Tan et al. (2015*a*) numerical tests, is presented in Figure 7.4. For both impact and CAI cases, the frame apparatus model is composed of rigid elements and a contact condition was considered constraining the laminate.

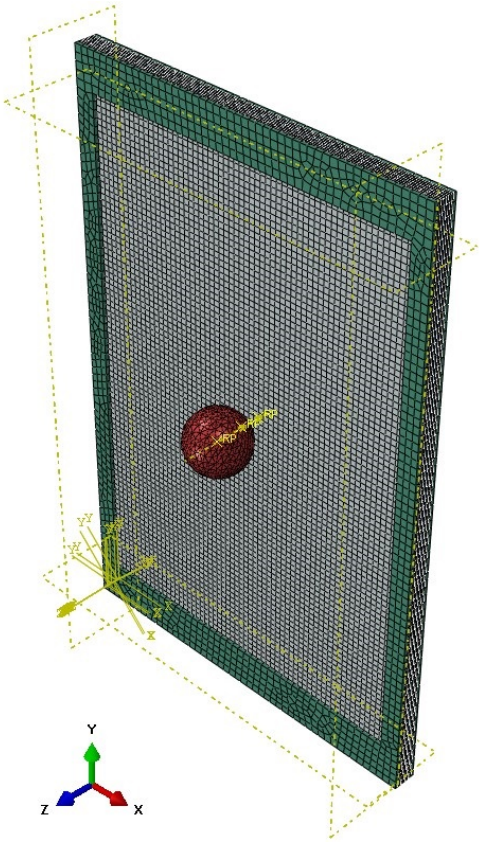

Figure 7.4: Model mesh configuration.

Material properties for unidirectional carbon/epoxy $T700/M21$ material were obtained from Hongkarnjanakul et al. (2013), Rivallant et al. (2013), Tan et al. (2015*a*) and Koloor et al. (2020), considering lamina elastic data, as presented in Table 7.2. The following macro-scale material data, obtained from the literature, were considered for model cases 1 to 4.

Table 7.2: Elastic properties of the unidirectional carbon/epoxy ply.

Lamina elastic parameter description	Value
Young's modulus in 1-direction [MPa]	130000
Young's modulus in 2-direction [MPa]	7700
Young's modulus in 3-direction [MPa]	7700
Poisson's ratio (12)	0.30
Poisson's ratio (13)	0.30
Poisson's ratio (23)	0.35
Shear modulus [MPa] (12)	4800
Shear modulus [MPa] (13)	4800
Shear modulus [MPa] (23)	3800

Allowable strength values, necessary for the macroscale models (cases 1 to 4), were adopted as presented in Table 7.3.

Table 7.3: Allowable stresses of the unidirectional carbon/epoxy ply.

Lamina damage parameter description	Value
Ultimate tens stress in 1-direction [MPa]	2080
Ultimate comp stress in 1-direction [MPa]	1250
Ultimate tens stress in 2-direction [MPa]	60
Ultimate comp stress in 2-direction [MPa]	290
Ultimate tens stress in 2-direction [MPa]	60
Ultimate comp stress in 2-direction [MPa]	290
Ultimate shear stress in 12-direction [MPa]	110
Ultimate shear stress in 13-direction [MPa]	110
Ultimate shear stress in 23-direction [MPa]	110

Fracture energy values, necessary for Abaqus® native energy-based damage evolution in continuum shell macroscale models (cases 1 and 2), were adopted as presented in Table 7.4. It may be observed that the presented values, especially those for the longitudinal direction, may be lower than expected. It is observed that the variation of these values does not influence the results obtained by the proposed multiscale methodology, having these values applied only to conventional models.

Table 7.4: Fracture energy values adopted for the unidirectional carbon/epoxy ply.

Fracture parameter description	Value
Longitudinal Tensile Fracture Energy (N/m)	48.4
Longitudinal Compressive Fracture Energy (N/m)	60.3
Transverse Tensile Fracture Energy (N/m)	4500
Transverse Compressive Fracture Energy (N/m)	8500

And inter-ply cohesive interface properties as presented in Table 7.5. These macro-scale material interface data, obtained from the literature, were used for cohesive surfaces in model cases 2 to 5.

Table 7.5: Interface properties.

Laminate interface parameter description	Value
Normal Fracture Energy [N/mm]	0.500
Shear Fracture Energy [N/mm]	1.600
Maximum nominal stress - Normal [MPa]	20
Maximum nominal stress - Shear [MPa]	36
BK exponent	1.450

The following micro-mechanical data for fiber, matrix and microscale fiber/matrix interface, also taken from the literature, were considered for Case 5. A $T700$ carbon fiber micro-mechanical material data was approximated based in available literature parameters (Eizaguirre, 2011; Hongkarnjanakul et al., 2013; Rivallant et al., 2013; Tan et al., 2015*a*; Kehrer et al., 2020; Toray, 2022), considering data as presented in Table 7.6. It is important to observe that the applied micro-scale parameters are here considered approximations due to the great dispersion in literature values, mostly presented as numerical approximations, and even to the lack of parameter measurement standardization.

Table 7.6: Approximated micro-mechanical fiber data considered in tests.

Fiber parameter description	Value
Longitudinal elastic modulus [MPa]	230000
Transverse elastic modulus [MPa]	13800
In-plane shear modulus [MPa]	8960
In-plane shear modulus [MPa]	4830
Major Poisson's ratio	0.27
Transverse Poisson's ratio	0.30
Fiber maximum longitudinal failure stress - traction [MPa]	3420
Fiber maximum longitudinal failure stress - compression [MPa]	1930

For $M21$ epoxy, a material data was approximated based on available literature parameters (Hongkarnjanakul et al., 2013; Rivallant et al., 2013; Tan et al., 2015*a*; Kehrer et al., 2020; Hexcel, 2022), considering micromechanical matrix data as presented in Table 7.7

Table 7.7: Approximated micro-mechanical matrix data considered in tests.

Matrix parameter description	Value
Elastic modulus [MPa]	3500
Poisson's ratio	0.35
Matrix maximum failure stress - traction [MPa]	70
Matrix maximum failure stress - compression [MPa]	226

For $T700/M21$ carbon/epoxy micro-mechanical fiber/matrix interface, data was again approximated based on available literature parameters (Ha et al., 2008), as presented in Table 7.8

Table 7.8: Approximated micro-mechanical interface data considered in tests.

Interface parameter description	Value
Interfacial traction strength [MPa]	60
Interfacial shear strength [MPa]	180

It is important to note that the presented material data, obtained from literature, were considered without the application of parametric studies. The input data variation can significantly affect the results of a numerical model, improving its reliability, and avoiding possible biases in the model results.

Experimental impact damaged area, forces and residual strengths measurements results for this case of study may be found in Hongkarnjanakul et al. (2013); Rivallant et al. (2013); Tan et al. (2015*a*). Since the experimental impact damaged area results were presented as a damage envelope in Tan et al. (2015*a*), the measurement approximations presented in Figure 7.6 (A) were considered here as reference in the

following studies. At first, the models cases 1 and 2 were compared. In the first case (**Case 1**) the proposed model was analyzed considering continuum shell elements, using the Abaqus native form of the Hashin criterion (subsection 3.1.1) and the also native energy-based linear progressive damage model (Table 7.9).

Table 7.9: Case 1 summarized failure model.

Failure mode		Variable	Degradation process	Degraded terms
Hashin	Fiber tension	F_f^T	strain-softening	C_d
	Fiber compression	F_f^C	strain-softening	C_d
	Matrix tension	F_m^T	strain-softening	C_d
	Matrix compression	F_m^C	strain-softening	C_d

In **Case 2**, keeping the same intralaminar criterion as in Case 1, an interlaminar cohesive failure criterion, described in section 3.2, was added (Table 7.10).

Table 7.10: Case 2 summarized failure model.

Failure mode		Variable	Degradation process	Degraded terms
Hashin	Fiber tension	F_f^T	energy based strain-softening	C_d
	Fiber compression	F_f^C	energy based strain-softening	C_d
	Matrix tension	F_m^T	energy based strain-softening	C_d
	Matrix compression	F_m^C	energy based strain-softening	C_d
Cohesive	Maximum stress criterion	-	energy based strain-softening	δ_n^o δ_s^o δ_t^o

Figure 7.5 presents the obtained maximum strain distribution, considering 6.5 J impact, for Case 1 and Case 2.

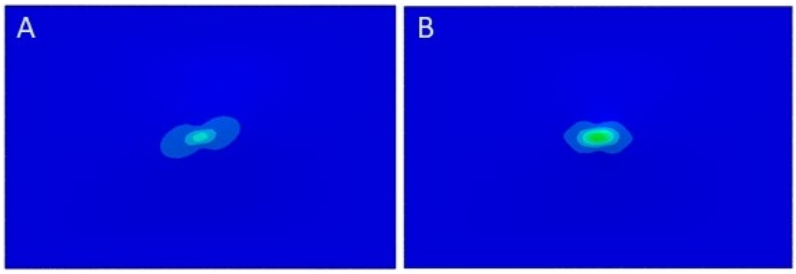

Figure 7.5: Maximum strain distribution considering 6.5 J impact: **(A) Case 1:** 2D model without cohesive surfaces using native Hashin failure criterion, **(B) Case 2:** 2D model including cohesive surfaces using native Hashin failure criterion.

The proposed semi-automatic damage measurement procedure (section 5.3) is then capable to proceed with the damaged area measurement. For a 6.5 J impact case, it is possible to observe the absence of damage for case 1 (without cohesive surfaces, Figure 7.6 (B)) and a damage closer to the experimental for Case 2 (Figure 7.6 (C)), given by the existence of a cohesive model, which makes interface damage possible in numerical results.

Figure 7.6: Damaged area considering 6.5 J impact: **(A) Experimental** (Tan et al., 2015*a*), **(B) Case 1:** 2D model without cohesive surfaces using native Hashin failure criterion, **(C) Case 2:** 2D model including cohesive surfaces using native Hashin failure criterion.

As presented in Figure 7.7 (A), the experimental data of force along the impact, for this case, present only data of maximum load, which was exceeded by the numerical data in both cases. For the impact force versus displacement in impact case (Figure 7.7 (B)), and for stress versus displacement in the CAI case (Figure 7.7

(C)), there is a better correlation for case 2 (with cohesive surfaces), which may be justified by the presence of damage due to the impact.

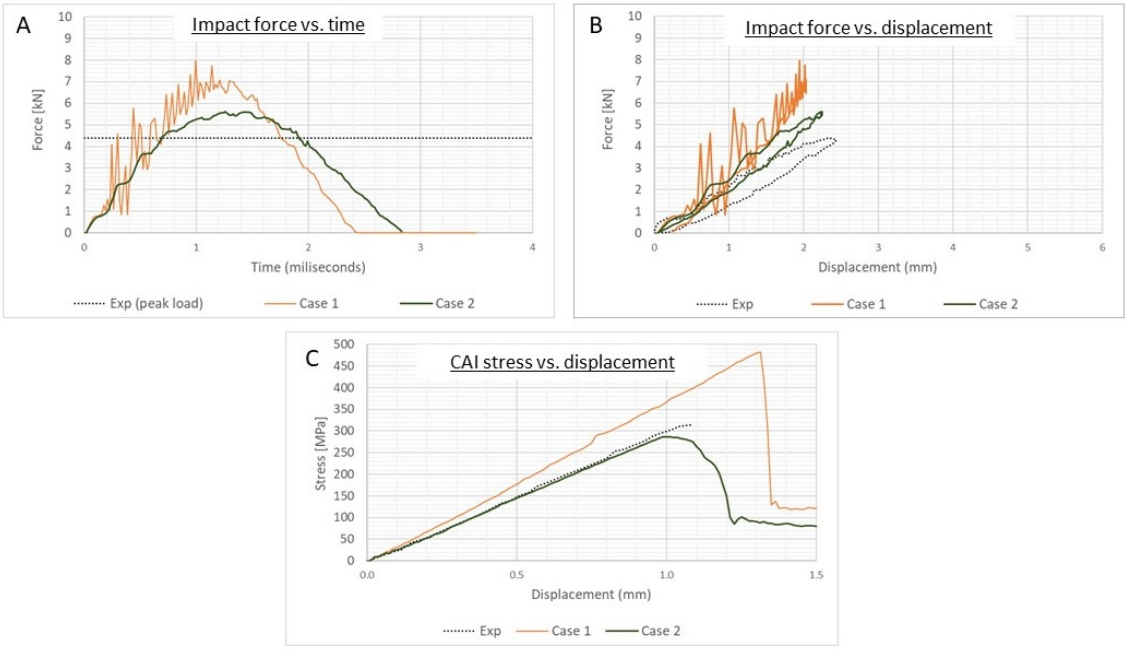

Figure 7.7: Virtual test measurements for Cases 1 and 2 considering 6.5 J impact: **(A)** Impact force vs. time, **(B)** Impact force vs. displacement, **(C)** CAI stress vs. displacement.

Figure 7.8 presents the obtained maximum strain distribution, considering 17 J impact, for Case 1 and Case 2.

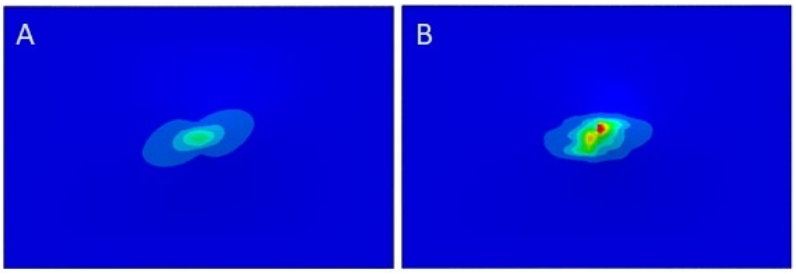

Figure 7.8: Maximum strain distribution considering 17 J impact: **(A) Case 1:** 2D model without cohesive surfaces using native Hashin failure criterion, **(B) Case 2:** 2D model including cohesive surfaces using native Hashin failure criterion.

For a 17J impact case, one can observe almost no damage for case 1 (without cohesive surface, Figure 7.9 (B)) and again a lower damage than the experimental (top) for case 2 (with cohesive surface, Figure 7.9 (C)) given by the existence of a model that allows delamination.

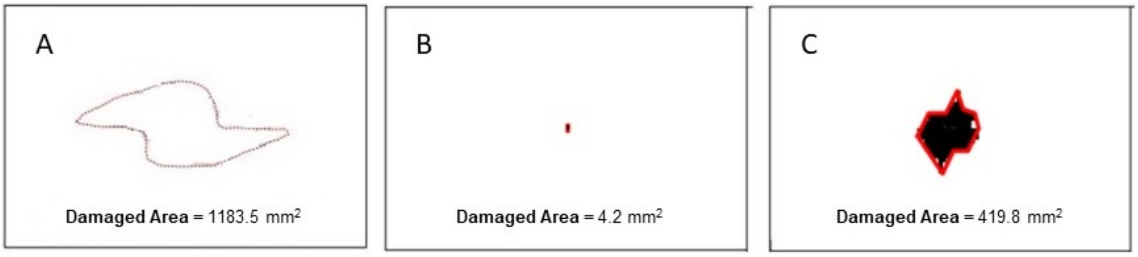

Figure 7.9: Damaged area considering 17 J impact: **(A) Experimental** (Tan et al., 2015*a*), **(B) Case 1:** 2D model without cohesive surfaces using native Hashin failure criterion, **(C) Case 2:** 2D model including cohesive surfaces using native Hashin failure criterion.

Experimental force data along impact time and along displacement are not presented for this energy case. Figure 7.10 presents the impact measured force along time (A) and along displacement (B) for both cases. For the stress versus displacement in the CAI case (Figure 7.10 (C)), there is again a better correlation for case 2, which may be justified by the presence of damage due to the impact.

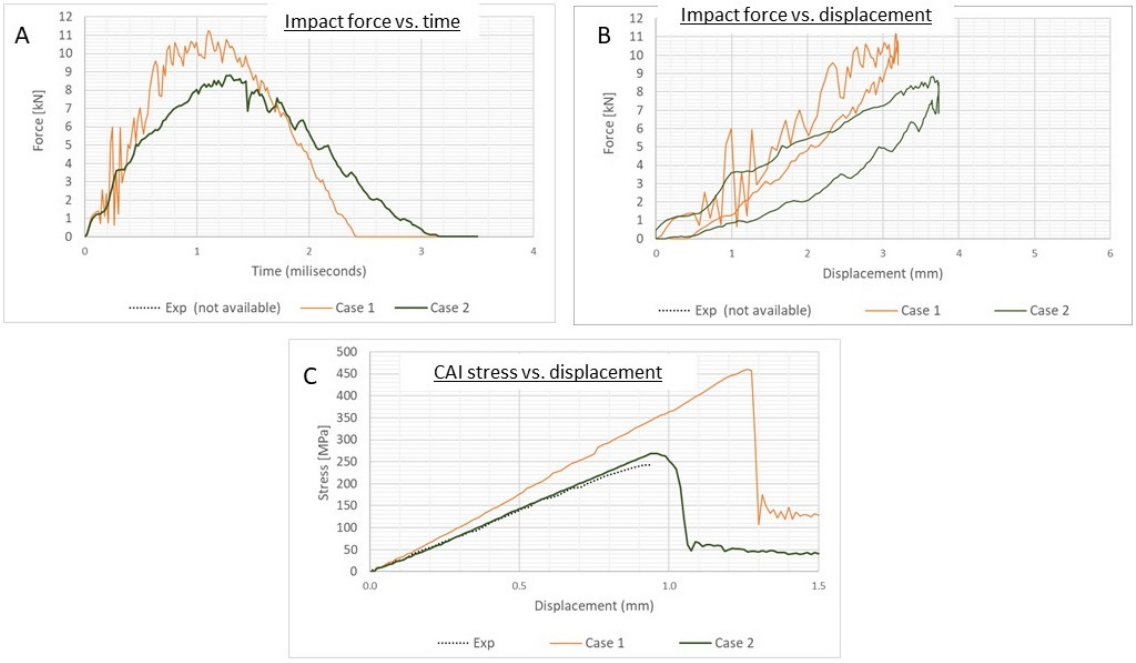

Figure 7.10: Virtual test measurements for Cases 1 and 2 considering 17 J impact: **(A)** Impact force vs. time, **(B)** Impact force vs. displacement, **(C)** CAI stress vs. displacement.

Figure 7.11 presents the obtained maximum strain distribution, considering 25 J impact, for Case 1 and Case 2.

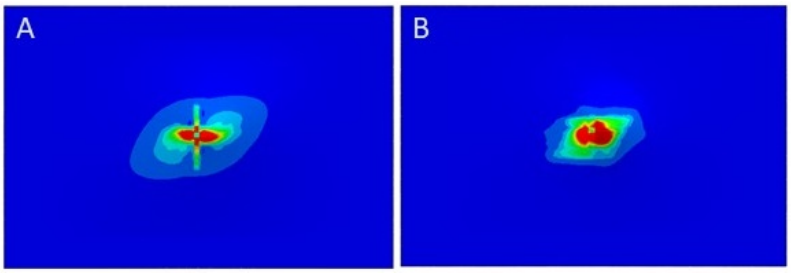

Figure 7.11: Maximum strain distribution considering 25 J impact: **(A) Case 1:** 2D model without cohesive surfaces using native Hashin failure criterion, **(B) Case 2:** 2D model including cohesive surfaces using native Hashin failure criterion.

For a 25 J impact case, it is possible to observe the damage concentration for Case 1 (Figure 7.12 (B)) and again a considerably greater damage for Case 2 (Figure 7.12

(C)), although still smaller than the experimental (Figure 7.12 (A)), given by the existence of a model that allows delamination in numerical results.

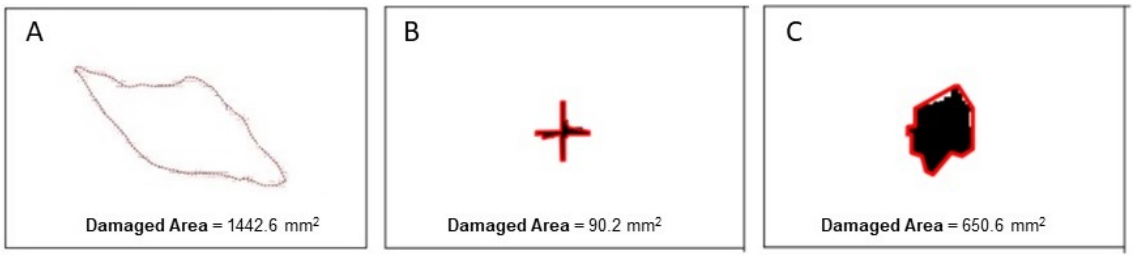

Figure 7.12: Damaged area considering 25 J impact: **(A) Experimental** (Tan et al., 2015*a*), **(B) Case 1:** 2D model without cohesive surfaces using native Hashin failure criterion, **(C) Case 2:** 2D model including cohesive surfaces using native Hashin failure criterion.

The experimental force data along impact time can be observed in the Figure 7.13 (A), and experimental force data along displacement can be observed in the Figure 7.13 (B), where, despite the difference in behavior, it was observed that the maximum obtained value is closer for case 2. No experimental data for stress versus displacement were presented in this CAI case. Figure 7.13 (C) presents the CAI measured force along time for both cases.

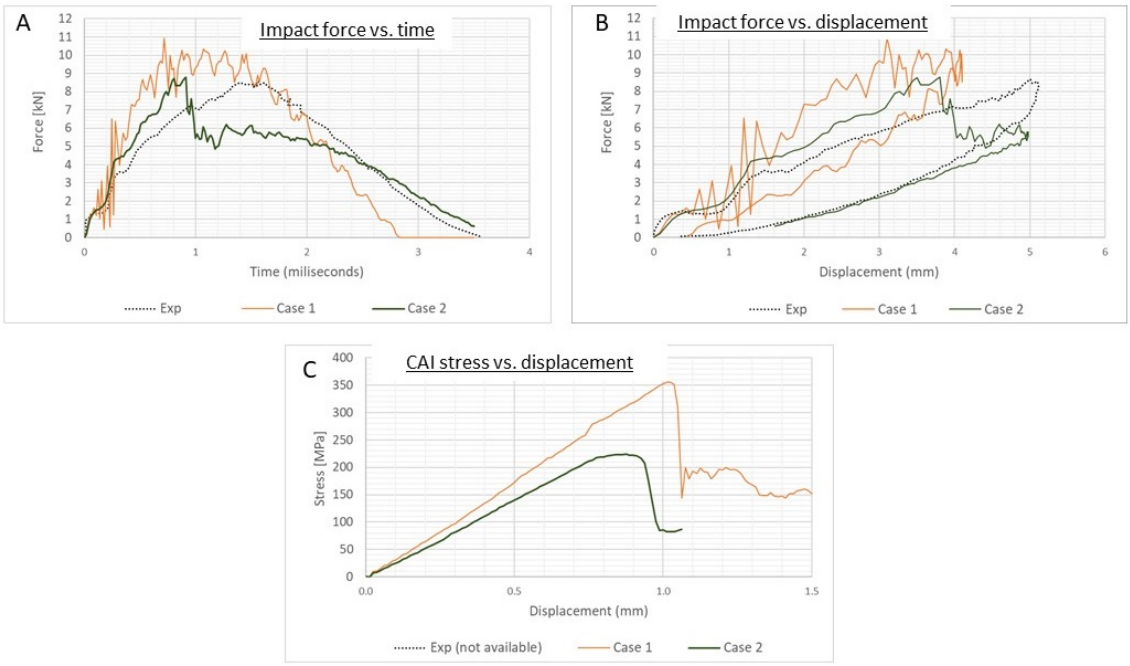

Figure 7.13: Virtual test measurements for Cases 1 and 2 considering 25 J impact: **(A)** Impact force vs. time, **(B)** Impact force vs. displacement, **(C)** CAI stress vs. displacement.

Figure 7.14 presents the obtained maximum strain distribution, considering 29.5 J impact, for Case 1 and Case 2.

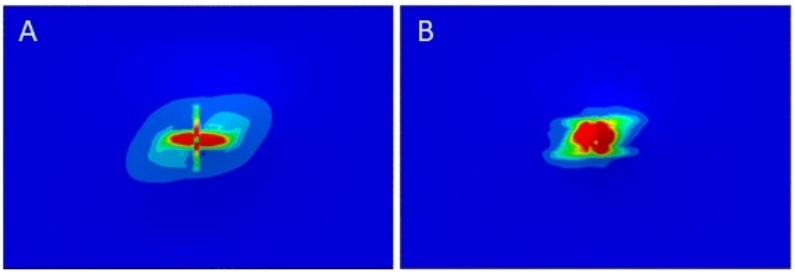

Figure 7.14: Maximum strain distribution considering 29.5 J impact: **(A) Case 1:** 2D model without cohesive surfaces using native Hashin failure criterion, **(B) Case 2:** 2D model including cohesive surfaces using native Hashin failure criterion.

For a 29.5 J impact case, it is again possible again observe the damage concentration for case 1 (Figure 7.15 (B)) and a damage area value closer to the experimental

(Figure 7.15 (A)) for case 2 (Figure 7.15 (C)), given by the existence of a model that allows delamination.

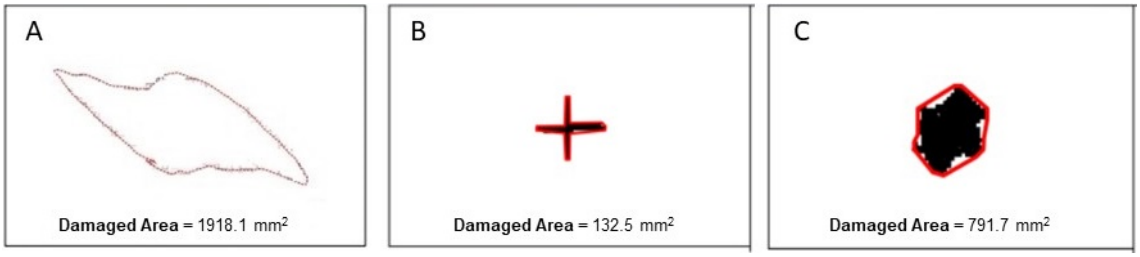

Figure 7.15: Damaged area considering 29.5 J impact: **(A) Experimental** (Tan et al., 2015*a*), **(B) Case 1:** 2D model without cohesive surfaces using native Hashin failure criterion, **(C) Case 2:** 2D model including cohesive surfaces using native Hashin failure criterion.

As shown in Figure 7.16 (A), the experimental data for impact force over time, for this case, presents only maximum load data, again with case 2 results closer to the experimental. Experimental force data along displacement can be observed in the Figure 7.16 (B) where, despite the difference in behavior, it was observed a better correlation for case 2. For CAI stress versus displacement (Figure 7.16 (C)), a better correlation is again observed for case 2, despite the maximum value being exceeded in both cases.

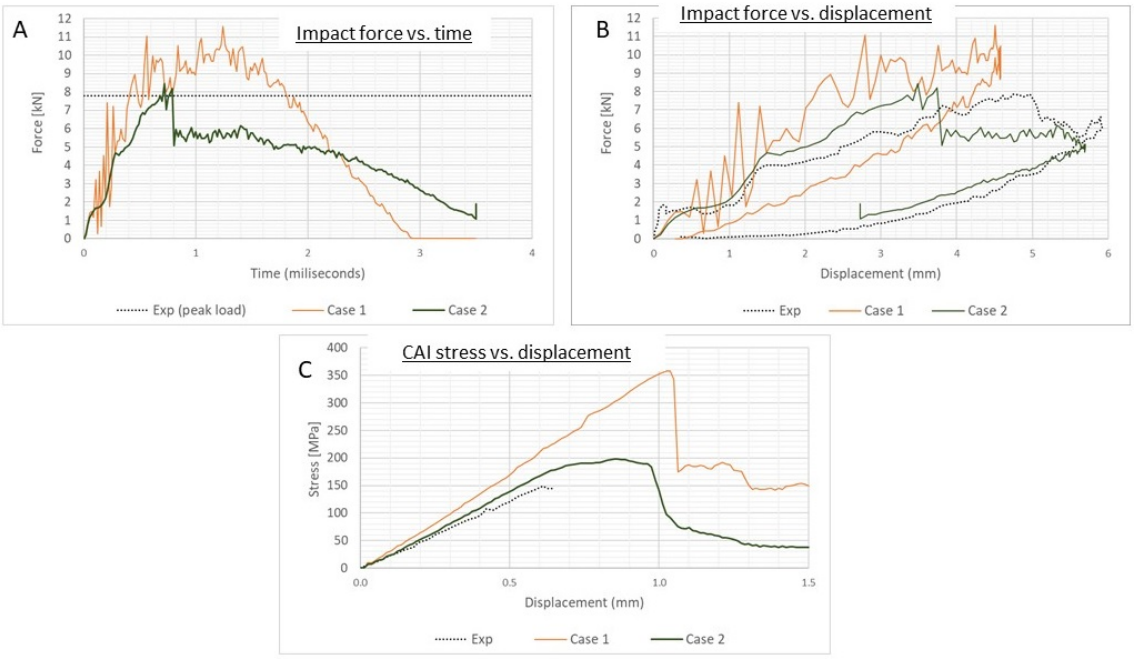

Figure 7.16: Virtual test measurements for Cases 1 and 2 considering 29.5 J impact: **(A)** Impact force vs. time, **(B)** Impact force vs. displacement, **(C)** CAI stress vs. displacement.

Observing the damage areas obtained for the two model configurations and 4 analyzed energies (Figure 7.17), and compared with the experimental data from the literature, it is possible to conclude that delamination is an important effect to be taken into account for the impact, even though both models showed smaller damages if compared to the experimental ones.

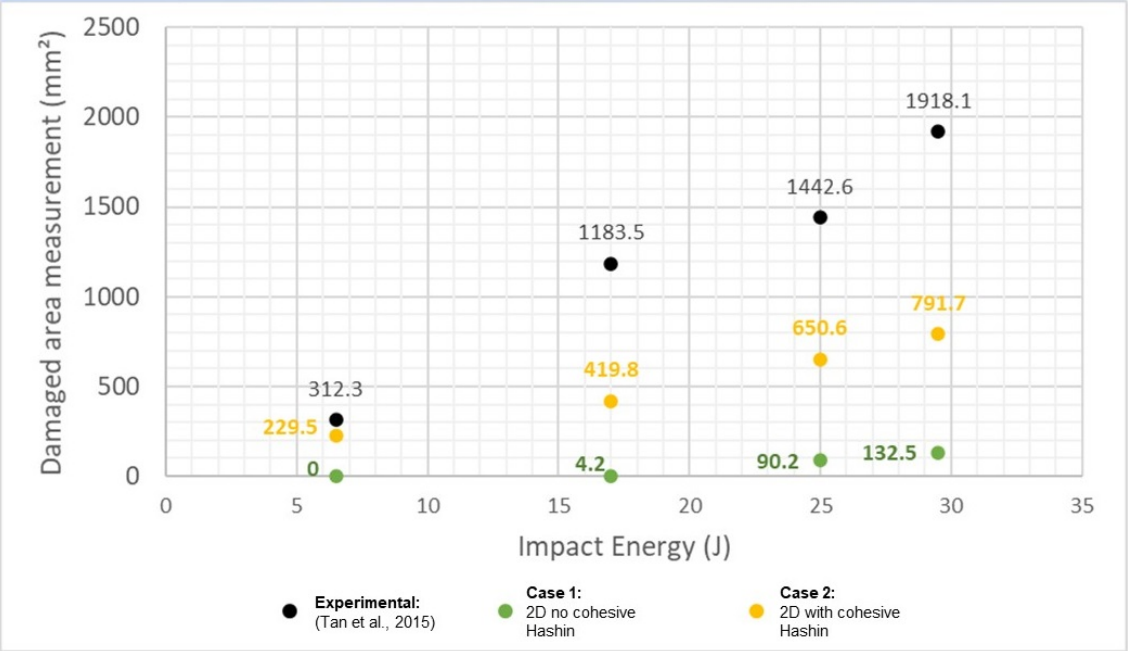

Figure 7.17: Simulation vs. experimental damaged area (Cases 1 and 2).

Observing the residual strength for each value of impact energy (Figure 7.18), it is again possible to conclude that delamination (cohesive model) is an important effect to be taken into account for impact. It is observed that Case 2 presents results considerably near to the experimental ones, even with the simplicity of the continuum shell model.

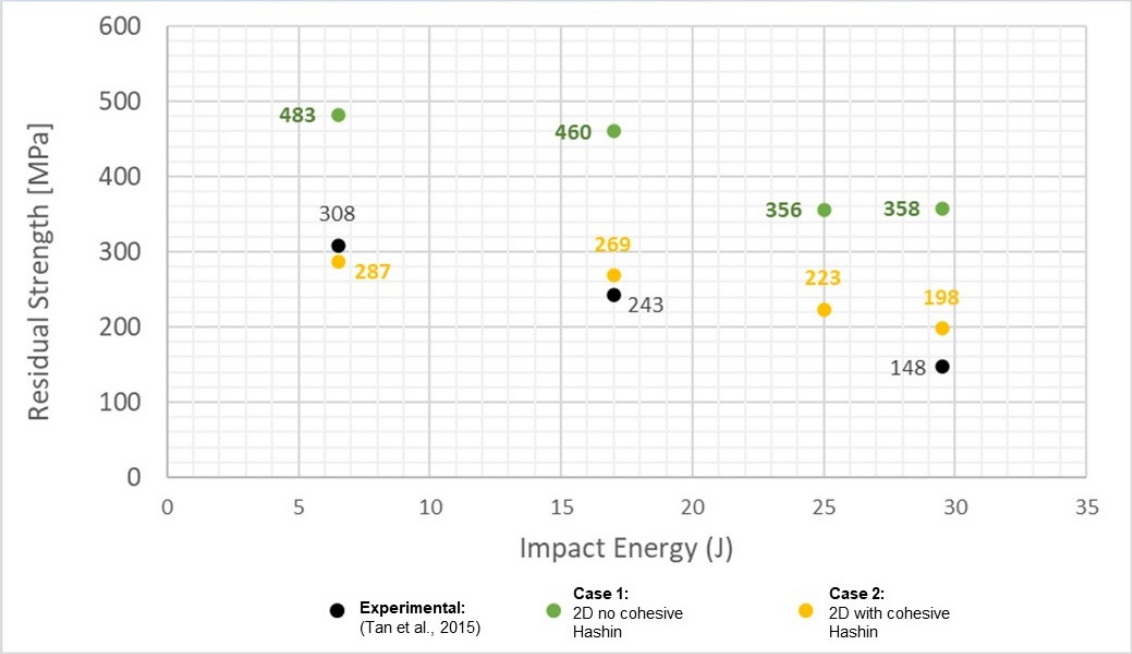

Figure 7.18: Simulation vs. experimental residual strength (Cases 1 and 2).

Considering the models cases 3 and 4, which use "3D" elements and failure criteria via VUMAT, the following numerical-experimental correlations can be observed. In the following cases, the use of the cohesive failure criterion is maintained and three-dimensional instead of continuum shell elements. In **Case 3** (Table 7.11), for the intralaminar failure, the subroutine *uniFiber.f*, which is available in Abaqus® documentation (Dassault Systemes, 2014; Nie, 2014) was applied. In this VUMAT it is possible to observe the criteria proposed by Nie (2014), applying Hashin criterion (Hashin, 1980) for fiber direction, and a criterion based in Puck's plane of action theory Puck and Schurmann (1998) for tension and compression for failure perpendicular to the fiber, as described in subsection 3.1.2.

Table 7.11: Case 3 summarized failure model.

Failure mode		Variable	Degradation process	Degraded terms
Constitutive model proposed by Nie	Fiber tension	F_f^T	abrupt	C_d
	Fiber compression	F_f^C	abrupt	C_d
	Matrix tension	F_m^T	abrupt	C_d
	Matrix compression	F_m^C	abrupt	C_d
Cohesive	Maximum stress criterion	-	energy based strain-softening	δ_n^o δ_s^o δ_t^o

In **Case 4** (Table 7.12), the modified VUMAT proposed in the thesis is considered. In this modification it is proposed to consider Hashin criterion (Hashin, 1980) for both fiber and matrix directions. The Hashin criterion in its conventional form is proposed for the plane stress state. In order not to completely disregard the out-of-plane stresses from the tree-dimensional elements, it was proposed here to consider the equations presented in Hashin's original article just before the plane stress simplifications. The modified subroutine, like the original one, was kept without progressive damage (binary failure) and the cohesive failure criterion was considered in the model.

Table 7.12: Case 4 summarized failure model.

Failure mode		Variable	Degradation process	Degraded terms
Three dimensional Hashin's criteria	Fiber tension	F_f^T	abrupt	C_d
	Fiber compression	F_f^C	abrupt	C_d
	Matrix tension	F_m^T	abrupt	C_d
	Matrix compression	F_m^C	abrupt	C_d
Cohesive	Maximum stress criterion	-	energy based strain-softening	δ_n^o δ_s^o δ_t^o

Figure 7.19 presents the obtained maximum strain distribution, considering 6.5 J impact, for Case 3 and Case 4.

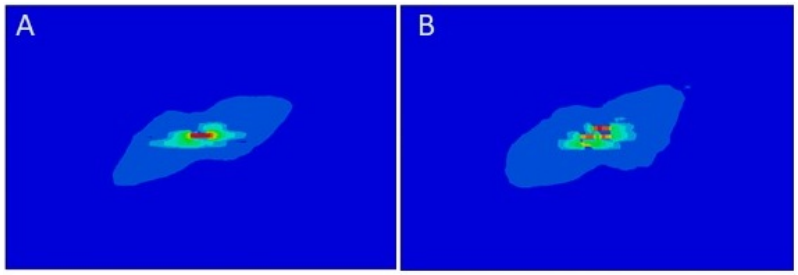

Figure 7.19: Maximum strain distribution considering 6.5 J impact: **(A) Case 3:** 3D model including cohesive surfaces using Abaqus available VUMAT with Hashin-Puck-based Nie (2014) failure criterion, **(B) Case 4:** 3D model including cohesive surfaces using modified VUMAT with Hashin extended failure criterion.

Applying the proposed semi-automatic damage measurement procedure (section 5.3) for a 6.5 J impact case, we can observe similar damage area measurements for both numerical cases, with values close to the experimental (Figure 7.20).

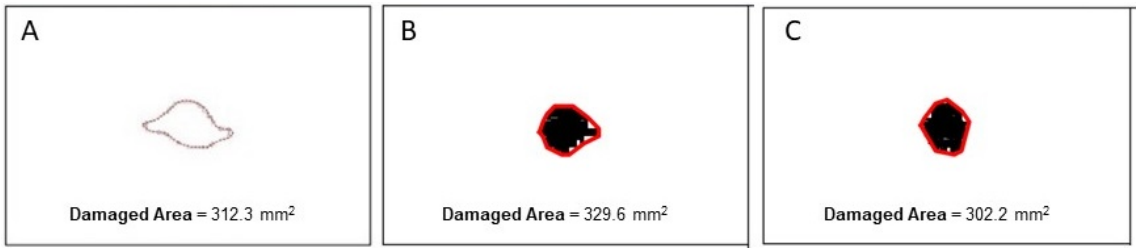

Figure 7.20: Damaged area considering 6.5 J impact: **(A) Experimental** (Tan et al., 2015*a*), **(B) Case 3:** 3D model including cohesive surfaces using Abaqus available VUMAT with Hashin-Puck-based Nie (2014) failure criterion, **(C) Case 4:** 3D model including cohesive surfaces using modified VUMAT with Hashin extended failure criterion.

As shown in Figure 7.21 (A), the experimental data of force along the impact, for this case, present only data of maximum load, which was reached only in the peaks of the numerical simulations in both cases. Probably due the lack of progressive damage model, both cases presents poor correlation for impact force versus displacement in impact case (Figure 7.21 (B)). For the stress versus displacement in the CAI case (Figure 7.21 (C)), a better correlation is observed for case 3 (Hashin/puck-based

Nie (2014)), although in both cases the maximum stress results were lower than the experimental ones.

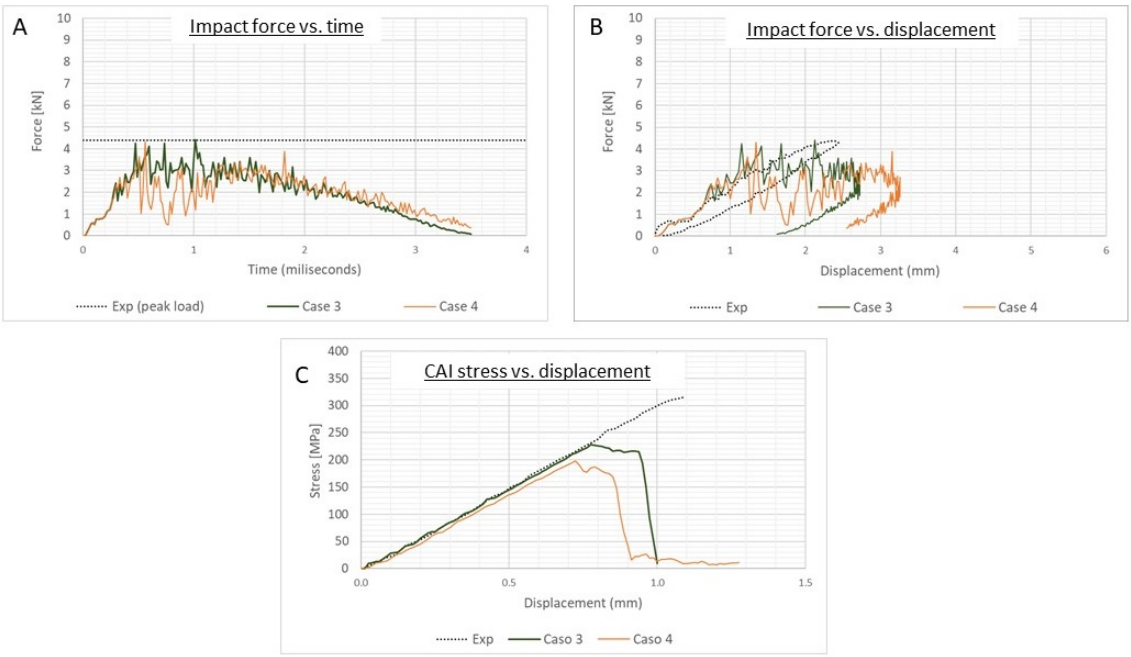

Figure 7.21: Virtual test measurements for Cases 3 and 4 considering 6.5 J impact: **(A)** Impact force vs. time, **(B)** Impact force vs. displacement, **(C)** CAI stress vs. displacement.

Figure 7.22 presents the obtained maximum strain distribution, considering 17 J impact, for Case 3 and Case 4.

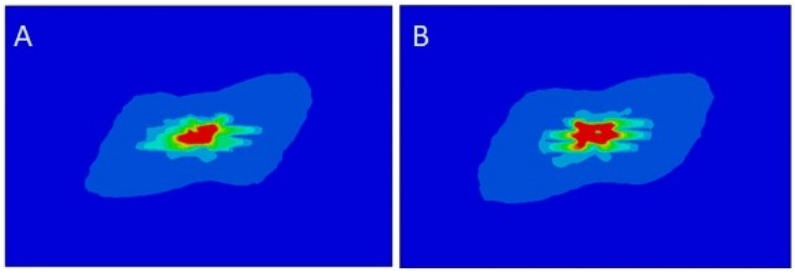

Figure 7.22: Maximum strain distribution considering 17 J impact: **(A) Case 3:** 3D model including cohesive surfaces using Abaqus available VUMAT with Hashin-Puck-based Nie (2014) failure criterion, **(B) Case 4:** 3D model including cohesive surfaces using modified VUMAT with Hashin extended failure criterion.

Figure 7.23 presents damage area measurement results for a 17 J impact case. One can observe similar damage areas for both numerical cases, both cases with values lower than the experimental results.

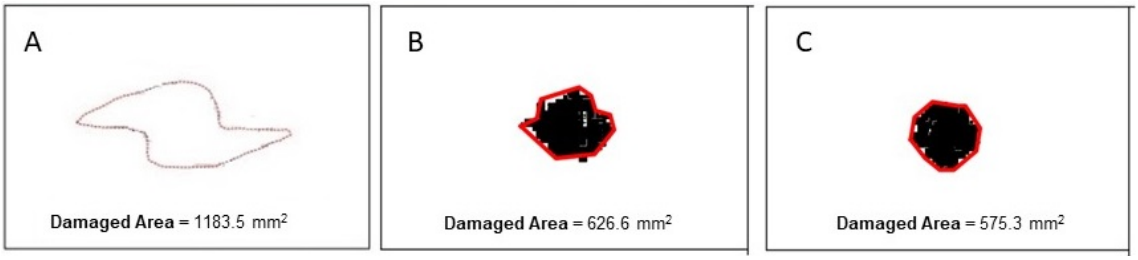

Figure 7.23: Damaged area considering 17 J impact: **(A) Experimental** (Tan et al., 2015*a*), **(B) Case 3:** 3D model including cohesive surfaces using Abaqus available VUMAT with Hashin-Puck-based Nie (2014) failure criterion, **(C) Case 4:** 3D model including cohesive surfaces using modified VUMAT with Hashin extended failure criterion.

Figure 7.24 (A and B) presents the obtained similar results for both models. Notice that the experimental impact force data is not given for these cases. For the stress versus displacement in the CAI case, as shown in Figure 7.24 (C), a better correlation is observed for case 3, although in both cases the maximum stress results were again lower than the experimental results.

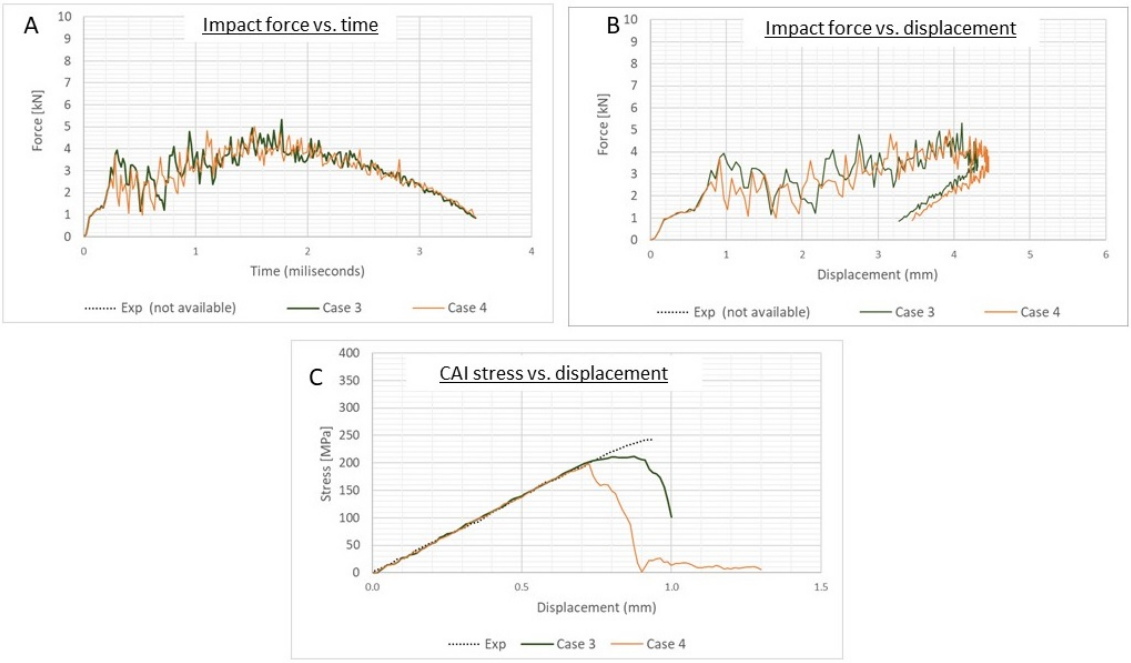

Figure 7.24: Virtual test measurements for Cases 3 and 4 considering 17 J impact: **(A)** Impact force vs. time, **(B)** Impact force vs. displacement, **(C)** CAI stress vs. displacement.

Figure 7.25 presents the obtained maximum strain distribution, considering 25 J impact, for Case 3 and Case 4.

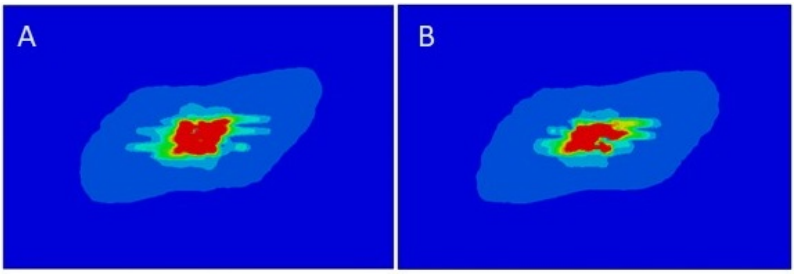

Figure 7.25: Maximum strain distribution considering 25 J impact: **(A) Case 3:** 3D model including cohesive surfaces using Abaqus available VUMAT with Hashin-Puck-based Nie (2014) failure criterion, **(B) Case 4:** 3D model including cohesive surfaces using modified VUMAT with Hashin extended failure criterion.

For a 25 J impact case (Figure 7.26), one can observe that both cases continue to present smaller damage areas than the experimental one, with a relatively closer result for Case 3.

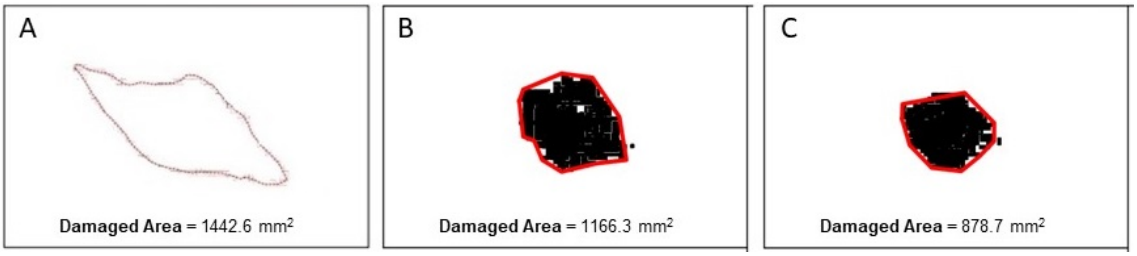

Figure 7.26: Damaged area considering 25 J impact: **(A) Experimental** (Tan et al., 2015*a*), **(B) Case 3:** 3D model including cohesive surfaces using Abaqus available VUMAT with Hashin-Puck-based Nie (2014) failure criterion, **(C) Case 4:** 3D model including cohesive surfaces using modified VUMAT with Hashin extended failure criterion.

Considering the experimental impact force data (Figure 7.27 (A and B)), despite the similar behavior of the numerical results, it was observed that the maximum obtained is lower than the experimental one. Experimental data for stress versus displacement was not presented in this CAI case and, as shown in Figure 7.27 (C), similar numerical results were obtained for both cases.

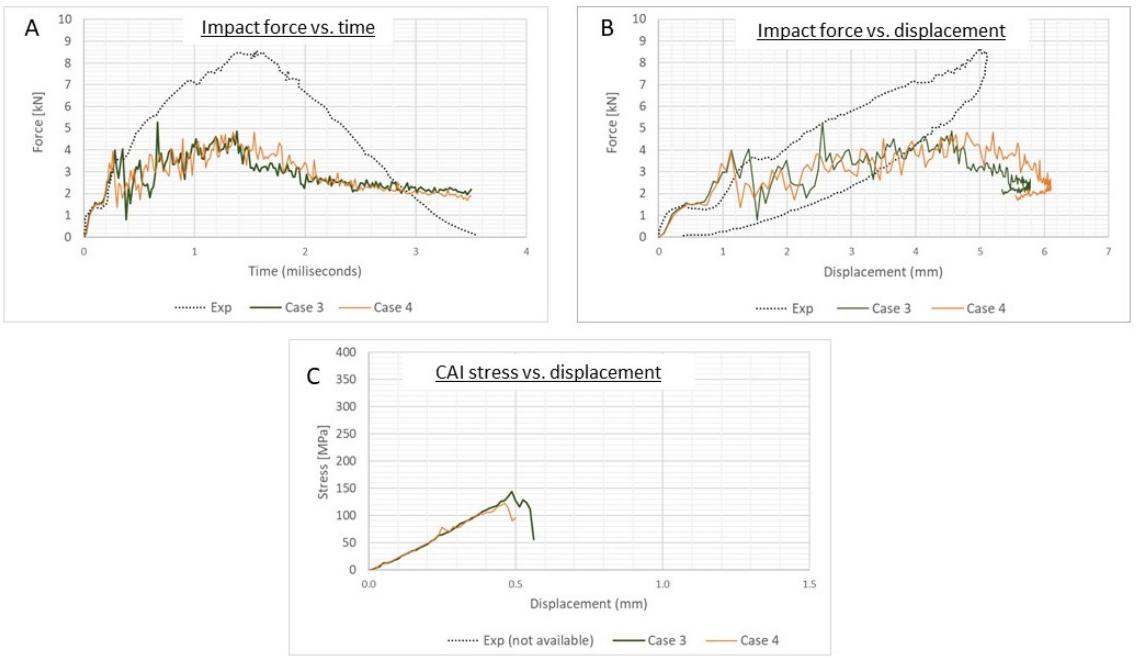

Figure 7.27: Virtual test measurements for Cases 3 and 4 considering 25 J impact: **(A)** Impact force vs. time, **(B)** Impact force vs. displacement, **(C)** CAI stress vs. displacement.

Figure 7.28 presents the obtained maximum strain distribution, considering 29.5 J impact, for Case 3 and Case 4.

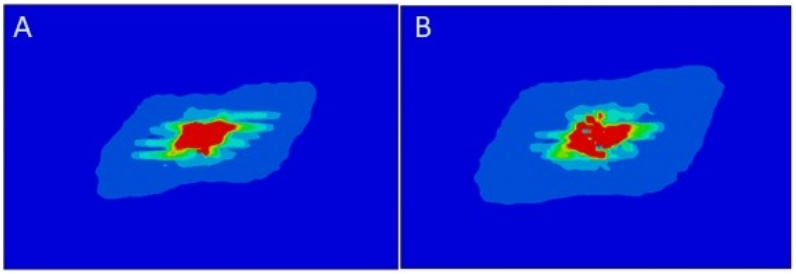

Figure 7.28: Maximum strain distribution considering 29.5 J impact: **(A) Case 3:** 3D model including cohesive surfaces using Abaqus available VUMAT with Hashin-Puck-based Nie (2014) failure criterion, **(B) Case 4:** 3D model including cohesive surfaces using modified VUMAT with Hashin extended failure criterion.

As shown in Figure 7.29,for a 29.5 J impact case, one can again observe similar damage obtained in both models, and again lower than the experimental result for both cases.

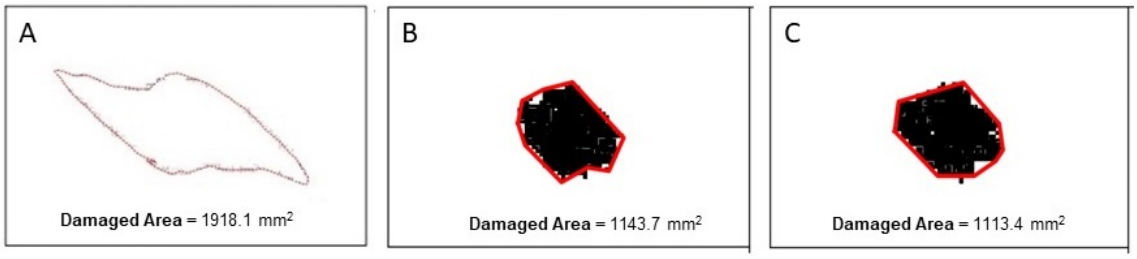

Figure 7.29: Damaged area considering 29.5 J impact: **(A) Experimental** (Tan et al., 2015*a*), **(B) Case 3:** 3D model including cohesive surfaces using Abaqus available VUMAT with Hashin-Puck-based Nie (2014) failure criterion, **(C) Case 4:** 3D model including cohesive surfaces using modified VUMAT with Hashin extended failure criterion.

The experimental impact force data over time, for this case, present only maximum load data, again with numerically inferior results to the experimental value (Figure 7.30 (A)). Probably due the lack of progressive damage model, both cases

presents poor correlation for impact force versus displacement in impact case (Figure 7.30 (B)) For CAI stress versus displacement, a better correlation is again observed for case 3 (Figure 7.30 (C)).

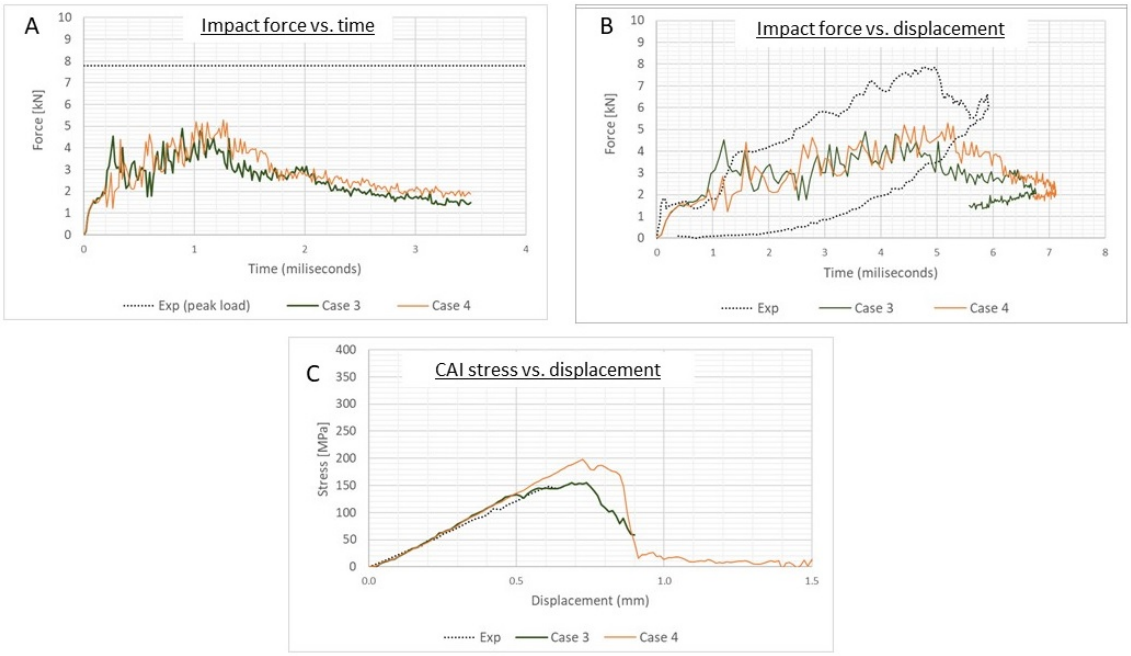

Figure 7.30: Virtual test measurements for Cases 3 and 4 considering 29.5 J impact: **(A)** Impact force vs. time, **(B)** Impact force vs. displacement, **(C)** CAI stress vs. displacement.

Considering the model case 5, which uses "3D" elements and the proposed multiscale model via VUMAT, allong with cohesive interfaces between the laminae, the following numerical-experimental correlations can be observed. The **Case 5** (Table 7.13) model considers the VUMAT proposed in this work, presented in section 5.2, which contains the multiscale criterion based on the Octagonal Fiber Model subsection 3.3.1. In summary, the macro-scale model feeds the VUMAT with material data and macro-scale stresses. Using the stress amplification factors (SAFs) calculated for the OFM (Huang et al., 2020), macro-stresses are converted into micro-stresses for fiber, matrix and interface in each of the OFM's quadrants. These approximated micro-scale stresses are then analyzed separately: For fibers, the verification is performed by a criterion of maximum longitudinal tension. This criterion

is a simplification of the Tsai-Wu criterion (subsection 3.3.2) when considering that the fiber has a high module compared to the matrix. Next, a damage homogenization criterion is proposed based on each of the 9 fiber's sub-regions. Similarly, the Bauwens criterion (subsection 3.3.3) is considered to verify each of the 20 regions of the matrix. Again, a damage homogenization criterion is proposed based on the proportion of the matrix damaged area. Finally, the stresses at the interface are verified considering the cohesive failure criterion (subsection 3.3.4), and a damage homogeneization was proposed considering the eight equal sides of the octagon. The calculated homogenized damage is then used to feed back the macroscale model as a degradation of the material's stiffness matrix.

Table 7.13: Case 5 summarized failure model.

Failure mode		Variable	Degradation process	Degraded terms
OFM-based multiscale criteria	Microscale fiber tension	A^f_{damT}	abrupt	C_d
	Microscale fiber compression	A^f_{damC}	abrupt	C_d
	Microscale matrix	$C_{Bauwens}$	linear strain-softening	C_d (except C_{11})
	Microscale interface	$C_{Interface}$	linear strain-softening	C_d (except C_{11})
Cohesive	Maximum stress criterion	-	energy based strain-softening	δ^o_n δ^o_s δ^o_t

Figure 7.31 presents the obtained maximum strain distribution, considering 6.5 J impact, for Case 5.

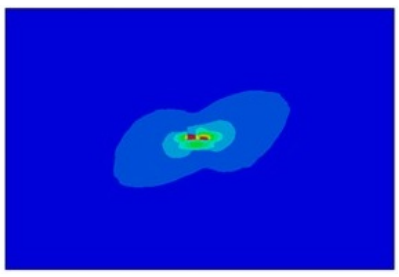

Figure 7.31: Maximum strain distribution considering 6.5 J impact for **Case 5:** 3D model including cohesive surfaces using mulitiscale approach with micromechanics OFM-based failure criterion.

Applying the proposed semi-automatic damage measurement procedure (section 5.3) for a 6.5 J impact case, one can observe in Figure 7.32 similar damage areas for the numerical and experimental cases. Despite this, a more concentrated damage is observed in the numerical results.

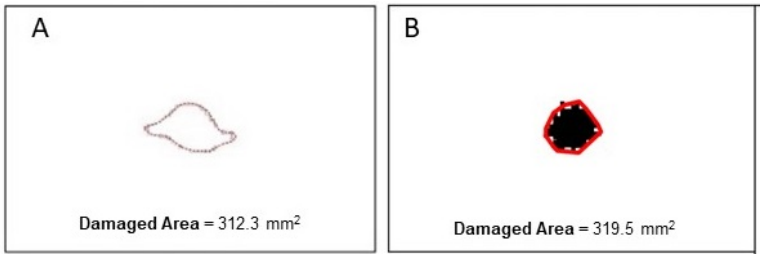

Figure 7.32: Damaged area considering 6.5 J impact: **(A) Experimental** (Tan et al., 2015*a*), **(B) Case 5:** 3D model including cohesive surfaces using mulitiscale approach with micromechanics OFM-based failure criterion.

The experimental force along the impact (Figure 7.33 (A)), for this case, present only data of maximum load, which was not reached by the numerical simulations. Probably due the simplified progressive damage model, the model presents a poor correlation for impact force versus displacement (Figure 7.33 (B)). For stress versus displacement in the CAI case (Figure 7.33 (C)), a good correlation of results is observed.

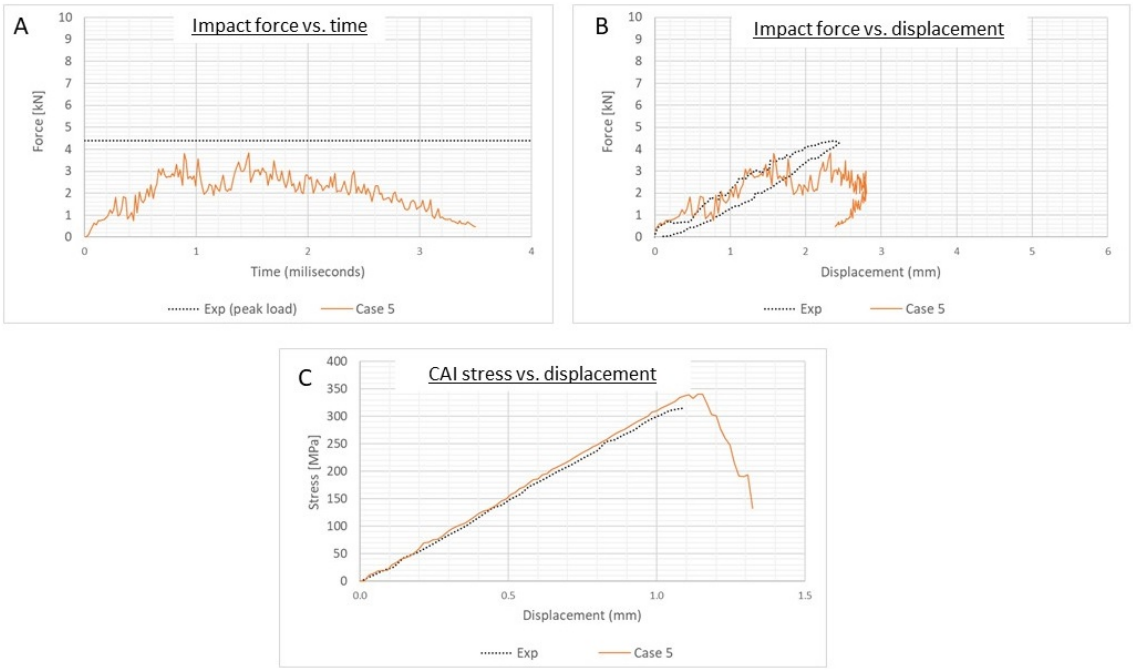

Figure 7.33: Virtual test measurements for Case 5 considering 6.5 J impact: **(A)** Impact force vs. time, **(B)** Impact force vs. displacement, **(C)** CAI stress vs. displacement.

Figure 7.34 presents the obtained maximum strain distribution, considering 17 J impact, for Case 5.

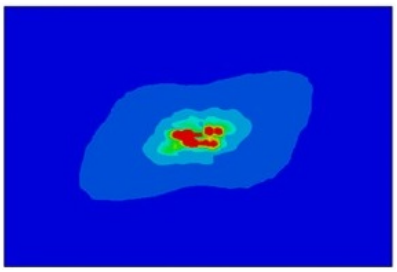

Figure 7.34: Maximum strain distribution considering 17 J impact for **Case 5:** 3D model including cohesive surfaces using mulitiscale approach with micromechanics OFM-based failure criterion.

For a 17J impact case, as presented in Figure 7.35, one can observe similar damage area for numerical case, if compared to experimental results, but again the damage occurs in a more concentrated way.

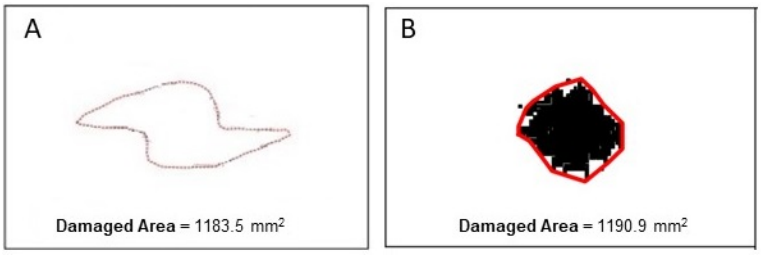

Figure 7.35: Damaged area considering 17 J impact: **(A) Experimental** (Tan et al., 2015*a*), **(B) Case 5:** 3D model including cohesive surfaces using mulitiscale approach with micromechanics OFM-based failure criterion.

Experimental force along impact data are not presented for this case, only numerical data is shown in Figure 7.36 (A and B). Figure 7.36 (C) presents stress versus displacement in the CAI case, where a good theoretical-experimental correlation is again observed.

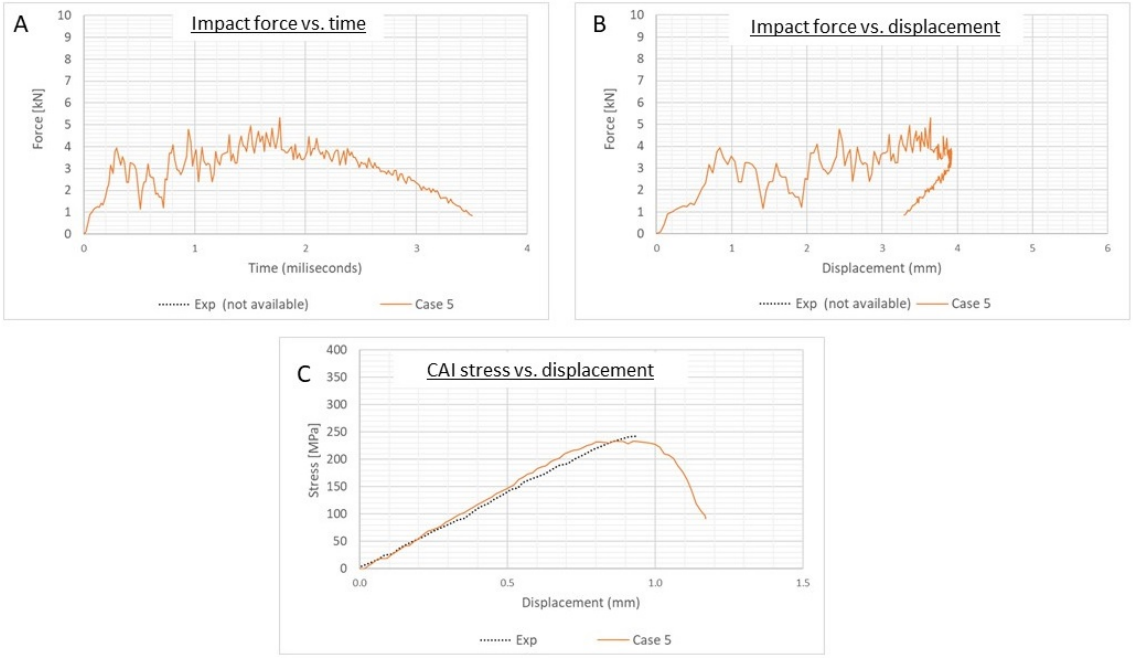

Figure 7.36: Virtual test measurements for Case 5 considering 17 J impact: **(A)** Impact force vs. time, **(B)** Impact force vs. displacement, **(C)** CAI stress vs. displacement.

Figure 7.37 presents the obtained maximum strain distribution, considering 25 J impact, for Case 5.

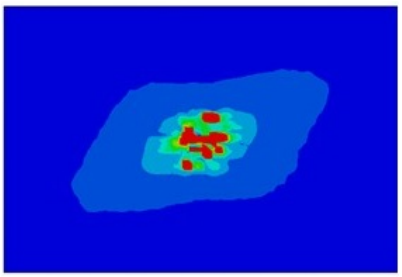

Figure 7.37: Maximum strain distribution considering 25 J impact for **Case 5:** 3D model including cohesive surfaces using mulitiscale approach with micromechanics OFM-based failure criterion.

For a case of 25 J impact (Figure 7.38), one can observe a numerical result with a damage area superior to the experimental one, however still showing the same tendency of concentrated damage.

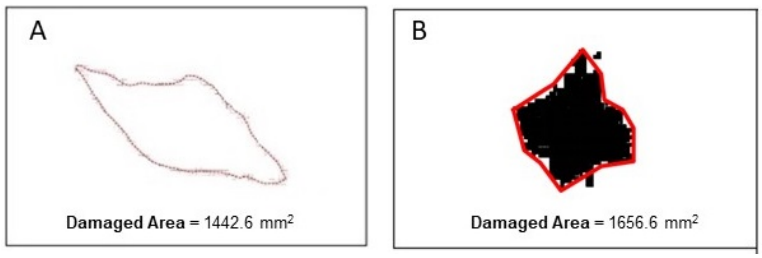

Figure 7.38: Damaged area considering 25 J impact: **(A) Experimental** (Tan et al., 2015*a*), **(B) Case 5:** 3D model including cohesive surfaces using mulitiscale approach with micromechanics OFM-based failure criterion.

The experimental force along impact data can be observed in Figure 7.39 (A and B), where the the maximum obtained numerical force is inferior to the experimental one. No experimental data for stress versus displacement were presented in this CAI case, Figure 7.39 (C) presents the numerical data.

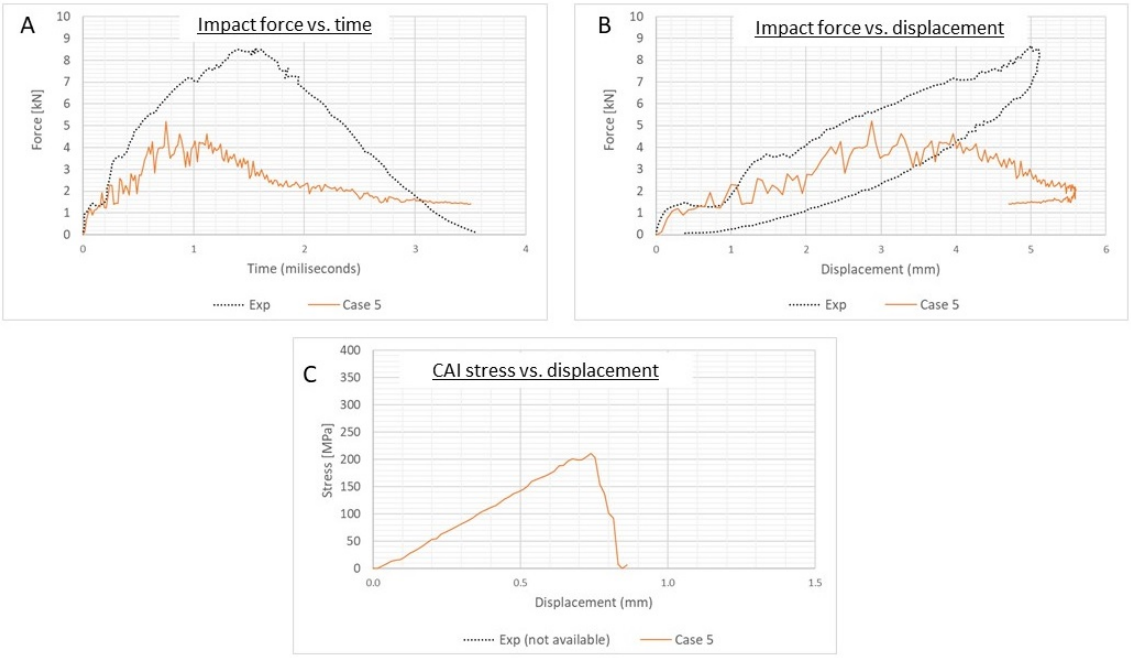

Figure 7.39: Virtual test measurements for Case 5 considering 25 J impact: **(A)** Impact force vs. time, **(B)** Impact force vs. displacement, **(C)** CAI stress vs. displacement.

Figure 7.40 presents the obtained maximum strain distribution, considering 29.5 J impact, for Case 5.

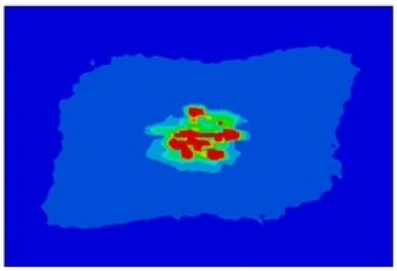

Figure 7.40: Maximum strain distribution considering 29.5 J impact for **Case 5:** 3D model including cohesive surfaces using mulitiscale approach with micromechanics OFM-based failure criterion.

Figure 7.41 presents impact force results for a 29.5 J energy. One can observe a numerical result with a damage area greater area than the experimental one, but still showing the same trend of concentrated damage.

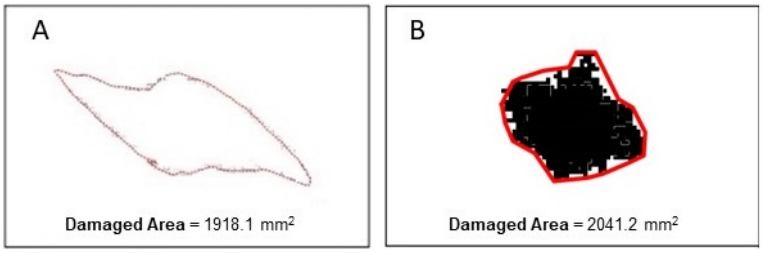

Figure 7.41: Damaged area considering 29.5 J impact: **(A) Experimental** (Tan et al., 2015*a*), **(B) Case 5:** 3D model including cohesive surfaces using mulitiscale approach with micromechanics OFM-based failure criterion.

The experimental impact force data, for this case, present only data of maximum load. In Figure 7.42 (A) is again possible to observe a numerical result inferior to the experimental value. Probably due the simplified progressive damage model, the model presents a poor correlation for impact force versus displacement, as shown in Figure 7.42 (B) For stress versus displacement in the CAI case, a higher residual resistance degradation is observed in the numerical case, compared to the experimental one, as shown in Figure 7.42 (C).

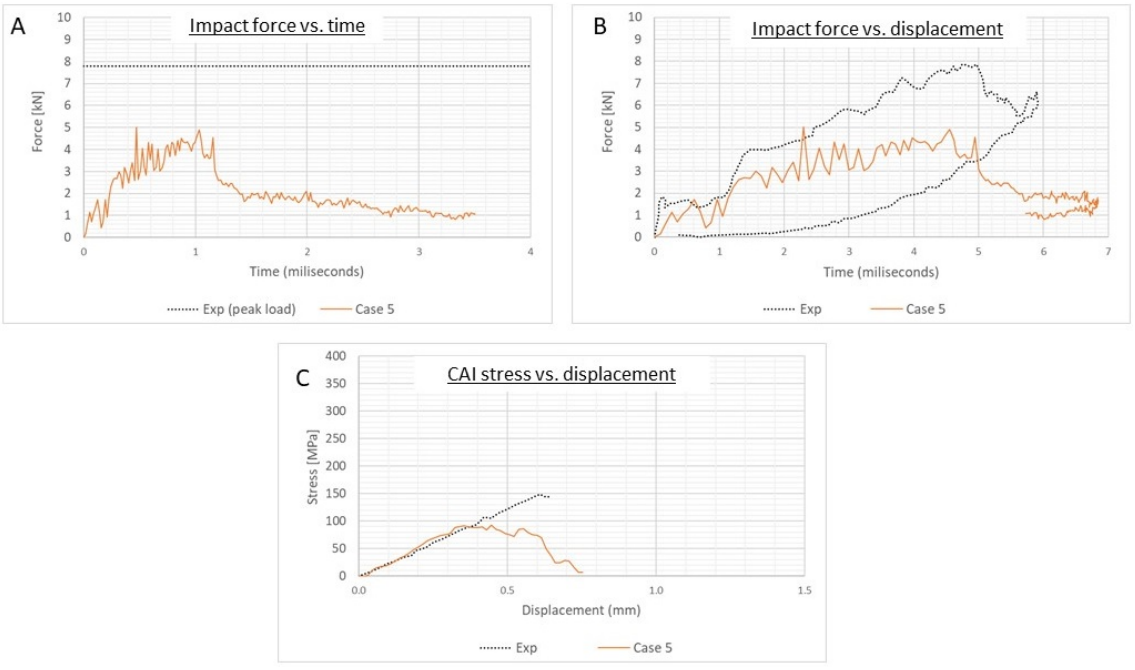

Figure 7.42: Virtual test measurements for Case 5 considering 29.5 J impact: **(A)** Impact force vs. time, **(B)** Impact force vs. displacement, **(C)** CAI stress vs. displacement.

Figure 7.43 presents a condensed experimental versus numerical impact damage area measurements comparison considering all cases with interlaminar cohesive surface model included between each model unidirectional layer (Cases 2, 3, 4, and 5). Considering damage areas obtained for the 4 analyzed energy levels, it is possible to observe that the proposed multiscale criterion, although simplified, presents gains in terms of impact damaged area results. However, these results are highly susceptible to modifications by changes in measurement criteria.

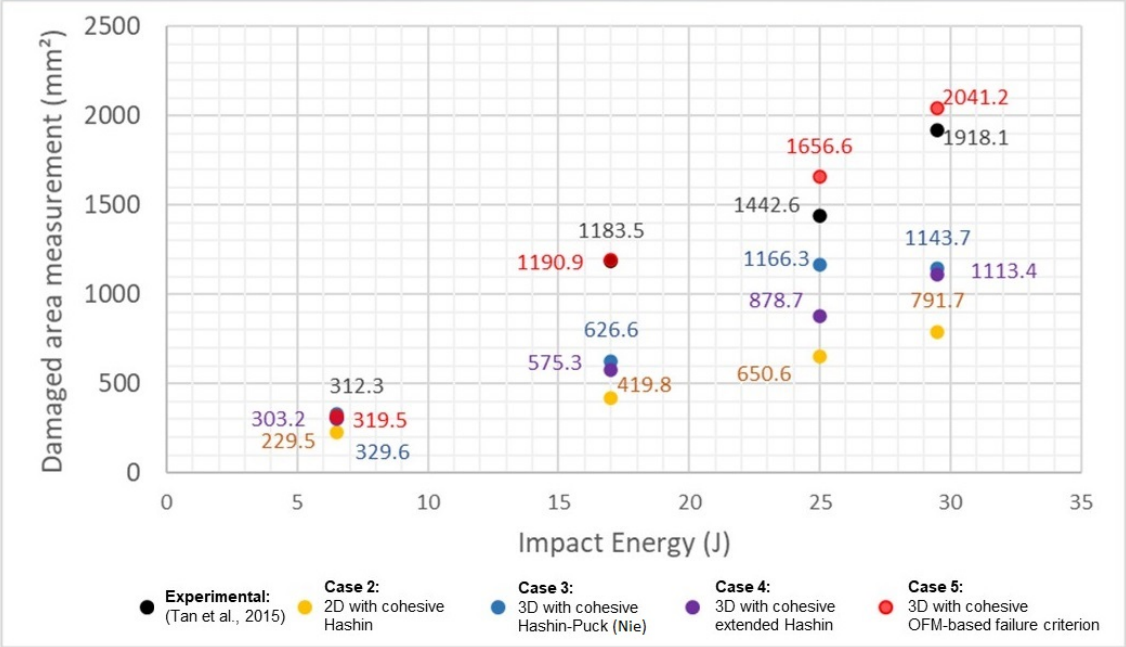

Figure 7.43: Simulation vs. experimental damaged area (Cases 2, 3, 4, and 5).

Observing in Figure 7.44 the residual resistance for each impact energy value, it is again possible to conclude that the proposed multi-scale model presented relatively good results, despite a tendency to be conservative in the case of higher energy. However, it is observed that conventional macro-scale models were also able to predict the phenomenon with different levels of precision, and that this type

of experimental result is highly susceptible to variations. It is also worth noting that the simplest case presented in this graph (case 2), where native Abaqus tools were used for Hasin and cohesive failure criteria, presented predictions close to the experimental one, although not conservative for high energy levels.

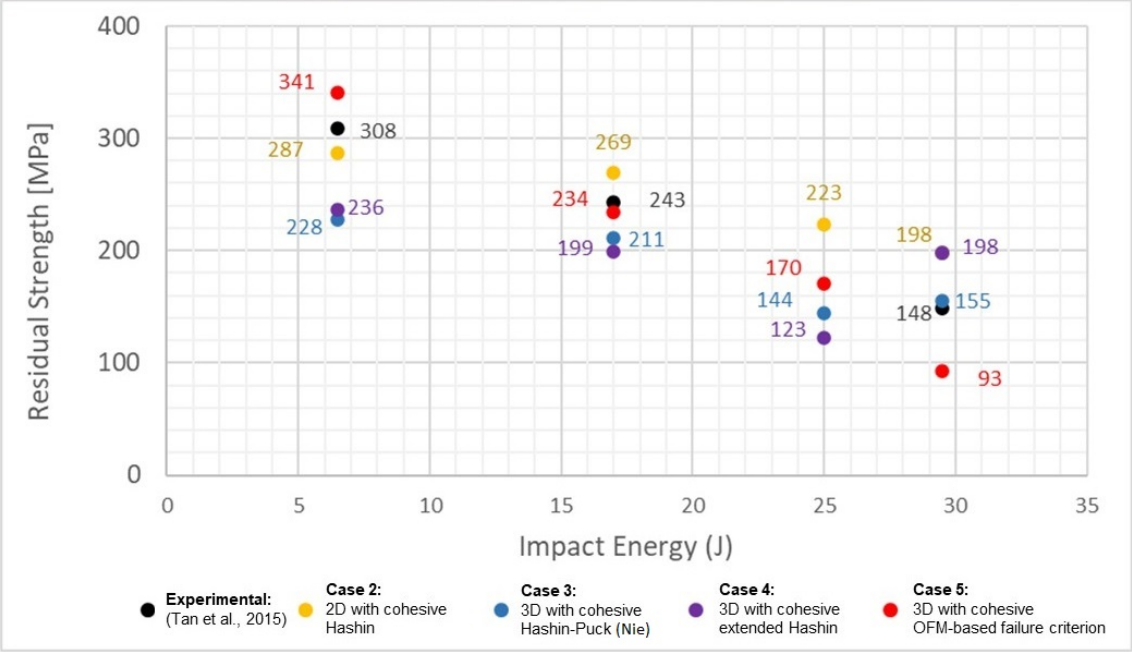

Figure 7.44: Simulation vs. experimental residual strength (Cases 2, 3, 4, and 5).

Chapter 8

Final Remarks

A multi-scale virtual testing methodology was developed with a focus on Compression After Impact (CAI) loading in composite materials focusing on reducing experimental impact and CAI test campaign.

An user-friendly and flexible Compression After Impact (CAI) Virtual Test Parametric Modeling Tool was coded within the program development framework of the commercial finite element platform Abaqus®. The developed architecture is capable to automatically process different layups, materials and failure criteria, to study damage tolerance and residual compression strength after impact in composite aeronautical components.

First, an Abaqus® user subroutine was developed in order to evaluate the three dimensional extension of Hashin failure criterion for fiber and matrix, modifying the original Abaqus® available VUMAT. Then, a multiscale analysis-based core for the proposed model was implemented in an Abaqus® user subroutine, based on the Octagonal Fiber Model and micro-mechanical failure criteria for fiber, matrix and interface. A damage homogenization metric was proposed, tested and implemented for OFM for the multi-scale approach, with considerable improvements for Compression After Impact (CAI) predictions with a relatively small computational cost increase.

A semi-automatic damage measurement metric was conceived to reduce human induced variables for impact damaged area measurements. The proposed tool was

designed to measure the damaged area and, optionally, non-negligible cracks, with minimal human interference.

Among the studied models in the CAI problem, the multiscale approach (case 5) presented the best results but still has uncertainties and a lack of standardization regarding micromechanical material inputs. Besides that, it is important to observe that the conventional macro-scale criteria were capable of achieving good CAI residual strength predictions and, if considering its simplicity and standardization, it may be still recommended for most studies. Considering the obtained results, the lamina level material input data availability and standardization, the computational cost, and the readiness of application, it is considered that the traditional form (two-dimensional) Hashin criteria are still the most advantageous option for industrial applications. Also, the conclusions are limited considering that the adopted input material data were obtained from literature without parametric studies. Besides that, it is important to notice that the cohesive inter-ply modeling was observed to play an important role in impact and compression after impact results.

8.1 Contributions of this Work

This work proposes a reliable, efficient and user-friendly virtual testing methodology, based on multi-scale approach, with a focus on Compression After Impact (CAI) loading in composite materials, where the main contributions can be highlighted as:

- A damage homogenization method was proposed, implemented and tested for OFM micro-mechanical model.
- A user subroutine (VUMAT) based on the Octagonal Fiber Model was developed to implement the multi-scale analysis model in Abaqus®.
- An automatic damage area measurement post-processor tool was proposed, implemented and tested.
- A comparison of results obtained using criteria traditionally applied in the industry and with the proposed multi-scale methodology was performed, concluding that the traditional form (two-dimensional) Hashin criteria is still the most advantageous option for industrial applications.

8.2 Suggestions for Future Work

Based on this work, the following future work proposals are suggested:

1. Verification, considering for applied works in each topic, the already implemented and pre-tested Virtual Test Parametric Modeling Tools for single-lap joints and Open Hole laminates.

2. Development of Virtual Test Parametric Modeling Tools considering different composite testing problems, as well as the development of an application package, based on the proposed semi-automatic architecture developed in Python during this work.

3. Numerical and/or experimental parametric study of macro and micro-scale input definitions and variability.

4. To expand the developed user subroutine (Abaqus®/Fortran) considering different types of multiscale-based Stress Amplification Factors (SAF), damage evolution methods and failure criteria, comparing the influence of different approximations.

5. To expand the developed user subroutine (Abaqus®/Fortran) considering statistically distributed defects and/or random fiber effects.

6. A statistical validation/calibration is suggested for the conceived Python semi-automatic damage measurement tool, considering an experimental and numerical controlled data sample.

Bibliography

Abir, M., Tay, T., Ridha, M. and Lee, H. (2017*a*), 'Modelling damage growth in composites subjected to impact and compression after impact', *Composite Structures* **168**, 13–25.

Abir, M., Tay, T., Ridha, M. and Lee, H. (2017*b*), 'On the relationship between failure mechanism and compression after impact (CAI) strength in composites', *Composite Structures* **182**, 242–250.

Aboudi, J. (1990), 'The nonlinear behavior of unidirectional and laminated composites-a micromechanical approach', *Journal of Reinforced Plastics and Composites* **9**(1), 13–32.

Aboudi, J. (1991), 'Micro-failure prediction of the strength of composite materials under combined loading', *Journal of Reinforced Plastics and Composites* **10**(5), 495–503.

Abrate, S. (2001), 'Modeling of impacts on composite structures', *Composite Structures* **51**(2), 129–138.

AIT (2010), 'Airbus industries test method 1-0010: Determination of compression strength after impact'.

Alves, M. P. and Cimini Jr, C. A. (2022), Localized fiber waviness and its effects in unidirectional composites under biaxial loading, *in* R. da Silva and T. Panzera, eds, 'Proceedings of the 6th Brazilian Conference on Composite Materials (Part of', pp. 671–675.

Amacher, R., Cugnoni, J., Botsis, J., Sorensen, L., Smith, W. and Dransfeld, C. (2014), 'Thin ply composites: Experimental characterization and modeling of size-effects', *Composites Science and Technology* **101**, 121–132.

Aminanda, Y., Castanié, B., Barrau, J.-J. and Thevenet, P. (2009), 'Experimental and numerical study of compression after impact of sandwich structures with metallic skins', *Composites Science and Technology* **69**(1), 50–59.

Anuse, V. S., Shankar, K., Velmurugan, R. and Ha, S. K. (2022), 'Compression-after-impact analysis of carbon fiber reinforced composite laminate with different ply orientation sequences', *International Journal of Impact Engineering* **167**, 104277.

ASTM (2010), 'D3039, standard test method for tensile properties of polymer matrix composite materials'.

ASTM (2012), 'D7137/d7137m-12, test method for compressive residual strength properties of damaged polymer matrix composite plates'.

ASTM (2014), 'D7136: Standard test method for measuring the damage resistance of a fiber-renforced polymer matrix composite to a drop-weight impact'.

Aymerich, F., Dore, F. and Priolo, P. (2008), 'Prediction of impact-induced delamination in cross-ply composite laminates using cohesive interface elements', *Composites Science and Technology* **68**(12), 2383–2390.

Aymerich, F., Lecca, G. and Priolo, P. (2008), 'Modelling of delamination growth in composite laminates by the virtual internal bond method', *Composites Part A: Applied Science and Manufacturing* **39**(2), 145–153.

Barbero, E. J. (2007), *Finite Element Analysis of Composite Materials*, CRC Press.

Bauwens, J. (1970), 'Yield condition and propagation of luders' lines in tension-torsion experiments on poly(vinyl chloride)', *Journal of Polymer Science Part A* **8**(2), 893–901.

Benzeggagh, M. and Kenane, M. (1996), 'Measurement of mixed-mode delamination fracture toughness of unidirectional glass/epoxy composites with mixed-mode bending apparatus', *Composites Sci Technol* **56**, 859–865.

bin Du, X., Zhu, H., Ai, J., sen Li, D. and Jiang, L. (2021), 'Parameterized meso-scale modeling and experimental study on the tensile damage evolution and strength of 3d five-directional braided composites', *Materials Design* **205**, 109702.

Borg, R., Nilsson, L. and Simonsson, K. (2004), 'Simulation of low velocity impact on fiber laminates using a cohesive zone based delamination model', *Composites Science and Technology* **64**(2), 279–288.

Camanho, P. P. and Davila, C. G. (2002), Mixed-mode decohesion finite elements for the simulation of delamination in composite materials, Technical Report TM-2002-211737, NASA.

Caminero, M., García-Moreno, I. and Rodríguez, G. (2017), 'Damage resistance of carbon fibre reinforced epoxy laminates subjected to low velocity impact: Effects of laminate thickness and ply-stacking sequence', *Polymer Testing* **63**, 530–541.

Caminero, M., García-Moreno, I. and Rodríguez, G. (2018), 'Experimental study of the influence of thickness and ply-stacking sequence on the compression after impact strength of carbon fibre reinforced epoxy laminates', *Polymer Testing* **66**, 360–370.

Cantwell, W. and Morton, J. (1991), 'The impact resistance of composite materials — a review', *Composites* **22**(5), 347–362.

Caprio, F. D., Langella, A., Lopresto, V. and Caprino, G. (2016), 'Numerical, experimental and analytical correlation for predicting the structural behavior of composite structures under impact', *Procedia Engineering* **167**, 80–87.

Cecot, W. and Oleksy, M. (2015), 'High order FEM for multigrid homogenization', *Computers & Mathematics with Applications* **70**(7), 1391–1400.

Chamis, C. (1983), Simplified composite micromechanics equations for hygral, thermal and mechanical properties, *in* 'NASA Technical Memorandum 83320'.

Chamis, C. C. (1987), 'Simplified composite micromechanics for predicting microstresses', *Journal of Reinforced Plastics and Composites* **6**(3), 268–289.

Chechkin, G. A., Piatnitski, A. L. and Shamaev, A. S. (2007), *Homogenization (Translations of Mathematical Monographs)*, American Mathematical Society.

Choi, H. Y. and Chang, F.-K. (1992), 'A model for predicting damage in graphite/epoxy laminated composites resulting from low-velocity point impact', *Journal of Composite Materials* **26**(14), 2134–2169.

Christoforou, A. P. (2001), 'Impact dynamics and damage in composite structures', *Composite Structures* **52**(2), 181–188.

Christoforou, A. P. and Yigit, A. S. (2009), 'Scaling of low-velocity impact response in composite structures', *Composite Structures* **91**(3), 358–365.

Cuntze, R. and Freund, A. (2004), 'The predictive capability of failure mode concept-based strength criteria for multidirectional laminates', *Composites Science and Technology* **64**(3-4), 343–377.

Daniel, I. and Ishai, O. (2005), *Engineering Mechanics of Composite Materials - 2nd ed.*, OXFORD UNIV PR.

Dassault Systemes (2014), 'Abaqus 6.14 - CAE user's manual'.

Davies, G. and Zhang, X. (1995), 'Impact damage prediction in carbon composite structures', *International Journal of Impact Engineering* **16**(1), 149–170.

Davila, C. G., Camanho, P. P. and Turon, A. (2007), Cohesive elements for shells, Technical Report TP-2007-214869, NASA.

Dixit, A., Mali, H. S. and Misra, R. (2013), 'Unit cell model of woven fabric textile composite for multiscale analysis', *Procedia Engineering* **68**, 352–358.

Eizaguirre, M. G. (2011), Tensile testing of 3d reinforced composites, Master's thesis, KTH, Lightweight Structures.

Elder, D. J., Thomson, R. S., Nguyen, M. Q. and Scott, M. L. (2004), 'Review of delamination predictive methods for low speed impact of composite laminates', *Composite Structures* **66**(1-4), 677–683.

Esaki, Y. S. K. M. M. K. M. S. Y. N. K. (2017), 'Progressive failure analysis for impact damage and compressive strength of composite laminates', *Mechanical Engineering Journal* **4**(5), 16–00710–16–00710.

Fatima, N. S., Dhaliwal, G. S. and Newaz, G. (2021), 'Influence of interfacial adhesive on impact and post-impact behaviors of CFRP/end-grain balsawood sandwich composites', *Composites Part B: Engineering* **212**, 108718.

Feng, D. and Aymerich, F. (2014), 'Finite element modelling of damage induced by low-velocity impact on composite laminates', *Composite Structures* **108**, 161–171.

Feng, Y., Zhang, H., Tan, X., He, Y., An, T. and Zheng, J. (2016), 'Effect of impact damage positions on the buckling and post-buckling behaviors of stiffened composite panel', *Composite Structures* **155**, 184–196.

Fotouhi, M., Damghani, M., Leong, M. C., Fotouhi, S., Jalalvand, M. and Wisnom, M. R. (2020), 'A comparative study on glass and carbon fibre reinforced laminated composites in scaled quasi-static indentation tests', *Composite Structures* **245**, 112327.

Gemi, D. S., Sahin, O. S. and Gemi, L. (2022), 'Experimental investigation of axial compression behavior after low velocity impact of glass fiber reinforced filament wound pipes with different diameter', *Composite Structures* **280**, 114929.

Gonzales, M. A. C., Dias, R. P. and Alves, M. (2009), An experimental-numerical analysis of the drop weight tear test, *in* '20th International Congress of Mechanical Engineering'.

González, E., Maimí, P., Camanho, P., Turon, A. and Mayugo, J. (2012), 'Simulation of drop-weight impact and compression after impact tests on composite laminates', *Composite Structures* **94**(11), 3364–3378.

Gopinath, G. and Batra, R. (2020), 'Prediction of elastic moduli and ultimate strength of fiber/yarn-reinforced elastic/plastic matrix using fourier series approach and cuboidal/wedge sub-volumes', *International Journal of Non-Linear Mechanics* **125**, 103539.

Ha, S. K., Huang, Y., Han, H. H. and Jin, K. K. (2010), 'Micromechanics of failure for ultimate strength predictions of composite laminates', *Journal of Composite Materials* **44**(20), 2347–2361.

Ha, S. K., Jin, K. K. and Huang, Y. (2008), 'Micro-mechanics of failure (MMF) for continuous fiber reinforced composites', *Journal of Composite Materials* **42**(18), 1873–1895.

Hamming, R. (1987), *Numerical Methods for Scientists and Engineers*, DOVER PUBN INC.

Han, G., Guan, Z., Li, X. and Du, S. (2016), 'Failure analysis of carbon fiber reinforced composite subjected to low velocity impact and compression after impact', *Journal of Reinforced Plastics and Composites* **35**(9), 727–746.

Hashin, Z. (1980), 'Failure criteria for unidirectional fiber composites', *Journal of Applied Mechanics* **47**(2), 329.

Hashin, Z. and Rotem, A. (1973), 'A fatigue criterion for fiber-reinforced materials', *Journal of Composite Materials* (7), 448–464.

Hayat, K. and Ha, S. K. (2014), 'Low-velocity impact-induced delamination detection by use of the s0 guided wave mode in cross-ply composite plates: A numerical study', *Journal of Mechanical Science and Technology* **28**(2), 445–455.

Hazzard, M. K., Hallett, S., Curtis, P. T., Iannucci, L. and Trask, R. S. (2017), 'Effect of fibre orientation on the low velocity impact response of thin dyneema® composite laminates', *International Journal of Impact Engineering* **100**, 35–45.

Herakovich, C. T. (1997), *Mechanics of Fibrous Composites*, Wiley.

Hexcel (2022), 'Hexply m21 product data sheet'. 2022-07-02.
URL: *https://www.hexcel.com/Resources/DataSheets/Prepreg*

Heydari-Meybodi, M., Saber-Samandari, S. and Sadighi, M. (2016), '3d multiscale modeling to predict the elastic modulus of polymer/nanoclay composites considering realistic interphase property', *Composite Interfaces* **23**(7), 641–661.

Hibbeler, R. (2000), *Resistência dos Materiais*, 3rd edn, Pearson Prentice Hall.

Hongkarnjanakul, N., Bouvet, C. and Rivallant, S. (2013), 'Validation of low velocity impact modelling on different stacking sequences of CFRP laminates and influence of fibre failure', *Composite Structures* **106**, 549–559.

Hou, J., Petrinic, N. and Ruiz, C. (2001), 'A delamination criterion for laminated composites under low-velocity impact', *Composites Science and Technology* **61**(14), 2069–2074.

Hou, J., Petrinic, N., Ruiz, C. and Hallett, S. (2000), 'Prediction of impact damage in composite plates', *Composites Science and Technology* **60**(2), 273–281.

Hou, Y., Meng, L., Li, G., Xia, L. and Xu, Y. (2021), 'A novel multiscale modeling strategy of the low-velocity impact behavior of plain woven composites', *Composite Structures* **274**, 114363.

Hou, Y., Wang, W., Meng, L., Sapanathan, T., Li, J. and Xu, Y. (2022), 'An insight into the mechanical behavior of adhesively bonded plain-woven-composite joints using multiscale modeling', *International Journal of Mechanical Sciences* **219**, 107063.

Huang, Y., Cimini, C. and Ha, S. (2020), 'A micromechanical unit cell model with an octagonal fiber for continuous fiber reinforced composites', *Journal of Composite Materials* **54**(28), 4495–4513.

Huang, Y., Jin, C. and Ha, S. K. (2012), 'Strength prediction of triaxially loaded composites using a progressive damage model based on micromechanics of failure', *Journal of Composite Materials* **47**(6-7), 777–792.

Huang, Y., Jin, K. K. and Ha, S. K. (2008), 'Effects of fiber arrangement on mechanical behavior of unidirectional composites', *Journal of Composite Materials* **42**(18), 1851–1871.

Huang, Y., Jin, K., Xu, L., Mustafa, G., Han, Y. and Ha, S. (2011), A micromechanical methodology for fatigue life prediction of polymeric matrix composites, *in* '18th Internationa Conference on Composite Materials'.

Huang, Y., Xu, L. and Ha, S. K. (2012), 'Prediction of three-dimensional composite laminate response using micromechanics of failure', *Journal of Composite Materials* **46**(19-20), 2431–2442.

Huebner, K. H. (1975), *The finite element method for engineers*, Wiley.

Ivančević, D. and Smojver, I. (2016), 'Explicit multiscale modelling of impact damage on laminated composites – part II: Multiscale analyses', *Composite Structures* **145**, 259–268.

Jayaram, R., Nagarajan, V. and Kumar, K. V. (2021), 'Low velocity impact and compression after impact behaviour of polyester pin-reinforced foam filled honeycomb sandwich panels', *Journal of Sandwich Structures Materials* **24**(1), 157–173.

Jesson, D. A. and Watts, J. F. (2012), 'The interface and interphase in polymer matrix composites: Effect on mechanical properties and methods for identification', *Polymer Reviews* **52**(3), 321–354.

Jin, K., Huang, Y., Lee, Y. and Ha, S. (2008), 'Distribution of micro stresses and interfacial tractions in unidirectional composites', *Journal of Composite Materials* **42**(18), 1825–1849.

Justo, J., Osuna, S. and París, F. (2015), 'Design of composite materials with improved impact properties', *Composites Part B: Engineering* **76**, 229–234.

Kadlec, M. and Kafka, V. (2015), 'Strain concentration during the compression of a carbon/epoxy composite after impact', *International Journal of Structural Integrity* **6**(2), 279–289.

Keegan, M., Nash, D. and Stack, M. (2013), 'Numerical modelling of hailstone impact on the leading edge of a wind turbine blade', *European Wind Energy Association) Annual Wind Energy Event* .

Kehrer, L., Wood, J. T. and BÃ¶hlke, T. (2020), 'Mean-field homogenization of thermoelastic material properties of a long fiber-reinforced thermoset and experimental investigation', *Journal of Composite Materials* **54**(25), 3777–3799.

Knopp, A., Funck, E., Holtz, A. and Scharr, G. (2022), 'Delamination and compression-after-impact properties of z-pinned composite laminates reinforced with circumferentially notched z-pins', *Composite Structures* **285**, 115188.

Kok, R., Martinez-Hergueta, F. and Teixeira-Dias, F. (2022), 'Tensile response of AP-PLY composites: A multiscale experimental and numerical study', *Composites Part A: Applied Science and Manufacturing* **159**, 106989.

Koloor, S., Karimzadeh, A., Yidris, N., Petru, M., Ayatollahi, M. and Tamin, M. (2020), 'An energy-based concept for yielding of multidirectional frp composite structures using a mesoscale lamina damage model', *Polymers* **12**, 157.

Koynagi, J., Shah, P. D., Kimura, S., Ha, S. K. and Kawada, H. (2009), 'Mixed-mode interfacial debonding simulation in single-fiber composite under a transverse load', *Journal of Solid Mechanics and Materials Engineering* **3**(5), 796–806.

Kwon, Y., Allen, D. H. and Talreja, R., eds (2007), *Multiscale Modeling and Simulation of Composite Materials and Structures*, Springer US.

LevyNeto, F. and Pardini, L. C. (2006), *Compositos Estruturais. Ciencia e Tecnologia*, Edgard Blucher.

Li, N. and Chen, P. (2016), 'Micro–macro FE modeling of damage evolution in laminated composite plates subjected to low velocity impact', *Composite Structures* **147**, 111–121.

Li, S. (1999), 'On the unit cell for micromechanical analysis of fibre-reinforced composites', *Proceedings of the Royal Society of London. Series A: Mathematical, Physical and Engineering Sciences* **455**(1983), 815–838.

Li, S. (2001), 'General unit cells for micromechanical analyses of unidirectional composites', *Composites Part A: Applied Science and Manufacturing* **32**(6), 815–826.

Lin, S. and Waas, A. M. (2021), 'Accelerating computational analyses of low velocity impact and compression after impact of laminated composite materials', *Composite Structures* **260**, 113456.

Linke, A. J. O.-F. M. (2022), Influence of initial matrix cracks on residualstrength in compression-after-impact simulation, *in* J. S. Gomes and S. Meguid, eds, 'Proceedings M2D2022 - 9th International Conference on Mechanics and Materials in Design', Funchal Portugal, pp. 37–48.

Liu, H., Falzon, B. G. and Tan, W. (2018), 'Predicting the compression-after-impact (CAI) strength of damage-tolerant hybrid unidirectional/woven carbon-fibre reinforced composite laminates', *Composites Part A: Applied Science and Manufacturing* **105**, 189–202.

Liu, H., Liu, J., Ding, Y., Zhou, J. and Kong, X. (2020), 'Effects of impactor geometry on the low-velocity impact behaviour of fibre-reinforced composites: An experimental and theoretical investigation', pp. 533–553.

Liu, P., Liao, B., Jia, L. and Peng, X. (2016), 'Finite element analysis of dynamic progressive failure of carbon fiber composite laminates under low velocity impact', *Composite Structures* **149**, 408–422.

Liu, Y., Jiang, Z. and Wen, H. (2020), 'Predicting impact induced delamination of FRP laminates', *International Journal of Impact Engineering* **137**, 103436.

Liv, Y., Guillamet, G., Costa, J., González, E., Marín, L. and Mayugo, J. (2017), 'Experimental study into compression after impact strength of laminates with conventional and nonconventional ply orientations', *Composites Part B: Engineering* **126**, 133–142.

Lopes, C., Sádaba, S., González, C., Llorca, J. and Camanho, P. (2016), 'Physically-sound simulation of low-velocity impact on fiber reinforced laminates', *International Journal of Impact Engineering* **92**, 3–17.

Lou, X., Cai, H., Yu, P., Jiao, F. and Han, X. (2017), 'Failure analysis of composite laminate under low-velocity impact based on micromechanics of failure', *Composite Structures* **163**, 238–247.

Ma, D., González-Jiménez, Á., Giglio, M., dos Santos Cougo, C. M., Amico, S. C. and Manes, A. (2021), 'Multiscale modelling approach for simulating low velocity impact tests of aramid-epoxy composite with nanofillers', *European Journal of Mechanics - A/Solids* **90**, 104286.

Marinucci, G. (2011), *Materiais Compositos Polimericos: Fundamentos e Tecnologia*, ARTLIBER.

Martinez, X., Rastellini, F., Oller, S., Flores, F. and Oñate, E. (2011), 'Computationally optimized formulation for the simulation of composite materials and delamination failures', *Composites Part B: Engineering* **42**(2), 134–144.

Meon, M., Nor, N., Shawal, S., Saedon, J., Rao, M. and Schroder, K.-U. (2020), 'On the modelling aspect of low- velocity impact composite laminates', *J. Mech. Eng* **2020**, 13–25.

Metoui, S., Pruliere, E., Ammar, A., Dau, F. and Iordanoff, I. (2018), 'A multiscale separated representation to compute the mechanical behavior of composites with periodic microstructure', *Mathematics and Computers in Simulation* **144**, 162–181.

Molina, A. C. and Curiel-Sosa, J. (2015), 'A multiscale finite element technique for nonlinear multi-phase materials', *Finite Elements in Analysis and Design* **94**, 64–80.

Montero, M. V., Barjasteh, E., Baid, H. K., Godines, C., Abdi, F. and Nikbin, K. (2017), 'Multi-scale impact and compression-after-impact modeling of reinforced benzoxazine/epoxy composites using micromechanics approach', *Journal of Multiscale Modelling* **08**(01), 1750002.

Mortell, D., Tanner, D. and McCarthy, C. (2016), 'An experimental investigation into multi-scale damage progression in laminated composites in bending', *Composite Structures* **149**, 33–40.

Moura, M., Magalhaes, A. G. and Morais, A. B. (2009), *Materiais Compositos Materiais, Fabrico e Comportamento Mecanico*, Publindustria.

Namdar, O. and Darendeliler, H. (2017), 'Buckling, postbuckling and progressive failure analyses of composite laminated plates under compressive loading', *Composites Part B: Engineering* **120**, 143–151.

Nie, Z. (2014), Advanced mesomechanical modeling of triaxially braided composites for dynamic impact analysis with failure, Master's thesis, University of Akron.

Niu, M. C. Y. (2010), *Composite Airframe Structures*, Hong Kong Conmilit Press Ltd.

Olsson, R. (2010), 'Analytical model for delamination growth during small mass impact on plates', *International Journal of Solids and Structures* **47**(21), 2884–2892.

Otero, F., Martínez, X., Oller, S. and Salomón, O. (2012), 'Study and prediction of the mechanical performance of a nanotube-reinforced composite', *Composite Structures* **94**(9), 2920–2930.

Otero, F., Oller, S., Martinez, X. and Salomón, O. (2015), 'Numerical homogenization for composite materials analysis. comparison with other micro mechanical formulations', *Composite Structures* **122**, 405–416.

Otsu, N. (1979), 'A threshold selection method from gray-level histograms.', *IEEE Trans. Syst. Man Cybern* **9**, 62–66.

Panettieri, E., Fanteria, D. and Danzi, F. (2016), 'Delaminations growth in compression after impact test simulations: Influence of cohesive elements parameters on numerical results', *Composite Structures* **137**, 140–147.

Park, J., Ha, S., Kang, K., Kim, C. and Kim, H. (2008), 'Impact damage resistance of sandwich structure subjected to low velocity impact', *Journal of Materials Processing Technology* **201**(1-3), 425–430.

Perillo, G., Jørgensen, J. K., Cristiano, R. and Riccio, A. (2017), 'A numerical/experimental study on the impact and CAI behaviour of glass reinforced compsite plates', *Applied Composite Materials* **25**(2), 425–447.

Piggott, M. R. (1987), 'The effect of the interface/interphase on fiber composite properties', *Polymer Composites* **8**(5), 291–297.

Puck, A. and Schurmann, H. (1998), 'Failure analysis of FRP laminates by means of physically based phenomenological models', *Composites Science and Technology* **58**, 1045–1067.

Raghava, R., Caddell, R. and Yeh, G. (1973), 'The macroscopic yield behavior of polymers', *Journal of Material Science* **8**, 225–232.

Rahmé, P., Bouvet, C., Rivallant, S., Fascio, V. and Valembois, G. (2012), 'Experimental investigation of impact on composite laminates with protective layers', *Composites Science and Technology* **72**(2), 182–189.

Rastellini, F., Oller, S., Salomón, O. and Oñate, E. (2008), 'Composite materials non-linear modelling for long fibre-reinforced laminates', *Computers & Structures* **86**(9), 879–896.

Ren, M., Cong, J., Wang, B. and Guo, X. (2017), 'Extended multiscale finite element method for small-deflection analysis of thin composite plates with aperiodic microstructure characteristics', *Composite Structures* **160**, 422–434.

Rezende, A. C., Costa, M. L. and Botelho, E. C. (2011), *Composito Estruturais: Tecnologia E Pratica*, ARTLIBER.

Rhead, A. T., Butler, R. and Hunt, G. W. (2017), 'Compressive strength of composite laminates with delamination-induced interaction of panel and sublaminate buckling modes', *Composite Structures* **171**, 326–334.

Richardson, M. and Wisheart, M. (1996), 'Review of low-velocity impact properties of composite materials', *Composites Part A: Applied Science and Manufacturing* **27**(12), 1123–1131.

Rivallant, S., Bouvet, C., Abdallah, E. A., Broll, B. and Barrau, J.-J. (2014), 'Experimental analysis of CFRP laminates subjected to compression after impact: The role of impact-induced cracks in failure', *Composite Structures* **111**, 147–157.

Rivallant, S., Bouvet, C. and Hongkarnjanakul, N. (2013), 'Failure analysis of CFRP laminates subjected to compression after impact: FE simulation using discrete interface elements', *Composites Part A: Applied Science and Manufacturing* **55**, 83–93.

Rozylo, P., Debski, H. and Kubiak, T. (2017), 'A model of low-velocity impact damage of composite plates subjected to compression-after-impact (CAI) testing', *Composite Structures* **181**, 158–170.

Santiago, R., Cantwell, W. and Alves, M. (2017), 'Impact on thermoplastic fibre-metal laminates: Experimental observations', *Composite Structures* **159**, 800–817.

Santos, G. B. M., Vial, E. D., Silva, L. S., Avila, P. H. O., Santos, T. L., de Andrade, M. F. and Panzera, T. H. (2022), Essential topics to compose a broad definition

of composite materials, *in* R. da Silva and T. Panzera, eds, 'Proceedings of the 6th Brazilian Conference on Composite Materials', pp. 671–675.

Schoeppner, G. and Abrate, S. (2000), 'Delamination threshold loads for low velocity impact on composite laminates', *Composites Part A: Applied Science and Manufacturing* **31**(9), 903–915.

Seamone, A., Davidson, P., Waas, A. M. and Ranatunga, V. (2022), 'Low velocity impact and compressive response after impact of thin carbon fiber composite panels', *International Journal of Solids and Structures* p. 111604.

Shah, S., Megat-Yusoff, P., Karuppanan, S., Choudhry, R., Din, I. U., Othman, A., Sharp, K. and Gerard, P. (2021), 'Compression and buckling after impact response of resin-infused thermoplastic and thermoset 3d woven composites', *Composites Part B: Engineering* **207**, 108592.

Shah, S., Megat-Yusoff, P., Karuppanan, S., Choudhry, R. and Sajid, Z. (2021), 'Multiscale damage modelling of 3d woven composites under static and impact loads', *Composites Part A: Applied Science and Manufacturing* **151**, 106659.

Sharpe, L. H. (1972), 'The interphase in adhesion', *The Journal of Adhesion* **4**(1), 51–64.

Shor, O. and Vaziri, R. (2017), 'Application of the local cohesive zone method to numerical simulation of composite structures under impact loading', *International Journal of Impact Engineering* **104**, 127–149.

Sihn, S.; Kim, R. K. K. T. S. (2007), 'Experimental studies of thin-ply laminated composites', *Composites Science and Technology* **67**(6), 996–1008.

Soto, A., González, E., Maimí, P., de la Escalera, F. M., de Aja, J. S. and Alvarez, E. (2018), 'Low velocity impact and compression after impact simulation of thin ply laminates', *Composites Part A: Applied Science and Manufacturing* **109**, 413–427.

Srinivasan, K. (2009), *Composite Materials: Production, Properties, Testing and Applications*, Alpha Science Intl Ltd.

Suemasu, H. (2016), 'Analytical approaches to compression after impact (CAI) behavior of carbon fiber-reinforced composite materials', *Advanced Composite Materials* **25**(1), 1–18.

Sun, C. and Vaidya, R. (1996), 'Prediction of composite properties from a representative volume element', *Composites Science and Technology* **56**(2), 171–179.

Sun, X. and Hallett, S. (2018), 'Failure mechanisms and damage evolution of laminated composites under compression after impact (CAI): Experimental and numerical study', *Composites Part A: Applied Science and Manufacturing* **104**, 41–59.

Swain, R., Reifsnider, K., Jayaraman, K. and El-Zein, M. (1990), 'Interface/interphase concepts in composite material systems', *Journal of Thermoplastic Composite Materials* **3**(1), 13–23.

Tan, R., Xu, J., Sun, W., Liu, Z., Guan, Z. and Guo, X. (2019), 'Relationship between matrix cracking and delamination in cfrp cross-ply lami-nates subjected to low velocity impact', *Materials (Basel)* (23), 12.

Tan, W., Falzon, B. G., Chiu, L. N. and Price, M. (2015*a*), 'Predicting low velocity impact damage and compression-after-impact (CAI) behaviour of composite laminates', *Composites Part A: Applied Science and Manufacturing* **71**, 212–226.

Tan, W., Falzon, B. G., Chiu, L. N. S. and Price, M. (2015*b*), 'Numerical prediction of the low-velocity impact damage and compression after impact strength of composite laminates', *IOP Conference Series: Materials Science and Engineering* **74**, 012015.

Tang, Y., Zhou, Z., Pan, S., Xiong, J. and Guo, Y. (2015), 'Mechanical property and failure mechanism of 3d carbon–carbon braided composites bolted joints under unidirectional tensile loading', *Materials and Design (1980-2015)* **65**, 243–253.

Tiberkak, R., Bachene, M., Rechak, S. and Necib, B. (2008), 'Damage prediction in composite plates subjected to low velocity impact', *Composite Structures* **83**(1), 73–82.

Toray (2022), 'Carbon fiber toray t700 technical data sheet available online'. 2022-07-02.
URL: *https://www.toraycma.com/page.php?id=661*

Tsai, S. and Wu, E. (1971), 'A general theory of strength for anisotropic materials', *Journal of Composite Materials* **5**, 58–80.

Tuo, H., Lu, Z., Ma, X., Zhang, C. and Chen, S. (2019), 'An experimental and numerical investigation on low-velocity impact damage and compression-after-impact behavior of composite laminates', *Composites Part B: Engineering* **167**, 329–341.

Ullah, H. and Silberschmidt, V. (2015), Analysis of impact induced damage in composites for wind turbine blades, *in* 'Proceedings of the 2015 Power Generation System and Renewable Energy Technologies (PGSRET)', Islamabad, Pakistan.

van Hoorn, N., Kassapoglou, C., Turteltaub, S. and van den Brink, W. (2022), 'Experimental damage tolerance evaluation of thick fabric carbon/epoxy laminates under low-velocity and high-velocity impact and compression-after-impact', *Journal of Composite Materials* **56**(5), 761–778.

Verma, A. S., Jiang, Z., Vedvik, N. P., Gao, Z. and Ren, Z. (2019), 'Impact assessment of a wind turbine blade root during an offshore mating process', *Engineering Structures* **180**, 205–222.

Verma, A. S., Vedvik, N. P. and Gao, Z. (2019), 'A comprehensive numerical investigation of the impact behaviour of an offshore wind turbine blade due to impact loads during installation', *Ocean Engineering* **172**, 127–145.

Verma, A. S., Vedvik, N. P., Haselbach, P. U., Gao, Z. and Jiang, Z. (2019), 'Comparison of numerical modelling techniques for impact investigation on a wind turbine blade', *Composite Structures* **209**, 856–878.

Verma, A., Vedvik, N. and Gao, Z. (2017), Numerical assessment of wind turbine blade damage due to contact/impact with tower during installation, *in* 'Proceedings of the IOP Conference Series: Materials Science and Engineering', Vol. 276, Busan, Korea, pp. 25–27.

Vignoli, L. L., Savi, M. A., Pacheco, P. M. C. L. and Kalamkarov, A. L. (2022), 'A novel micromechanical model based on the rule of mixtures to estimate effective elastic properties of circular fiber composites', *Applied Composite Materials* .

Walt, S., Schonberger, J., Nunez-Iglesias, J., Boulogne, F., Warner, J., Yager, N., Gouillart, E., Yu, T. and scikit-image contributors (2014), 'scikit-image: Image processing in python', *PeerJ* **2**, e453.

WANG, C. and NAGASHIMA, T. (2022), 'Compression-after-impact test analysis of CFRP skin-stringer specimen by FEM using a zig-zag type cohesive zone model', *Mechanical Engineering Journal* **9**(3), 22–00063–22–00063.

Wang, X., Cao, W., Deng, C., Wang, P. and Yue, Z. (2015), 'Experimental and numerical analysis for the post-buckling behavior of stiffened composite panels with impact damage', *Composite Structures* **133**, 840–846.

Wang, Y., Wang, J., Wang, J. and Hui, D. (2021), 'Experimental and multiscale numerical investigations on low-velocity impact responses of syntactic foam composites reinforced with modified MWCNTs', *Nanotechnology Reviews* **10**(1), 883–903.

Xia, Z., Zhang, Y. and Ellyin, F. (2003), 'A unified periodical boundary conditions for representative volume elements of composites and applications', *International Journal of Solids and Structures* **40**(8), 1907–1921.

Xing, Y., Gao, Y. and Li, M. (2017), 'The multiscale eigenelement method in dynamic analyses of periodical composite structures', *Composite Structures* **172**, 330–338.

Xu, K., Chen, W., Liu, L., Zhao, Z. and Luo, G. (2021), 'A hierarchical multiscale strategy for analyzing the impact response of 3d braided composites', *International Journal of Mechanical Sciences* **193**, 106167.

Xu, L., Jin, C. Z. and Ha, S. K. (2014), 'Ultimate strength prediction of braided textile composites using a multi-scale approach', *Journal of Composite Materials* **49**(4), 477–494.

Yang, B., Chen, Y., Lee, J., Fu, K. and Li, Y. (2021), 'In-plane compression response of woven CFRP composite after low-velocity impact: Modelling and experiment', *Thin-Walled Structures* **158**, 107186.

Yang, B., Lu, L., Liu, X., Xie, Y., Li, J. and Tang, Y. (2017), 'Uniaxial tensile and impact investigation of carbon-fabric/polycarbonate composites with different weave tow widths', *Materials Design* **131**, 470–480.

Yang, L., Wu, Z., Gao, D. and Liu, X. (2016), 'Microscopic damage mechanisms of fibre reinforced composite laminates subjected to low velocity impact', *Computational Materials Science* **111**, 148–156.

Yasaee, M., Mohamed, G., Pellegrino, A., Petrinic, N. and Hallett, S. R. (2017), 'Strain rate dependence of mode II delamination resistance in through thickness reinforced laminated composites', *International Journal of Impact Engineering* **107**, 1–11.

Yerbolat, G., Amangeldi, S., Ali, M., Badanova, N., Ashirbeok, A. and Islam, G. (2018), Composite materials property determination by rule of mixture and monte carlo simulation, *in* 'IEEE International Conference on Advanced Manufacturing (ICAM)'.

Yin, H. and Iannucci, L. (2022), 'An experimental and finite element investigation of compression-after-impact (CAI) behaviour of biaxial carbon fibre non-crimp-fabric (NCF) based composites', *Composite Structures* **281**, 115057.

Yu, Z. and Gao, S. (2016), 'Increase of contact radius due to deflection in low velocity impact of composite laminates and prediction of delamination threshold load', *Composite Structures* **147**, 286–293.

Zhang, C., Duodu, E. A. and Gu, J. (2017), 'Finite element modeling of damage development in cross-ply composite laminates subjected to low velocity impact', *Composite Structures* **173**, 219–227.

Zhang, C., Zhu, Q., Curiel-Sosa, J. L. and Bui, T. Q. (2020), 'Ballistic performance and damage simulation of fiber metal laminates under high-velocity oblique impact', *International Journal of Damage Mechanics* **29**(7), 1011–1034.

Zhang, H. T. Z. L. X. M. J. X. C. (2019), 'Damage and failure mechanism of thin composite laminates under low-velocity impact and compression-after-impact loading conditions', *Composites Part B: Engineering* **163**, 642–654.

Zhang, J., Li, C., Zhu, C. and Zhao, Z. (2021), 'Analysis of biaxial mechanical properties and failure criterion of self-compacting concrete', *Frontiers in Materials* **8**.

Zhang, Y., Li, H., Gao, Y., Lou, R., Ge, L. and Fang, D. (2022), 'Multi-scale modeling and elastic properties prediction of 3d four-directional tubular braided composites', *Composite Structures* **292**, 115632.

Zhao, C., Huang, Y., Chen, Z. and Ha, S. K. (2017), 'Progressive failure prediction of a landing gear structure of braided composites', *Composite Structures* **161**, 407–418.

Zhou, G., Sun, Q., Li, D., Meng, Z., Peng, Y., Chen, Z., Zeng, D. and Su, X. (2021), 'Meso-scale modeling and damage analysis of carbon/epoxy woven fabric composite under in-plane tension and compression loadings', *International Journal of Mechanical Sciences* **190**, 105980.

Zou, J., Lei, Z., Bai, R., Liu, D., Jiang, H., Liu, J. and Yan, C. (2021), 'Damage and failure analysis of composite stiffened panels under low-velocity impact and compression after impact', *Composite Structures* **262**, 113333.